Astronomy Letters, Vol. 29, No. 7, 2003, pp. 425–428. Translated from Pis'ma v Astronomicheskiĭ Zhurnal, Vol. 29, No. 7, 2003, pp. 483–487.

A Possible Shock Wave in the Intergalactic Medium of the Cluster of Galaxies A754

R. A. Krivonos[1*], A. A. Vikhlinin[1], M. L. Markevitch[2], and M. N. Pavlinsky[1]

[1] *Space Research Institute, Russian Academy of Sciences, Profsoyuznaya ul. 84/32, Moscow, 117810 Russia*

[2] *Harvard–Smithsonian Center for Astrophysics, 60 Garden Street, Cambridge, MA 02138 USA*

Received January 17, 2003

Abstract—The cluster of galaxies A754 is undergoing a merger of several large structural units. X-ray observations show the nonequilibrium state of the central part of the cluster, in which a cloud of cold plasma ~500 kpc in size was identified amid the hotter cluster gas. The X-ray image of A754 exhibits a brightness discontinuity, which can be interpreted as a shock wave in front of a moving cloud of dense gas. The shock parameters are determined from the jump in intergalactic gas density using the ROSAT image. The estimated Mach number is $M_1 = 1.71^{+0.45}_{-0.24}$ at a 68% confidence level. © *2003 MAIK "Nauka/Interperiodica".*

Key words: *clusters of galaxies, shock waves.*

INTRODUCTION

Clusters of galaxies are the largest gravitationally bound objects in the Universe. Mergers of clusters result in the release of potential energy into the intergalactic medium at a level of 10^{63} erg, mainly in the form of heating by shock waves. Consequently, observations of shock waves in the intergalactic medium, which provide information for studying the physical processes that accompany the formation of clusters, are of practical interest.

Here, we study A754, a rich cluster of galaxies at $z = 0.0541$ in the stage of violent formation. ASCA data clearly indicate that the central part of the cluster is in a nonequilibrium state and hot and cold regions are identifiable in it (Henriksen and Markevitch 1996). The pattern probably represents the motion of a cold dense cloud through a hotter ambient gas. Structures of this kind were observed by the Chandra satellite in several clusters (Markevitch *et al.* 2000, 2001; Vikhlinin *et al.* 2001). The merging parts of the clusters are expected to move at a supersonic speed, which leads to the formation of shock waves.

The ROSAT X-ray image of the cluster of galaxies A754 exhibits a surface-brightness discontinuity, which can be interpreted as a shock wave in front of a moving cloud of dense gas. The amplitude of the surface-brightness discontinuity makes it possible to determine the jump in gas density at the shock front and, hence, the Mach number $M = v/v_s$, where v is the shock velocity and v_s is the speed of sound in the medium. Unfortunately, the ROSAT energy range (0.5–2.5 keV) does not allow us to determine the gas temperature at the shock boundary; i.e., we cannot independently verify the interpretation of the brightness discontinuity as a shock wave using the temperature jump.

Here, we estimate the distances by assuming that $H_0 = 50$ km s^{-1} Mpc^{-1}. The measured velocity and Mach number do not depend on H_0.

DATA ANALYSIS

Figure 1 shows the ROSAT image of the cluster of galaxies A754. The region of cold gas appears as a bright cloud at the image center. By its shape and position, the brightness discontinuity to the left from the center can be interpreted as a shock in front of a cloud of cold gas moving at a supersonic speed.

Quantitative information about the gas density distribution can be obtained by analyzing the brightness profile. The shape of the front of the putative shock is well described by a circle with a radius of ~1 Mpc. The circle center is taken as the reference point of distances. To determine the surface-brightness profile, we took a ±15° sector with respect to the front symmetry axis.[1] The cluster-brightness

[*] E-mail: krivonos@hea.iki.rssi.ru

[1] The sector opening angle was determined by the size of the brightness discontinuity region; the brightness profile for the outer part of the shock was obtained in a wider sector (±20°) to improve the statistics.

1063-7737/03/2907-0425$24.00

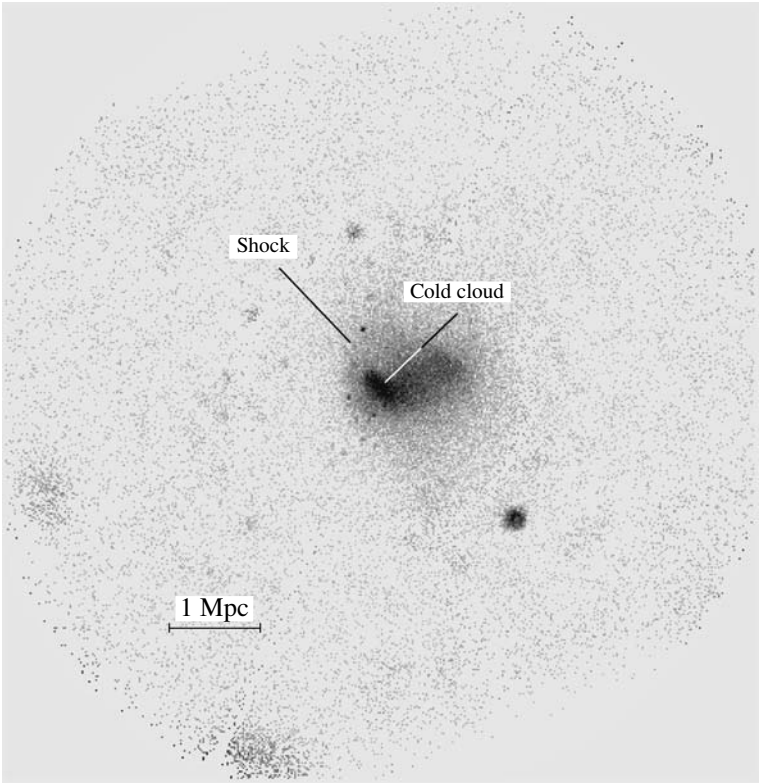

Fig. 1. The ROSAT X-ray image of the cluster of galaxies A754 in the energy range 0.7–2.0 keV. The brightness discontinuity to the left of the central body most likely corresponds to the shock.

profile was measured in concentric rings of equal logarithmic width; the ratio of the inner and outer ring radii was 1.01. We verified that varying the reference point changed the measured jump in gas density only slightly.

Measuring the gas-density distribution at large radii requires a careful processing of X-ray images; special attention should be given to the proper background subtraction and the correction for the loss of sensitivity at large deviations from the optical axis. The images that we used were obtained with the software package of S. Snowden (Snowden *et al.* 1994), which allows the periods of an anomalously high background of particles and scattered solar X-ray emission to be detected and eliminated. In addition, the exposure maps are computed and all of the known background components are fitted. The final result is an image in a given energy range that contains only the cluster radiation, pointlike X-ray sources, and the persistent cosmic X-ray background. An optimal ratio of the cluster surface brightness to the background level is achieved by using data above 0.7 keV.

When measuring the X-ray brightness profile, we eliminated all of the detectable pointlike sources and all the extended sources unrelated to the main radiation from the cluster. The cluster gives an appreciable contribution to the total brightness even at large distances from the center ($\sim$2 Mpc). Therefore, the region that could be used to directly determine the background level is difficult to identify. For this reason, we derived the background level by fitting the brightness profile at large distances by the β model (Cavaliere and Fusco-Femiano 1976) as follows:

$$I(r) = I_0 \left(1 + (r/r_c)^2\right)^{-3\beta+1/2} + I_b, \qquad (1)$$

where $I(r)$ is the surface brightness, I_b is the background intensity, and r_c is the cluster core radius.

FITTING THE BRIGHTNESS PROFILE

The main parameter of the shock motion is the Mach number, $M = v/v_s$. The Mach number can be expressed in a standard way (Landau and Lifshits 1988) in terms of the jump in any of the gas parameters (density, pressure, temperature) at the shock front. The most easily measurable quantity is the density jump, because the gas density is related to the emissivity by a simple relation: $\varepsilon \sim \rho^2$. Consequently, the problem reduces to deprojecting the brightness discontinuity.

The brightness profile can be best deprojected by fitting the data by some analytic dependence. Since the outer part of the cluster is most likely to have not

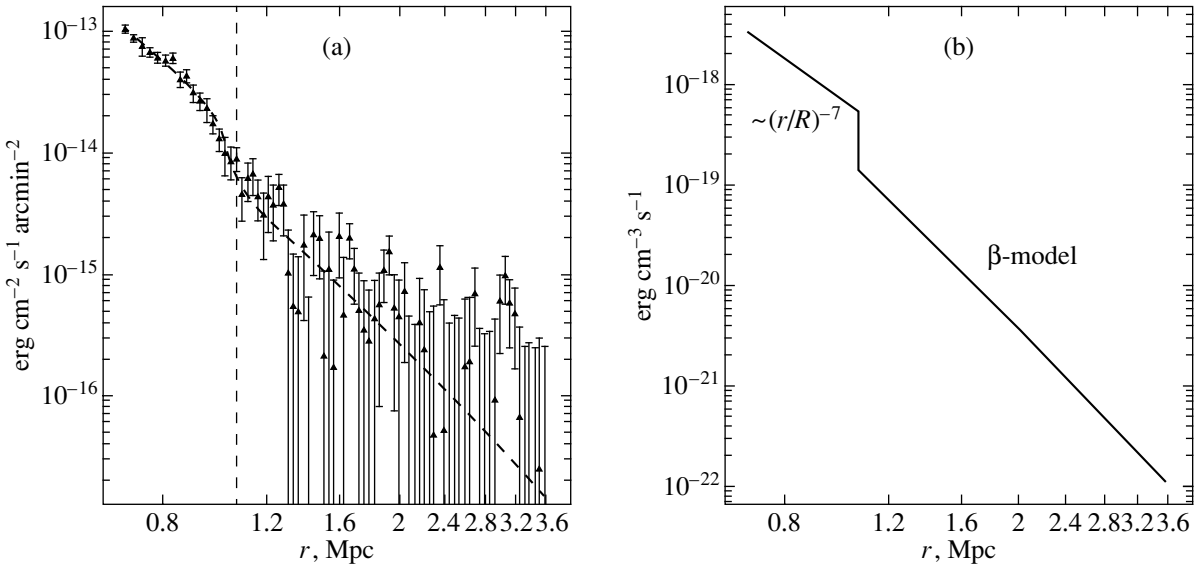

Fig. 2. (a) The surface-brightness profile in the shock region. The distances are measured from the center of curvature of the front along the direction of the shock propagation; the solid line represents the fitting curve obtained by integrating the plasma emissivity model (b) along the line of sight.

yet been perturbed by the shock, we can assume that the gas-density profile is described by the standard β model. Inside the shock front, we will be concerned with a narrow range of radii in which the density profile can be assumed, to sufficient accuracy, to be a power-law one. Thus, we have the following model of the plasma emissivity:

$$\varepsilon(r) = \begin{cases} \varepsilon_2 (r/R)^{\alpha} & \text{if } r \leqslant R \\ \varepsilon_\beta (1 + r^2/r_{\rm c}^2)^{-3\beta} & \text{if } r > R, \end{cases} \quad (2)$$

where R is the front position, ε_2 is the postshock emissivity, and ε_β is the central emissivity for the β model. The core radius $r_{\rm c}$ was fixed at a typical value of 250 kpc (Jones and Forman 1984).

The model emissivity profile was numerically integrated along the line of sight and folded with the angular resolution of the telescope ($\sim 25''$). Note that the normalization of the β model in formula (2) can be expressed in terms of the preshock emissivity ε_1. To determine the parameters of the above model, we minimized the χ^2 value for four parameters (ε_2, $\varepsilon_2/\varepsilon_1$, β, α). Figure 2 shows the derived model of the gas emissivity distribution (Fig. 2b) and the surface-brightness profile (Fig. 2a).

RESULTS

The emissivity jump obtained by fitting the brightness profile is trivially transformed into the density jump ($\varepsilon_2/\varepsilon_1$):

$$\frac{\rho_2}{\rho_1} = \left(\frac{\varepsilon_2}{\varepsilon_1}\right)^{1/2} = 1.98^{+0.44}_{-0.32}. \quad (3)$$

The quoted errors at a 68% confidence level correspond to $\Delta\chi^2 = 1$ when one parameter concerned is varied. From the ρ_2/ρ_1 ratio, we find the Mach number of the shock with respect to the ambient gas:

$$\frac{\rho_2}{\rho_1} = \frac{(1+\gamma)\, M_1^2}{2 + (\gamma - 1)\, M_1^2}, \quad (4)$$

where $\gamma = 5/3$ is the adiabatic index for monatomic gas. From (4), we obtain $M_1 = 1.71^{+0.45}_{-0.24}$ at a 68% confidence level (see Fig. 3).

The derived value of M_1 corresponds to the gas temperature jump $T_2/T_1 = 1.72^{+0.55}_{-0.28}$. In principle, measuring such a temperature discontinuity would be an independent test of the validity of the interpretation of the observed structure as a shock wave. Unfortunately, the available Chandra and XMM observations of A754 do not allow us to determine the gas temperature outside the shock because of the low signal-to-noise ratio. Inside the shock, the temperature is measured reliably, $T_2 = 10$ keV (Markevitch *et al.* 2003), from the Chandra data.

A useful quantity is the shock velocity relative to the gas on the inner side of the discontinuity:

$$M_2 = \left(\frac{2 + (\gamma - 1) M_1^2}{2\gamma M_1^2 - (\gamma - 1)}\right)^{1/2} = 0.66 \pm 0.07. \quad (5)$$

The measured value of T_2 allows us to determine the speed of sound and, hence, the absolute shock velocity: $v_2 = 1070 \pm 115$ km s^{-1} and $v_1 = 2100^{+200}_{-150}$ km s^{-1}.

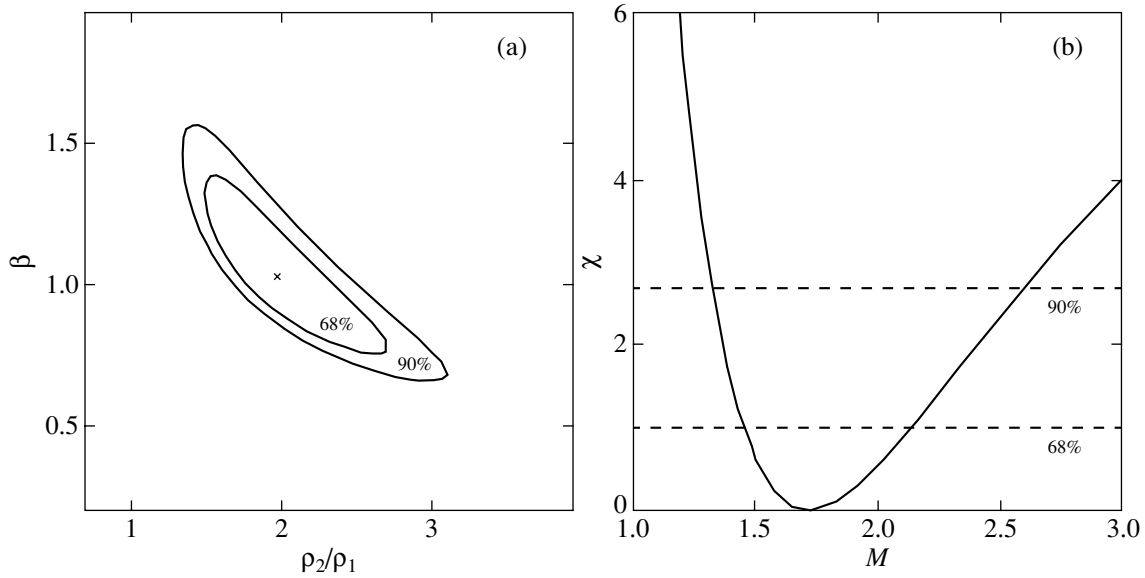

Fig. 3. The 68% and 90% confidence regions for two parameters of our model of intergalactic-gas radiation: the gas density ratio at the shock boundary and the parameter β in the outer part of the cluster (see Eq. (2)). (a) The cross marks the point that corresponds to the best-fit parameters; (b) χ^2 versus Mach number.

The measured Mach number of the shock wave in the cluster of galaxies A754 is close to its theoretically expected values for merging clusters: $M = 2$–3 (Sarazin 2002). This study is valuable in that the measurements of shock parameters in clusters are still quite scarce (Cyg A, Markevitch *et al.* 1999; A3667, Vikhlinin *et al.* 2002; 1E0657–56, Markevitch *et al.* 2002).

ACKNOWLEDGMENTS

This work was supported by the Russian Foundation for Basic Research (project nos. 00-02-1724 and 00-15-96699), the Commission of the Russian Academy of Sciences for Work with Young Scientists, and the Program of the Russian Academy of Sciences "Nonstationary Astronomical Phenomena."

REFERENCES

1. A. Cavaliere and R. Fusco-Femiano, Astron. Astrophys. **49**, 137 (1976).
2. M. Henriksen and M. Markevitch, Astrophys. J. **466**, L79 (1996).
3. C. Jones and W. Forman, Astrophys. J. **276**, 38 (1984).
4. L. D. Landau and E. M. Lifshitz, *Hydrodynamics* (Nauka, Moscow, 1988).
5. M. Markevitch, A. H. González, L. David, *et al.*, Astrophys. J. **567**, L27 (2002).
6. M. Markevitch, P. Mazzota, A. Vikhlinin, *et al.*, Astrophys. J. (2003, in press).
7. M. Markevitch, T. J. Ponman, P. E.J. Nulsen, *et al.*, Astrophys. J. **541**, 542 (2000).
8. M. Markevitch, C. Sarazin, and A. Vikhlinin, Astrophys. J. **521**, 526 (1999).
9. M. Markevitch, A. Vikhlinin, and P. Mazzota, Astrophys. J. **562**, L153 (2001).
10. C. Sarazin, Astrophys. Space Sci. **272**, 1 (2002).
11. S. L. Snowden, D. McCammon, D. N. Burrows, *et al.*, Astrophys. J. **424**, 714 (1994).
12. A. Vikhlinin and M. Markevitch, Pis'ma Astron. Zh. **28**, 563 (2002) [Astron. Lett. **28**, 495 (2002)].

Translated by G. Rudnitskii

Astronomy Letters, Vol. 29, No. 7, 2003, pp. 429–436. Translated from Pis'ma v Astronomicheskiĭ Zhurnal, Vol. 29, No. 7, 2003, pp. 488–496.

The Structure and Evolution of M 51-Type Galaxies

V. P. Reshetnikov* **and S. A. Klimanov**

Astronomical Institute, St. Petersburg State University, Universitetskii pr. 28, Petrodvorets, 198504 Russia

Received February 3, 2003

Abstract—We discuss the integrated kinematic parameters of 20 M 51-type binary galaxies. A comparison of the orbital masses of the galaxies with the sum of the individual masses suggests that moderately massive dark halos surround bright spiral galaxies. The relative velocities of the galaxies in binary systems were found to decrease with increasing relative luminosity of the satellite. We obtained evidence that the Tully–Fisher relation for binary members could be flatter than that for local field galaxies. An enhanced star formation rate in the binary members may be responsible for this effect. In most binary systems, the direction of the orbital motion of the satellite coincides with the direction of the rotation of the main galaxy. Seven candidates for distant M 51-type objects were found in the Northern and Southern Hubble Deep Fields. A comparison of this number with the statistics of nearby galaxies provides evidence for the rapid evolution of the space density of M 51-type galaxies with redshift z. We assume that M 51-type binary systems could be formed through the capture of a satellite by a massive spiral galaxy. It is also possible that the main galaxy and its satellite in some of the systems have a common cosmological origin.

Key words: *galaxies, groups and clusters of galaxies, intergalactic gas.*

1. INTRODUCTION

M 51-type (NGC 5194/95) binary systems consist of a spiral galaxy and a satellite located near the end of the spiral arm of the main component. Previously (Klimanov and Reshetnikov 2001), we analyzed the optical images of about 150 objects that were classified by Vorontsov-Vel'yaminov (1962–1968) as galaxies of this type. Based on this analysis, we made a sample of 32 objects that are most likely to be M 51-type galaxies. By analyzing the sample galaxies, we were able to formulate empirical criteria for classifying a binary system as an object of this type (Klimanov and Reshetnikov 2001): (1) the B-band luminosity ratio of the components ranges from 1/30 to 1/3 and (2) the satellite lies at a distance that does not exceed two optical diameters of the main component.

Klimanov *et al.* (2002) presented the results of spectroscopic observations of 12 galaxies from our list of M 51-type objects, including rotation curves for the main galaxies and line-of-sight velocities for their satellites. Together with previously published results of other authors, we have access to kinematic data for most (20 objects) of our selected M 51-type galaxies. Here, we analyze the observational data for the galaxies of our sample. All of the distance-dependent quantities were determined by using the Hubble constant $H_0 = 75$ km s^{-1} Mpc^{-1} (except in Section 4).

2. MEAN PARAMETERS OF THE GALAXY SAMPLE

The kinematic parameters for 12 binary systems were published by Klimanov *et al.* (2002) (see Fig. 1 and the table in this paper). The corresponding data for eight more systems from our list (object nos. 6, 10, 13, 14, 19, 21, 25, and 27; see Table 7 and Fig. 7 in Klimanov and Reshetnikov 2001) were taken from the LEDA and NED databases.

The mean B-band absolute magnitude of the main galaxy for 20 binary systems is $-20^m.6 \pm 0^m.3$ (below, the standard deviation from the mean is given as the error). Therefore, the main components are relatively bright galaxies comparable in luminosity to the Milky Way. The mean luminosity ratio of the satellite and the main galaxy is 0.16 ± 0.04. The mean apparent flattenings of the main galaxy ($\langle b/a \rangle = 0.61 \pm 0.04$) and its satellite ($0.66 \pm 0.03$) roughly correspond to the expected flattening of a randomly oriented thin disk ($2/\pi = 0.64$). The satellites lie at a projected distance of $\langle X \rangle = 19.0 \pm 2.7$ kpc or, in fractions of the standard optical radius R_{25} measured from the $\mu(B) = 25^m$ arcsec^{-2} isophote, at a distance of $(1.39 \pm 0.11)R_{25}$. In going from the projected linear distance to the true separation, we find that

*E-mail: resh@astro.spbu.ru

1063-7737/03/2907-0429$24.00

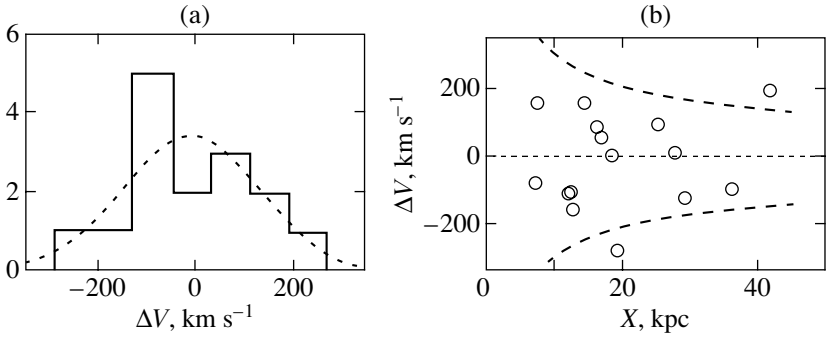

Fig. 1. (a) The distribution of observed line-of-sight velocity differences between the main galaxy and its satellite. (b) The velocity difference between the main galaxy and its satellite versus the projected linear separation between them.

the satellites are separated by a mean distance of $\approx 4/\pi \times 1.39 R_{25} = 1.8 R_{25}$.

The mean maximum rotation velocity of the main galaxy corrected for the inclination of the galactic plane and for the deviation of the spectrograph slit position from the major axis (see the next section for more details) is $\langle V_{\max} \rangle = 190 \pm 19$ km s^{-1}. If we exclude the galaxies with $b/a > 0.7$ seen almost face-on, then this value increases to 203 ± 16 km s^{-1} (12 pairs).

The mean difference between the line-of-sight velocities of the galaxies and their satellites is $\langle \Delta V \rangle = -9 \pm 35$ km s^{-1}. The absolute value of this difference, i.e., the difference with no sign, is 115 ± 18 km s^{-1}. The relatively low values of ΔV suggest that all objects of our sample are physical pairs. Remarkably, the mean absolute value of the velocity difference for M 51-type galaxies is close to that (137 ± 6 km s^{-1}) for 487 galaxy pairs from the catalog of Karachentsev (1987) with a ratio of the orbital mass of the pair to the total luminosity of its components $f < 100$. Note also that the measurement error of ΔV in Klimanov *et al.* (2002) is, on average, only 20 km s^{-1}.

Figure 1a (left panel) shows the observed ΔV distribution. To a first approximation, this distribution can be described by a Gaussian with the standard deviation $\sigma = 140$ km s^{-1} (dotted line). Figure 1b shows a plot of the difference ΔV against the projected linear separation between the main galaxy and its satellite. The dashed lines in the figure represent the expected (Keplerian) dependences for a point mass with $M_{\rm tot} = 2 \times 10^{11} M_\odot$ located at the center of the system.

Let us compare the mean values of the individual and orbital mass estimates for M 51-type galaxies. For a sample of binary galaxies with a randomly oriented plane of the circular orbit with respect to the line of sight, the total mass of the components can be found as $M_{\rm orb} = (32/3\pi)(X\Delta V^2/G)$, where G is the gravitational constant (Karachentsev 1987). For the objects of our sample, $\langle M_{\rm orb} \rangle = (2.9 \pm 1.0) \times 10^{11} M_\odot$. We will determine the individual masses of the main components by using the maximum rotation velocities (see the next section) and by assuming that the rotation curves of the galaxies within their optical radii are flat. For a spherical distribution of matter, we then obtain the mean mass of the main galaxy, $\langle M_{\rm main} \rangle = (1.6 \pm 0.4) \times 10^{11} M_\odot$, and the mass-to-luminosity ratio, $\langle M_{\rm main}/L_{\rm main}(B) \rangle = 4.7 \pm 0.9 M_\odot/L_{\odot,B}$. The ratio of the orbital mass of M 51-type systems to the mass of the main galaxy for the objects under consideration is 1.9 ± 0.5. Given

Candidates for M 51-type galaxies in the Hubble Deep Fields

Name	I_{814}	z	Spectral type	X
n45	21.26	1.012	Scd	2″.95
n78	25.30	1.04:	Irr	
n350	21.27	0.320	Scd	3.36
n351	24.03	0.24:	Irr	
n888a	23.88	0.559	Irr	0.72
n888b	25.75			
n938a	23.11	0.557	Scd	1.37
n938b	25.85			
SB-WF-2033-3411a	22.76	0.55:	Irr	1.44
SB-WF-2033-3411b	24.94			
SB-WF-2736-0920a	22.01	0.59:	Scd	1.54
SB-WF-2736-0920b	24.30			
SB-WF-2782-4400a	23.05	0.53:	Irr	0.89
SB-WF-2782-4400b	24.58			

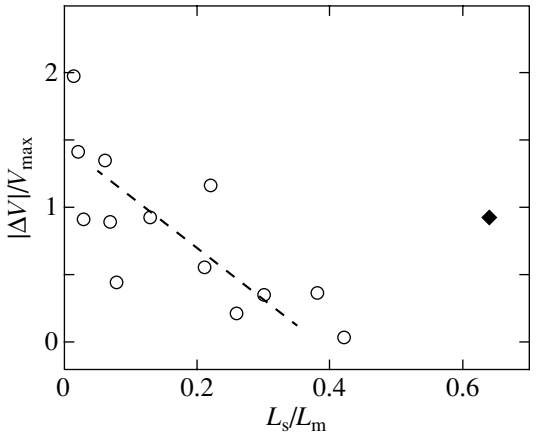

Fig. 2. The relation between the satellite's relative orbital velocity and the luminosity ratio of the satellite and the main galaxy.

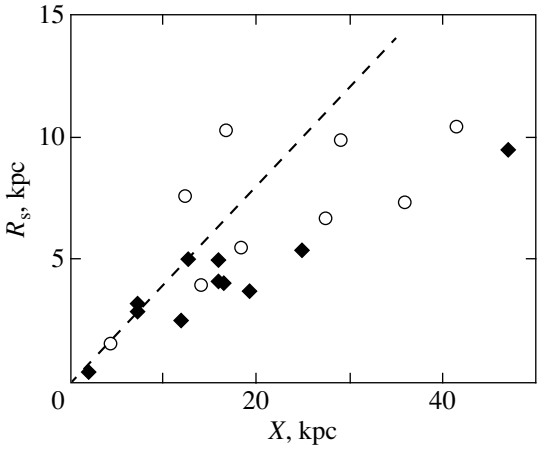

Fig. 3. The relation between the observed optical radius of the satellite and the projected linear distance to the main galaxy. The parameters of the satellites with $L_s/L_m > 0.1$ and $L_s/L_m \leq 0.1$ are indicated by the circles and diamonds, respectively. The straight line indicates the expected values of the tidal radius for a central point mass (which approximates the main galaxy) and a mass ratio of the satellite and the main galaxy equal to 1/3.

the satellite's mass, the ratio of the orbital mass of the system to the total mass of the two galaxies is ≈1.6 (for a fixed mass-to-luminosity ratio and a mean luminosity ratio of the satellite and the main galaxy equal to 0.16). If the orbits of the satellites are assumed to be not circular but elliptical with a mean eccentricity $e = 0.7$ (Ghigna *et al.* 1998), then the orbital mass estimate increases by a factor of 1.5 (Karachentsev 1987). The ratio of the orbital mass of the system to the total mass of the two galaxies also increases by a factor of 1.5 (to 2.4). Consequently, we obtained evidence for the existence of moderately massive dark halos around bright spiral galaxies within $(1.5–2)R_{25}$.

In Fig. 2, $k = |\Delta V|/V_{max}$ is plotted against the ratio of the observed B-band luminosities of the satellite and the main galaxy (L_s/L_m), where V_{max} is the maximum rotation velocity of the main galaxy. If $|\Delta V|/V_{max}$ is close to unity, then the relative velocity of the satellite is approximately equal to the disk rotation velocity of the main galaxy; if $k \approx 0$, then the satellite's observed velocity is close to the velocity of the main galaxy. We see a clear trend in the figure: relatively more massive satellites show lower values of k. If we restrict our analysis to satellites with $L_s/L_m < 0.5$ (circles), then the correlation coefficient of the dependence shown in Fig. 2 is −0.77; i.e., the correlation is statistically significant at $P > 99\%$ (the diamond in the figure indicates the parameters of the system NGC 3808A,B with $L_c/L_m = 0.64$). The corresponding linear fit is indicated in the figure by the dashed straight line. Low-mass satellites with $L_c/L_m < 0.2$ are located, on average, on the extension of the rotation curve for the main galaxy and have velocities close to V_{max} (for them, $\langle k \rangle = 1.13 \pm 0.19$). More massive satellites with $0.2 < L_s/L_m < 0.5$ have a lower relative velocity: $\langle k \rangle = 0.52 \pm 0.15$.

There is another curious trend: more distant satellites are, on average, more massive. This trend can be explained by observational selection when choosing candidates for M 51-type galaxies. Another plausible explanation is that the massive satellites located near the main galaxy have a shorter evolution scale, because the characteristic lifetime of a satellite near a massive galaxy due to dynamical friction is inversely proportional to the satellite's mass (Binney and Tremaine 1987).

The optical radius of the satellite is plotted against the projected linear distance to the center of the main galaxy in Fig. 3. The dashed straight line in the figure indicates the expected tidal radius of the satellite as a function of the distance to the point mass (Binney and Tremaine 1987); the mass ratio of the satellite and the main galaxy was taken to be 1/3 (this was done in accordance with our formal criterion for classifying a system as being of the M 51 type (see the Introduction)). As we see from the figure, in general, the satellites satisfy the tidal constraint imposed on their sizes. Moreover, the relatively more (circles) and less (diamonds) massive satellites show steeper and flatter dependences, respectively. If the satellite's size is limited by the tidal effect of the main component, then this is to be expected, because the tidal radius is roughly proportional to $(M_s/M_m)^{1/3}$, where M_s/M_m is the mass ratio of the satellite and the main galaxy (Binney and Tremaine 1987).

In ten of the twelve binary systems whose observations are presented in Klimanov *et al.* (2002), the satellite moves relative to the dynamic center

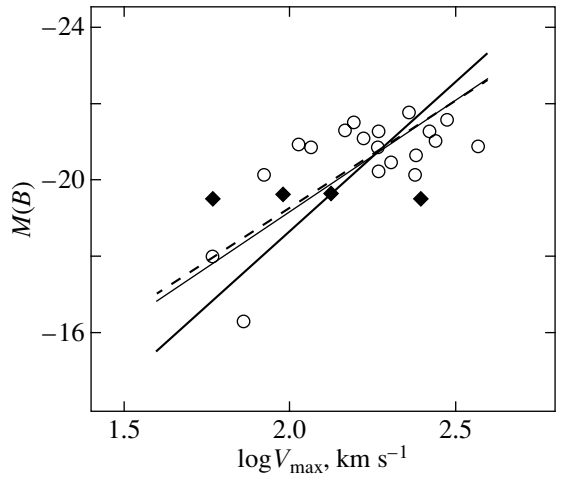

Fig. 4. The Tully–Fisher relation for M 51-type galaxies. The parameters of the main galaxies and their satellites are indicated by the circles and diamonds, respectively. The heavy solid straight line represents the TF relation for spiral galaxies as constructed by Tully *et al.* (1998) and the dashed line represents our TF relation for M 51-type galaxies; the thin straight line indicates the TF relation for spiral galaxies at $z \sim 0.5$ (Ziegler *et al.* 2002).

of the main component in the same direction as the direction of rotation of the part of the main galaxy's disk facing it. In two cases (NGC 2535/36 and NGC 4137), the motion of the satellite may be retrograde, although both main galaxies in these systems are seen almost face-on and this conclusion is preliminary.

3. THE TULLY–FISHER RELATION

The relation between luminosity and rotation velocity (the Tully–Fisher (TF) relation) is one of the most fundamental correlations for spiral galaxies. This relation is widely used to study the large-scale spatial distribution of galaxies. In addition, it is an important test for the various kinds of models that describe the formation and evolution of spiral galaxies.

The observed rotation curves of M 51-type galaxies are often highly irregular (see Fig. 1 in Klimanov *et al.* 2002). Therefore, to estimate the maximum rotation velocity, we used the empirical fit to the rotation curve suggested by Courteau (1997):

$$v(r) = v_0 + v_c(1+x)^{\beta}(1+x^{\gamma})^{-1/\gamma},$$

where r is the distance from the dynamical center, v_0 is the line-of-sight velocity of the dynamical center, v_c is the asymptotic rotation velocity, and $x = r_t/r$ (β, γ, and r_t are the parameters). This formula well represents the rotation curves for most spiral galaxies (Courteau 1997).

Figure 4 shows the distribution of the parameters of M 51-type galaxies in the absolute magnitude ($M(B)$)—maximum rotation velocity ($V_{\max}$) plane. The values of $M(B)$ for the sample objects were corrected for internal extinction, as prescribed by the LEDA database. We took the values of v_c (see above) obtained by fitting the observed rotation curves as the maximum rotation velocity for most objects. In addition, these values were corrected in a standard way for the disk inclination to the line of sight and for the deviation of the spectrograph slit position from the galaxy's major axis. For eight galaxies, we estimated $V_{\max}$ from the LEDA H I line widths.

As we see from Fig. 4, the parameters of M 51-type galaxies are located along a flatter relation than are those of nearby spiral galaxies. The mean relation for the objects of our sample indicated by the dashed straight line is $L(B) \propto V_{\max}^{-(2.2\pm0.6)}$, while the relation for local field spiral galaxies is $L(B) \propto V_{\max}^{-(3.1-3.2)}$ (Tully *et al.* 1998; Sakai *et al.* 2000). The bright (massive) binary members are located near the standard relation (Fig. 4). This location is consistent with the conclusion that the TF relation for giant spiral galaxies does not depend on their spatial environment (Evstigneeva and Reshetnikov 2001). The M 51-type galaxies with $V_{\max} \leq 150$ km s^{-1} lie, on average, above the relation for single galaxies and, at a fixed $V_{\max}$, show a higher luminosity (or, conversely, at the same luminosity, they are characterized by, on average, lower observed values of $V_{\max}$).

A similar fact (a different TF relation for the members of interacting galaxy systems and an excess luminosity of the low-mass members of these systems) was, probably, first pointed out by Reshetnikov (1994). The members of close pairs of galaxies also exhibit a flatter TF relation: $L(R) \propto V_{\max}^{-2.2}$ (Barton *et al.* 2001). Barton *et al.* (2001) argue that interaction-triggered violent star formation in galaxies could be mainly responsible for the different slope of the TF relation for the binary members. Starbursts more strongly affect the observed luminosities of the low-mass galaxies by taking them away from the standard TF relation.

Violent star formation also appears to be responsible for the flatter TF relation for M 51-type galaxies. As we showed previously (Klimanov and Reshetnikov 2001), IRAS data on the far-infrared radiation from galaxies suggest an enhanced star-formation rate in M 51-type systems compared to local field objects. Unfortunately, the IRAS angular resolution is too low to separate the contributions from the main galaxy and its satellite to the observed radiation. Figure 4 provides circumstantial evidence for violent star formation in both binary components.

Interestingly, a flatter TF relation has also been recently found (Ziegler *et al.* 2002) for spiral galaxies at redshifts $z \sim 0.5$ (see Fig. 4). The similarity between the TF relations for nearby interacting/binary galaxies and distant spirals suggests that violent star formation triggered by interaction (mergers) could be responsible for the observed luminosity evolution in distant low-mass galaxies. The rate of interactions and mergers between galaxies rapidly increases toward $z \sim 1$ (Le Fevre *et al.* 2000; Reshetnikov 2000). This mechanism must undoubtedly contribute to the luminosity evolution and, hence, to the observed TF relation.

4. EVOLUTION OF THE FREQUENCY OF OCCURRENCE OF M 51-TYPE GALAXIES

Let us consider how the space density of M 51-type galaxies changes with increasing redshift z. To this end, we studied the original frames of the Northern and Southern Hubble Deep Fields (Ferguson *et al.* 2000) and selected candidates for distant objects of this type. In selecting objects, we used the same criteria as those used to make the sample of nearby galaxies. Unfortunately, there are no published spectroscopic z estimates simultaneously for the main galaxy and for its satellite for any of the systems.

Each of the Deep Fields contains several thousand galaxies; the images of many of them are seen in projection closely or superimposed on one another, which makes it difficult to select candidates for M 51-type objects. Therefore, we restricted our analysis only to relatively bright and nearby galaxies ($z < 1.1$).

The candidates for distant M 51-type objects are listed in the table. The first column of the table gives the galaxy name from the catalog of Fernandez-Soto *et al.* (1999) (the first four and last three objects are located in the Northern and Southern Fields, respectively); the second column gives the galaxy's apparent magnitude in the HST I_{814} filter (for the first two systems, we took the estimates from the catalog of Fernandez-Soto *et al.*; for the remaining systems, we provided our own magnitude estimates); the third column gives the redshift (the spectroscopic z estimates (Cohen *et al.* 2000) are given with three significant figures; the photometric z estimates (Fernandez-Soto *et al.* 1999) are marked by a colon); the fourth column gives the spectral type, which characterizes the galaxy's spectral energy distribution (Fernandez-Soto *et al.* 1999); and the last column contains our measurements of the angular separation between the nuclei of the main galaxy and its satellite.

The integrated parameters of the selected candidates for M 51-type systems are close, within the error limits, to those of nearby systems (see Section 2). Thus, the ratio of the observed luminosities of the satellite and the main galaxy is 0.13 ± 0.07 (in the I_{814} filter, which roughly corresponds to the B band in the frame of reference associated with the objects themselves at the mean redshift of the sample under consideration); the mean observed separation between the main components and their satellites is 12 ± 7 kpc. The absolute magnitude of the main galaxies that was estimated by applying the k correction (Lilly *et al.* 1995) is $M(B) = -19\overset{m}{.}4 \pm 1\overset{m}{.}4$. (These values, as well as those given below, were calculated for a cosmological model with a nonzero Λ term: $\Omega_m = 0.3$, $\Omega_\Lambda = 0.7$, and $H_0 = 65$ km s^{-1} Mpc^{-1}.

To estimate the evolution rate of the space density of galaxies with z, we use the same approach that was used by Reshetnikov (2000). By assuming that the space density of M 51-type galaxies changes as

$$n(z) = n_0(1+z)^m$$

($n(z)$ is the number of objects per unit volume (Mpc^3) at redshift z and $n_0 = n(z=0)$), we calculate the expected number of galaxies in the direction of the Deep Fields in the z range of interest for various exponents m.

The most important parameter required for this estimation is the spatial abundance of M 51-type galaxies in the region of the Universe close to us (n_0). According to Klimanov (2003), M 51-type galaxies account for 0.3% of the field galaxies and about 4% of the binary galaxies. Interestingly, this estimate is close to the frequency of occurrence estimated by Vorontsov-Vel'yaminov (1975), who assumed that M 51-type galaxies accounted for about 10% of the interacting galaxies. Assuming that about 5% of the galaxies are members of interacting systems (Karachentsev and Makarov 1999), we find that M 51-type systems account for $\approx$0.5% of all galaxies. By integrating the luminosity function of the field galaxies taken from the SDSS and 2dF surveys (Blanton *et al.* 2001; Norberg *et al.* 2002) in the range of absolute magnitudes $M(B)$ from -17^m to $-22\overset{m}{.}5$, we can estimate the space density of field galaxies in this luminosity range as 0.017 Mpc^{-3} and, hence, $n_0 = 5.1 \times 10^{-5}$ Mpc^{-3}.

Integrating the expression $n_0(1+z)^m$ over the z range from 0.2 to 1.1, we found that in the absence of density evolution ($m = 0$), the expected number of M 51-type galaxies in the two fields is 0.8. The observed number of objects (seven) exceeds their expected number by more than two standard Poisson deviations ($\sigma = \sqrt{7} = 2.65$). Despite the poor statistics, this result provides evidence for the evolution of the spatial abundance of M 51-type objects with z.

The exponent $m = 3.6$ corresponds to the observed number of galaxies. The formal spread in this value that corresponds to the range of the number of objects from $7 - \sqrt{7}$ to $7 + \sqrt{7}$ is $^{+0.5}_{-0.8}$. The actual error in the m estimate may be much larger, for example, because of the uncertainty in n_0.

Of course, the estimated evolution rate depends on the assumed cosmological model. For example, for a flat Universe with a zero Λ term and $H_0 = 75$ km s^{-1} Mpc^{-1}, the exponent m increases to 4.8.

5. DISCUSSION

A typical M 51-type binary system is a bright spiral galaxy with a relatively low-mass satellite physically associated with it located near the boundary of its disk. In most cases, the satellite shows prograde motion; i.e., it rotates in the same direction as the main galaxy (see Section 2). Observational selection may be responsible for this peculiarity, because the satellite whose direction of orbital motion coincides with the direction of rotation of the main galaxy can excite and maintain a large-scale two-arm pattern in the galactic disk. If the motion of the satellite is retrograde, then the tidal response will be much weaker. The presence of a spiral pattern is one of the criteria for classifying a galaxy as an M 51-type object, and three quarters of them show a large-scale two-arm pattern (Klimanov and Reshetnikov 2001). Consequently, the predominance of prograde motions of the satellites in objects with a well-developed two-arm spiral pattern can serve as a confirmation of the tidal nature of the spiral arms in such galaxies.

Other indications of the mutual influence of the galaxies in M 51-type systems include an enhanced star-formation rate (as evidenced by the high far-infrared luminosities of the systems (Klimanov and Reshetnikov 2001) and, possibly, by a flatter Tully–Fisher relation (Fig. 4)) and the existence of a tidal constraint on the sizes of the satellites (Fig. 3).

M 51-type binary systems are relatively rare objects. According to Klimanov (2003), only $\sim$0.7% of the spiral galaxies in the range of absolute B magnitudes from -16^m to -22^m have a relatively bright satellite near the end of the spiral arm and can be classified as objects of this type.

As was shown in the preceding section, the fraction of M 51-type galaxies increases with redshift. Interestingly, within the error limits, the rate of increase in the relative abundance of these objects ($m = 3.6^{+0.5}_{-0.8}$) roughly corresponds to the rate of increase in the number of binary and interacting galaxies. Thus, the fraction of galaxies with tidal features is proportional to $(1 + z)^m$ with $m = 4 \pm 1$ (Reshetnikov 2000); the fractions of merging and binary galaxies evolve with $m = 3.4 \pm 0.6$ and 2.7 ± 0.6, respectively (Le Fevre *et al.* 2000).

Let us now try to describe the possible origin and evolution of M 51-type binary systems. Numerical calculations of the formation of galaxies performed in terms of CDM (cold dark matter) models indicate that galaxies are formed inside extended dark halos; many less massive subhalos must be contained inside a massive halo (see, e.g., Kauffmann *et al.* 1993; Klypin *et al.* 1999). Thus, the halo of a galaxy with a mass comparable to the mass of the Milky Way must include several tens of satellites of different masses within its virial radius of 200–300 kpc (Benson *et al.* 2002a). Numerical calculations suggest that $\leq$5% of the galaxies similar to the Milky Way have satellites with a V-band luminosity of -18^m (Benson *et al.* 2002b). Consequently, such satellites (their luminosity is typical of the satellites of M 51-type objects) are relatively but not extremely rare. Recall that our Galaxy has such a satellite, the Large Magellanic Cloud, at a distance of about 50 kpc.

What is the subsequent fate of the relatively massive satellites formed in the halos of galaxies similar to the Milky Way? The evolution of the satellites will be governed mainly by two processes: (1) dynamical friction, which will cause the satellite's orbital decay until the satellite merges with the main component; and (2) tidal stripping, which causes a decrease in the satellite's mass and, as a result, an increase in the lifetime of its separate existence from the main galaxy. Recent studies suggest that the lifetime of a satellite under dynamical friction can be much longer than assumed previously (see, e.g., Colpi *et al.* 1999; Hashimoto *et al.* 2003). In addition, this lifetime weakly depends on the orbital eccentricity of the satellite (Colpi *et al.* 1999).

Cosmological calculations indicate that the satellites formed within the massive halo of a central object are in highly elongated orbits with a mean eccentricity of $e = 0.6$–0.8 (Ghigna *et al.* 1998). If such satellites are assumed to be observed in M 51-type systems mostly near the orbital pericenter (in this case, their tidal effect on the disk of the main galaxy is at a maximum), i.e., $r_\Pi = 24$ kpc, then the distance at the apocenter is 100–150 kpc and the orbital period of the satellite is 3–6 Gyr. In Hubble time, such a satellite would make only 2 to 4 turns and might not be absorbed by the central galaxy by $z = 0$. During its first encounter with the main galaxy, the satellite can lose $\sim$50% of its mass, which significantly increases the time of its orbital evolution (Colpi *et al.* 1999). Consequently, the "cosmological" satellites formed on the periphery of the halos of central galaxies could in several cases survive by $z = 0$ and be observed together with the main components as M 51-type binary systems.

Another, apparently more plausible scenario for the formation of the binary systems under consideration is the capture of a relatively low-mass object by a central galaxy during their chance encounter. At present, the interactions of galaxies are relatively rare events, but they are observed more and more often with increasing z (at least up to $z \approx 1$). Whereas only $\approx 5\%$ of the galaxies at $z = 0$ are members of interacting systems with clear morphological evidence of perturbation (Karachentsev and Makarov 1999), this fraction at $z = 1$ is $\approx 50\%$ (Reshetnikov 2000; Le Fevre *et al.* 2000). Thus, an event during which a massive galaxy at $z \geq 0.5$ captures a satellite seems quite likely. This event is all the more likely since the peculiar velocities of the galaxies were earlier lower and, hence, their chance encounters occurred with lower relative velocities and, more often, led to the formation of bound systems or mergers (see, e.g., Balland *et al.* 1998). The orbital period in a circular orbit with a semimajor axis of $a = 24$ kpc around a galaxy similar to the Milky Way after 0.5–1 Gyr. Consequently, in several Gyr (recall that an age equal to about half of the Hubble time corresponds to $z = 1$), most of such satellites will be absorbed by the main galaxies (Colpi *et al.* 1999; Penarrubia *et al.* 2002); by the time that corresponds to $z = 0$, they should be observed rarely. This scenario is confirmed by our evidence for the relatively rapid evolution of the space density of M 51-type objects with z.

Thus, the currently observed M 51-type systems could have both a primordial origin and a more recent origin—through the capture of a satellite by the main galaxy. Mixed scenarios are also possible, for example, when an encounter with another galaxy can change the orbit of the peripheral satellite and push it closer to the main galaxy. Of course, the actual pattern of formation and evolution of the binary systems under consideration is much more complex, and it should be tested by numerical calculations.

How does the galaxy M 51, the prototype of this class of objects, fit into the scenarios described above? It should be noted that in some respects, this binary system is not a typical representative of the M 51-type systems. For example, the mass ratio of the satellite and the main galaxy for it is 1/3 or even 1/2, a value that is larger than that for a typical binary system of this type. The dynamical structure of the binary system is not completely understood either. The apparent morphology and kinematics of M 51 can be explained both in terms of the models according to which we observe the separation of the galaxies after their first encounter (Durrell *et al.* 2003) and in terms of the approach according to which multiple encounters of the satellite and the main galaxy have already taken place in this system (Salo and Laurikainen 2000). In the former case, the system M 51 has, probably, formed recently (we are observing it several hundred Myr after the passage of the satellite through the pericenter) during a close encounter of the galaxies NGC 5194 and NGC 5195; in the latter case, this system is much older and its age can reach several Gyr.

In conclusion, note that because of the relatively small number of systems studied, some of our results (a different slope of the TF relation and an increase in the frequency of occurrence of M 51-type galaxies with z) are preliminary and should be confirmed using more extensive observational data.

ACKNOWLEDGMENTS

This study was supported by the Federal Program "Astronomy" (project no. 40.022.1.1.1101).

REFERENCES

1. Ch. Balland, J. Silk, and R. Schaeffer, Astrophys. J. **497**, 541 (1998).
2. E. J. Barton, M. J. Geller, B. C. Bromley, *et al.*, Astron. J. **121**, 625 (2001).
3. A. J. Benson, C. G. Lacey, C. M. Baugh, *et al.*, Mon. Not. R. Astron. Soc. **333**, 156 (2002a).
4. A. J. Benson, C. S. Frenk, C. G. Lacey, *et al.*, Mon. Not. R. Astron. Soc. **333**, 177 (2002b).
5. J. Binney and S. Tremaine, *Galactic Dynamics* (Cambridge University Press, Princeton, 1987).
6. M. R. Blanton, J. Dalcanton, D. Eisenstein, *et al.*, Astron. J. **121**, 2358 (2001).
7. J. G. Cohen, D. W. Hogg, R. Blandford, *et al.*, Astrophys. J. **538**, 29 (2000).
8. M. Colpi, L. Mayer, and F. Governato, Astrophys. J. **525**, 720 (1999).
9. S. Courteau, Astron. J. **114**, 2402 (1997).
10. P. R. Durrell, J. Ch. Mihos, J. J. Feldmeier, *et al.*, Astrophys. J. **582**, 170 (2003).
11. E. A. Evstigneeva and V. P. Reshetnikov, Astrofizika **44**, 193 (2001).
12. H. C. Ferguson, M. Dickinson, and R. Williams, Ann. Rev. Astron. Astrophys. **38**, 667 (2000).
13. A. Fernández-Soto, K. M. Lanzetta, and A. Yahil, Astrophys. J. **513**, 34 (1999).
14. S. Ghigna, B. Moore, F. Governato, *et al.*, Mon. Not. R. Astron. Soc. **300**, 146 (1998).
15. Y. Hashimoto, Y. Funato, and J. Makino, Astrophys. J. **582**, 196 (2003).
16. I. D. Karachentsev, *Binary Galaxies* (Nauka, Moscow, 1987).
17. I. D. Karachentsev and D. I. Makarov, *Galaxy Interactions at Low and High Redshift*, Ed. by J. E. Barnes and D. B. Sanders (1999), p. 109.
18. G. Kauffmann, S. D.M. White, and B. Guiderdoni, Mon. Not. R. Astron. Soc. **264**, 201 (1993).
19. S. A. Klimanov, Astrofizika (2003, in press).
20. S. A. Klimanov and V. P. Reshetnikov, Astron. Astrophys. **378**, 428 (2001).

21. S. A. Klimanov, V. P. Reshetnikov, and A. N. Burenkov, Pis'ma Astron. Zh. **28**, 643 (2002) [Astron. Lett. **28**, 579 (2002)].
22. A. Klypin, A. V. Kravtsov, O. Valenzuela, and F. Prada, Astrophys. J. **522**, 82 (1999).
23. O. Le Fevre, R. Abraham, S. J. Lilly, *et al.*, Mon. Not. R. Astron. Soc. **311**, 565 (2000).
24. S. J. Lilly, L. Tresse, F. Hammer, *et al.*, Astrophys. J. **455**, 108 (1995).
25. P. Norberg, Sh. Cole, C. M. Baugh, *et al.*, Mon. Not. R. Astron. Soc. **336**, 907 (2002).
26. J. Penarrubia, P. Kroupa, and Ch. M. Boily, Mon. Not. R. Astron. Soc. **333**, 779 (2002).
27. V. P. Reshetnikov, Astron. Astrophys. **353**, 92 (2000).
28. V. P. Reshetnikov, Astrophys. Space Sci. **211**, 155 (1994).
29. S. Sakai, J. R. Mould, S. M. G. Hughes, *et al.*, Astrophys. J. **529**, 698 (2000).
30. H. Salo and E. Laurikainen, Mon. Not. R. Astron. Soc. **319**, 377 (2000).
31. R. B. Tully, M. J. Pierce, J.-Sh. Huang, *et al.*, Astron. J. **115**, 2264 (1998).
32. B. A. Vorontsov-Vel'yaminov, Astron. Zh. **52**, 692 (1975) [Sov. Astron. **19**, 422 (1975)].
33. B. A. Vorontsov-Vel'yaminov, A. A. Krasnogorskaya, and V. P. Arkhipova, *A Morphological Catalog of Galaxies* (Izd. Mosk. Gos. Univ., Moscow, 1962–1968), Vols. 1–4.
34. B. L. Ziegler, A. Bohm, K. J. Fricker, *et al.*, Astrophys. J. Lett. **564**, L69 (2002).

Translated by V. Astakhov

Astronomy Letters, Vol. 29, No. 7, 2003, pp. 437–446. Translated from Pis'ma v Astronomicheskiĭ Zhurnal, Vol. 29, No. 7, 2003, pp. 497–507.

The Shape of the Rotation Curves of Edge-on Galaxies

A. V. Zasov[1]* and A. V. Khoperskov[2]

[1]*Sternberg Astronomical Institute, Universitetski pr. 13, Moscow, 119992 Russia*

[2]*Department of Theoretical Physics, Volgograd State University, Volgograd, 400068 Russia*

Received February 4, 2003

Abstract—We consider the effects of projection, internal absorption, and gas- or stellar-velocity dispersion on the measured rotation curves of galaxies with edge-on disks. Axisymmetric disk models clearly show that the rotational velocity in the inner galaxy is highly underestimated. As a result, an extended portion that imitates nearly rigid rotation appears. At galactocentric distances where the absorption is low (i.e., it does not exceed 0.3–0.5^m kpc^{-1}), the line profiles can have two peaks, and a rotation curve with minimum distortions can be obtained by estimating the position of the peak that corresponds to a higher rotational velocity. However, the high-velocity peak disappears in high-absorption regions and the actual shape of the rotation curve cannot be reproduced from line-of-sight velocity estimates. In general, the optical rotation curves for edge-on galaxies are of little use in reconstructing the mass distribution in the inner regions, particularly for galaxies with a steep velocity gradient in the central region. In this case, estimating the rotation velocities for outer (transparent) disk regions yields correct results. © *2003 MAIK "Nauka/Interperiodica".*

Key words: *galaxies—rotation and internal absorption.*

1. INTRODUCTION

The rotation curve $V(r)$ is the most important characteristic of disk galaxies. It not only provides information about the mass distribution but also allows empirical methods for determining the luminosity (distance) from the maximum rotational velocity to be used. For spiral galaxies with edge-on disks, constructing the rotation curve is difficult because of the following two complicating factors: projection and internal absorption. The two effects depend both on the shape of the rotation curve and on the distribution of the radiation sources and the absorbing medium in the galaxy.

The rotation curves or, to be more precise, one-dimensional line-of-sight velocity distributions over the disk were obtained for many edge-on galaxies. A distinctive feature of many of these galaxies is an extended region of rigid rotation (a monotonic increase in the velocity). A nearly linear increase in the line-of-sight velocity up to large galactocentric distances was pointed out in the first kinematic studies of galaxies with thin disks (Goad and Roberts 1981). These authors were, probably, the first to note that the rigidly rotating part of the rotation curve in edge-on galaxies could be an artifact and that the effects of a nonuniform dust distribution require drawing the envelope an that bounds the positions of the data points in the radius–measured rotational velocity diagram from above. Bosma *et al.* (1992) clearly showed the effect of absorption on the shape of the rotation curve by comparing the optical and radio rotation curves for two edge-on galaxies (NGC 801 and NGC 100). As was shown by these authors using simple dust-containing disk models as an example, absorption rather than light scattering by dust affects the observed rotation-velocity estimates. They found that the absorption effect significantly decreases only if the disk orientation differs from the "edge-on" orientation by more than 5°.

Subsequently, comparison of the shape of the rotation curve in the inner region with the disk inclination to the line of sight for a large number of galaxies confirmed that the gradient in the measured rotational velocity in the inner galaxy is actually lower for strongly inclined disks, and this effect is more pronounced for luminous galaxies, which, on average, exhibit stronger internal absorption (Giovanelli and Haynes 2002).

Curiously, at a sufficiently high optical depth, the effect of the diffuse dust medium on the mass estimate may prove to be significant not only for disk galaxies but also for slowly rotating (elliptical) galaxies (see Baes and Dejonghe (2000) and references therein).

More than 300 rotation curves for edge-on galaxies (from the Flat Galaxy Catalog (FGC) of Karachentsev *et al.* 1993) were obtained with the 6-m

*E-mail: zasov@sai.msu.ru

1063-7737/03/2907-0437$24.00

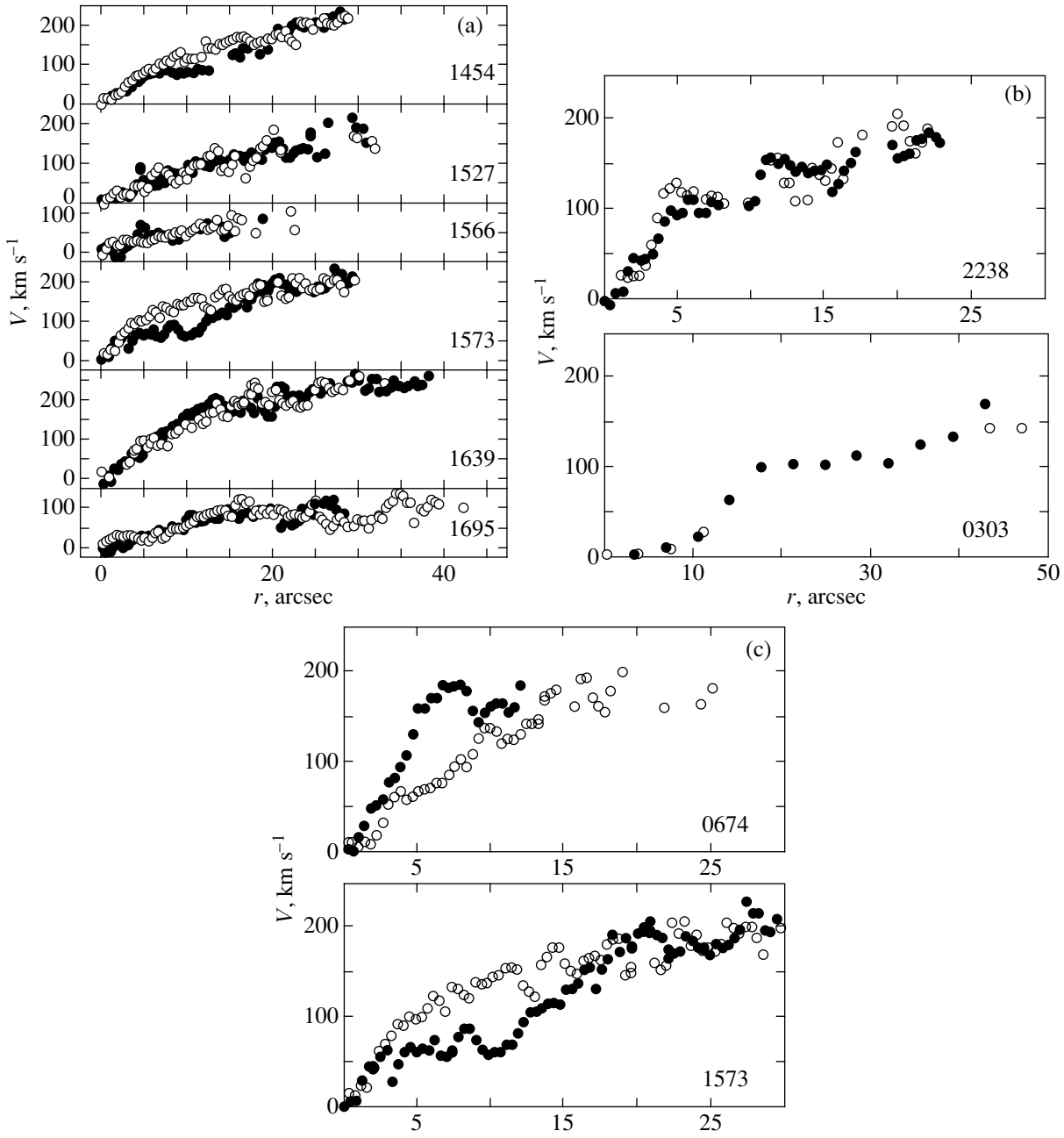

Fig. 1. Examples of the observed rotation curves for edge-on galaxies: (a) typical rotation curves; (b) examples of galaxies with a step on the rotation curve, and (c) examples of galaxies with different distributions of the measured velocities on different sides of the center. The filled and open circles correspond to the receding and approaching sides of the galaxy, respectively (Makarov *et al.* 1997, 1999; Karachentsev and Zhou Shu 1991). The galaxy number in the FGC catalog (Karachentsev *et al.* 1993) is indicated.

telescope at the Special Astrophysical Observatory of the Russian Academy of Sciences (see Makarov *et al.* (2000) and references therein). The measurements confirmed that the overwhelming majority of these galaxies have an extended rigidly rotating portion, which occasionally extends to the outer boundary of the measured rotation curve, although there are exceptions (Makarov *et al.* 1997a, 1997b, 1999). As an example, Fig. 1a shows several typical rotation curves for galaxies from Makarov *et al.* 1997a). Figures 1b and 1c illustrate less common features of the rotation curves, which are discussed below (in Subsections 3.2 and 3.3). The following questions arise in connection with the interpretation of the rotation curves: How do various effects affect the measured rotation velocities of such galaxies, and can the actual

rotation curve of the galaxy and an estimate of the maximum disk rotational velocity be directly obtained from observations?

Here, for axisymmetric galaxy models with given rotation curves, we compute the line-of-sight velocity distributions $V_s(x)$ along the major axis of an edge-on disk under various assumptions about the spatial distribution of the gas (star) density—both in the absence and in the presence of internal absorption in the galaxy.

2. GALAXY MODELS

2.1. Absorption-Free Models

The case with low internal absorption can actually apply to rotation-velocity measurements in the radio wavelength range or in galaxies with a very low interstellar dust abundance or to velocity measurements in the outer galaxy with a small optical depth τ.

In the absence of internal absorption, the maximum values of the Doppler rotational velocity component correspond to the regions located near a line perpendicular to the line of sight that crosses the galaxy along its diameter (we will arbitrarily call it the major axis of the galaxy). Therefore, the maximum-velocity estimates for sources at a given galactocentric distance must represent (to within the velocity dispersion) the actual circular rotational velocity. However, in general, this velocity will not necessarily correspond to the centroid (barycenter) of the line profile, because its position depends on the distribution of not only the velocity but also the volume luminosity along the line of sight.

We assume that the rotational velocity of the disk, as well as its brightness in the spectral line used to measure the velocity, are distributed axisymmetrically. Denote the volume luminosity in the line by $S(r)$. Let the x axis correspond to the major axis of the galaxy and the y axis be directed along the line of sight (Fig. 2a). The specific luminosity-weighted mean velocity along the line of sight is then given by the expression

$$V_s(x) = \frac{\int\limits_{-y_0}^{y_0} S(r)V_\varphi(r)\dfrac{x}{\sqrt{x^2+y^2}}dy}{\int\limits_{-y_0}^{y_0} S(r)dy}, \qquad (1)$$

where R is the disk radius, $r = \sqrt{x^2+y^2}$, and the integration limit is $y_0 = \sqrt{R^2-x^2}$.

Since the models are axisymmetric, below we assume that the distance from the disk center in the x projection is always positive.

Let us consider how the actual shape of the rotation curve $V_\varphi(r)$ and the peculiarities of the mass distribution in the disk affect the dependence $V_s(x)$ (the observed rotation curve).

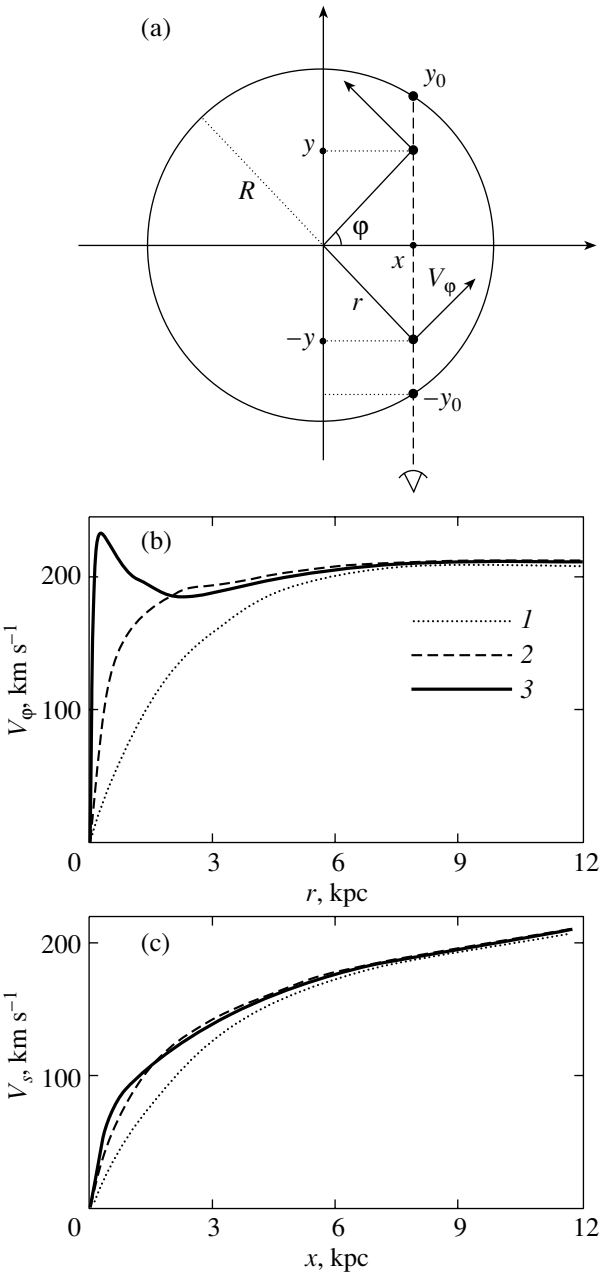

Fig. 2. (a) Determining the rotational velocity for an edge-on disk of radius R. At the point (x, y), the disk has the rotational velocity V_φ. The integration is performed from $-y_0$ to y_0. (b) The three types of rotation curves V_φ considered here (see also the text). (c) The line-of-sight velocity distribution relative to the center of the galaxy along its major axis $V_s(x)$ for the rotation curves shown in Fig. 2b without an allowance for internal absorption.

Let the disk volume luminosity in the spectral line used to estimate the velocity decrease exponentially with r:

$$S(r) = S_0 \exp(-r/L), \qquad (2)$$

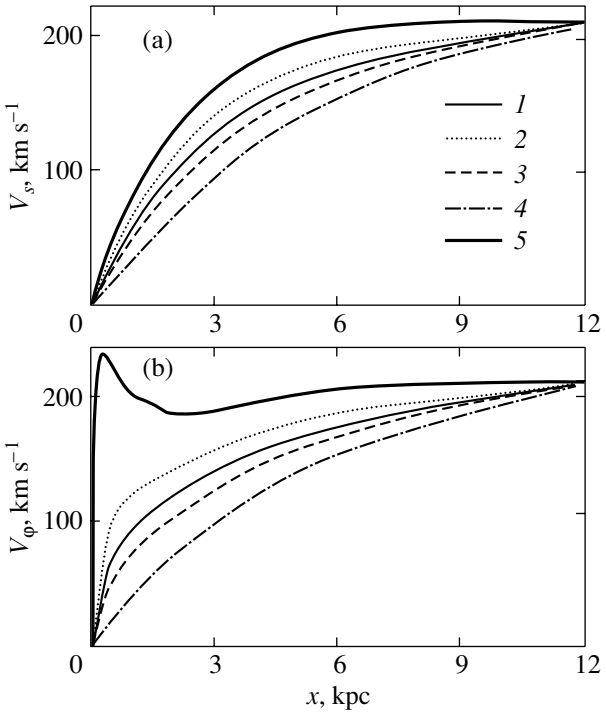

Fig. 3. The line-of-sight velocity distributions $V_s(x)$ for a gaseous disk with a chosen rotation curve (heavy lines). The models differ by the radial scale lengths L of the emission gas: $L =$ (*1*) 3, (*2*) 1.5, (*3*) 6, and (*4*) 6 kpc with an allowance made for the central ring; (a) for the rotation curve V_φ of the first type (line *1* in Fig. 2b), (b) for the rotation curve V_φ of the third type (line *3* in Fig. 2b).

where L is the radial scale length of the disk brightness in the emission line or, in the case where the velocities are determined from absorption lines, the radial scale length of the stellar disk. We assume, for certainty, that $R = 4L$. The disk contribution to the observed line profile is assumed to be zero at galactocentric distances $r > R$. As an illustration, we restrict our analysis to the following three types of rotation curves with different shapes in the inner disk ($r \lesssim 2L$) (Fig. 2b):

(1) the rotation curve $V_{\varphi 1}$ typical of galaxies without massive bulges (the dotted line in Fig. 2b),

(2) the rotation curve of the second type $V_{\varphi 2}$ that takes place in the case of a low-mass bulge responsible for the steeper velocity gradient in the inner galaxy (the dashed line in Fig. 2b), and

(3) the rotation curve $V_{\varphi 3}$ with a circumnuclear rotation velocity maximum (the solid line in Fig. 2b) that reflects the existence of a massive concentrated bulge.

In all of these cases, the rotation curve flattens out at large r.

Figure 2c shows the radial dependences of the disk velocity along the line of sight $V_s(x)$ calculated using formula (1) for the three types of rotation curves under consideration in the absence of absorption. As we see, in all of these cases, the rotational velocity in the entire disk is significantly underestimated, particularly in the central region $r \lesssim 2L$. The difference between the curves of the first and second types virtually vanishes and the underestimation of the rotational velocity is largest for the rotation curve $V_{\varphi 3}$. Only at the very edge of the disk does the approximate equality $V_s \simeq V_\varphi$ holds. Since the velocity curves $V_s(x)$ depend only slightly on the actual shape of the rotation curve $V_\varphi(r)$, they do not allow the mass distribution in the galaxy to be reconstructed.

For any of the adopted dependences $V_\varphi(r)$, the velocity $V_s(x)$ rapidly increases with decreasing radial brightness scale length L in the spectral line, approaching $V_\varphi(r)$ (Figs. 3a and 3b). However, in general, the shape of the curve $V_s(x)$ weakly depends on L for any type of rotation curve.

The emission-gas distribution often appreciably deviates from an exponential one, particularly in the central region. In many spiral galaxies, gas forms a wide ring: the density exponentially decreases only at large r, while the central region exhibits a deficit of gas (Van den Bosch *et al.* 2000):

$$S(r) \propto r^\beta \exp\left(-r/L_{\rm gas}\right), \qquad (3)$$

where the values of β lie within a wide range, $\beta =$ 0.2–8 (Van den Bosch 2000).

The model with a gas ring at the radius of $r = L_{\rm gas}$ for $\beta = 1$ yields the observed rotation curve $V_s(x)$ shown in Figs. 3a and 3b (line *4*). The brightness decline in the central part of the galaxy causes an even more significant decrease in the measured $V_s(x)$. This effect is enhanced with increasing β. As a result, we can obtain a nearly linear dependence of the line-of-sight velocity for most of the disk.

2.2. Models with Absorption

When light passes through the disk matter, the contribution from the farther regions of the galaxy is smaller than the contribution from its regions located closer to the observer. As an illustration, Fig. 4 shows the lines of equal optical depth τ. Dust-containing galaxies are virtually opaque to the light that propagates in the disk at a small angle to its plane. Therefore, we can assume that the light from the farthest region does not reach the observer. The light from the middle region, where the line-of-sight rotational velocity is at a maximum, is significantly attenuated; the closer the center of the system, the stronger the absorption effect. As a result, in the central region of the galaxy ($r \lesssim R/2$), the nearest region, in which the line-of-sight velocity is low, mainly contributes to

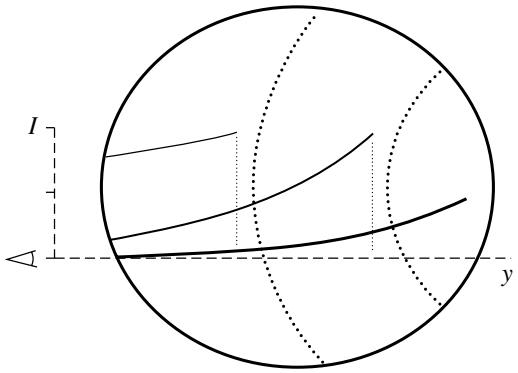

Fig. 4. A scheme that shows the effect of internal absorption in the galaxy on the measured rotational velocity. The dotted lines represent $\tau \approx 1$, and the solid lines represent the growth of τ along the line of sight.

the light. When corrected for absorption, relation (1) takes the form

$$V_s(x) = \frac{\int\limits_{-y_0}^{y_0} S(r)\exp(-\tau(x,y))V_\varphi(r)\dfrac{x}{\sqrt{x^2+y^2}}dy}{\int\limits_{-y_0}^{y_0} S(r)\exp(-\tau(x,y))dy}, \quad (4)$$

where the quantity $\tau(x,y)$, which characterizes the optical depth per unit length in the disk plane, is determined by the dust distribution function $f_{\rm dust}(x,y)$:

$$\tau = \int\limits_{y_0}^{y} f_{\rm dust}\,(x,\xi)\,d\xi. \quad (5)$$

For simplicity, we restrict our analysis to an axisymmetric exponential dust distribution:

$$f_{\rm dust}(x,y) = \alpha_{\rm d}\exp\left(-\frac{\sqrt{x^2+\xi^2}}{L_{\rm d}}\right), \quad (6)$$

where $L_{\rm d}$ is the radial scale length of the distribution of the absorbing medium and $\alpha_{\rm d}$ is the normalization parameter. Following the gas-density distribution, the function $\tau(x)$ decreases with galactocentric distance and becomes zero at $r = R$. Let us define the parameter $\tau_0(x)$ as the optical depth per unit length (1 kpc) on the major axis of the galaxy at the galactocentric distance $r = x$. Being proportional to $f_{\rm dust}$, this quantity reflects the density of the absorbing medium at a given galactocentric distance x. When we constructed the model dependences of the line-of-sight velocity along the galactic disk, we varied the parameter $\alpha_{\rm d}$ between 0 and 6, which corresponds to a variation of the optical depth τ_0 between 0 and 2.2 kpc^{-1} at a galactocentric distance $x = 3$ kpc.[1]

[1]The opacity in units of τ kpc^{-1} roughly corresponds to the attenuation in magnitudes per 1 kpc.

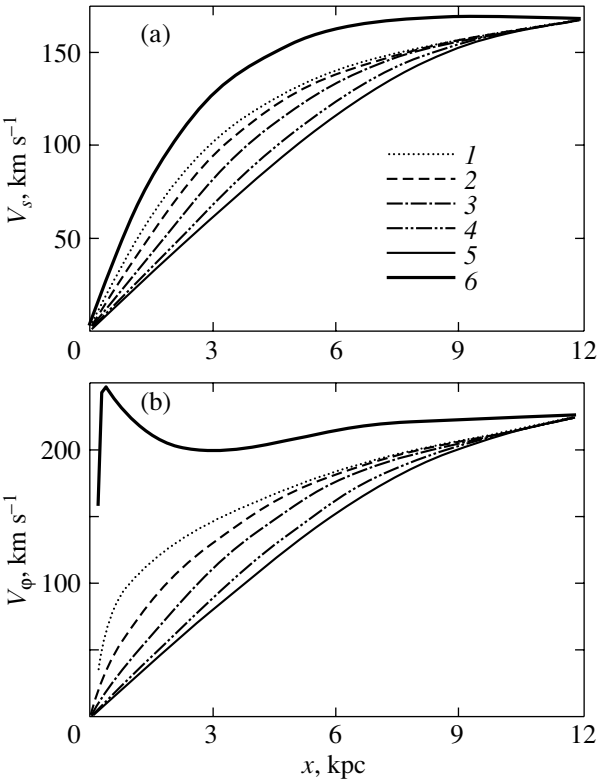

Fig. 5. The absorption-corrected line-of-sight velocity distributions $V_s(x)$ for the radial scale length of the dust distribution $L = L_{\rm d} = 3$ kpc. (a) The dependences $V_\varphi(r)$ (a bulgeless model) and $V_s(x)$ for various optical depths at $r = 3$ kpc: (*1*) $\tau_0 = 0$, (*2*) 0.37, (*3*) 0.73, (*4*) 1.46, and (*5*) 2.2 kpc^{-1}. (b) The same for the rotation curve of the third type (see Fig. 2b).

Figure 5 shows the results of our calculations using formula (4) with an allowance made for relations (2), (5), and (6) for the radial scale lengths of the distributions of the emission-line brightness and the dust density equal to $L = 3$ kpc and $L_{\rm d} = 3$ kpc, respectively, at various values of τ_0. In all cases, the absorption greatly decreases the velocity $V_s(x)$, except for the outer, relatively transparent part of the galaxy. As a result, the observed rotation curve straightens out. Therefore, in a very dusty disk, a nearly linear increase in $V_s(x)$ can be traced to the outer disk boundary, irrespective of the actual shape of the rotation curve (see Fig. 5). The presence of a ring and a central hole (see formula (3)) in the gas distribution enhances this feature in the behavior of the curve $V_s(x)$ even further in models with absorption.

3. EFFECTS OF RANDOM MOTIONS

3.1. The Model

In the models considered above, we assumed that the velocity dispersion of the radiation sources was

equal to zero and that there was only regular rotation. Let us now take into account the residual velocities, which we will characterize by the dispersions of the radial (c_r) and azimuthal (c_φ) velocities. If the rotation curve is estimated from stellar spectra, then we can assume, in accordance with observations (see, e.g., Bottema 1993), that both c_r and c_φ decrease with increasing galactocentric distance. For c_r, we adopt the simple expression

$$c_r = c_{r0}\exp(-r/L_c). \quad (7)$$

As a rule, the radial scale length L_c of the velocity dispersion is several times larger than the density scale length L. We choose a velocity distribution function in the form

$$F = F_0\exp\left\{-\frac{(V_\varphi - v_\varphi)^2}{2c_\varphi^2} - \frac{v_r^2}{2c_r^2}\right\}, \quad (8)$$

where c_r and c_φ are the velocity dispersions for the random velocity components v_r and v_φ, respectively. The line profile, which reflects the velocity variation along the line of sight, at a fixed observed distance from the center of the galactic disk is given by the expression

$$I(v_y, x) = I_0\int\limits_{-y_0}^{y_0} S(x,y)\exp(-\tau)F(x,y,v_y)dy, \quad (9)$$

where I_0 is the normalization constant and τ is determined by integral (5).

3.2. The Observed Rotation Curves for Gaseous and Stellar Disks

Let us consider separately the effects of the factors described above on the observed rotation curves of the dynamically hot (stellar disk) and cold (gaseous disk) subsystems for edge-on galaxies. For the gaseous disk, $c_r/V_{\max} \ll 1$ (where $V_{\max}$ is the maximum rotational velocity) and the velocity distribution is isotropic ($c_r = c_\varphi$). Figure 6 shows the velocity profiles (Doppler line profiles) $I(V) = I(v_y, x)$ at various distances from the disk center. In the absence of dust (Fig. 6a), the profiles differ greatly for different distances x. A characteristic feature of the profiles is their asymmetry and, for the central region (Fig. 6a, curves *1*–*3*), the presence of two peaks or a long wing with a "step" in place of the second peak (curves *4*–*7*). The first peak (at high velocities) is attributable to the rapid rotation of matter in the region $|\varphi| \ll 1$ near the "major axis" (see Fig. 2a). The second peak or the step (at lower velocities) is associated with two factors: the presence of residual velocities, and, to a greater extent, the large decrease in the line-of-sight velocity component V_φ at $|\varphi| > \pi/4$.

The situation qualitatively changes in a very dusty disk (Fig. 6b). All $I(V)$ profiles in the central region exhibit only one peak (of the two peaks observed in the previous case, only the peak that corresponds to the lower velocity remains). The peak at the higher velocity emerges only when the absorption is low enough to make it possible to observe the regions near the major axis at a given distance x.

The velocity dispersion for the stellar disk is higher than that for the gas. For an axisymmetric model, $c_\varphi = \frac{\varkappa}{2\Omega}c_r$, where the epicyclic frequency $\varkappa$ and the angular velocity Ω can be calculated from the dependence $V_\varphi(r)$. Figures 6c and 6d show the distributions $I(V)$ for a stellar disk with a central stellar radial velocity dispersion $c_r(0)/V_{\max} = 0.5$ (where $I(V)$ is taken in absolute value, because we deal with absorption lines). In this case, as in the case of emission gas, the $I(V)$ peaks shift toward lower velocities in the presence of absorption.

The complex shape of the line profiles results in a difference between the line-of-sight velocities estimated from the measurement of the wavelengths that correspond to the intensity peak and the wavelengths of the line "barycenter." Figure 7 shows the dependences $V_\varphi(r)$ and $V_s(x)$ constructed from the positions of the peaks in the $I(V)$ profiles shown in Figs. 6a–6d. According to what was said above, in the presence of two peaks, we chose the peak at the higher velocity. In the model of an absorption-free gaseous disk (Fig. 6a), this method of estimating the velocity yields a small difference between the actual rotational velocity V_φ and $V_s(x)$ (curves *1* and *2* in Fig. 7). In our case, it does not exceed 7% (see Fig. 7).

The difference $V_\varphi - V_s(x)$ is much higher for a stellar population with a large velocity dispersion, $c_r(0)/V_{\max} = 0.5$. However, in this case, the internal peak is also clearly traceable in the rotation curve (curve *3*), although its amplitude is appreciably smaller.

Thus, the approach based on the determination of the $I(V)$ peak yields a more accurate result when constructing the rotation curve than does the method of the weighted mean line-of-sight velocity determined from the line "barycenter" (see Section 2). Unfortunately, changing the shape of the line profile with an accuracy sufficient for a detailed comparison with the model profiles presented here requires a spectral resolution that is difficult to achieve. Besides, the line profiles in real galaxies are usually distorted by the nonuniform distribution of the emission regions and absorbing medium. However, the asymmetry of the profile, if present, can be measured and taken into account when estimating the velocity.

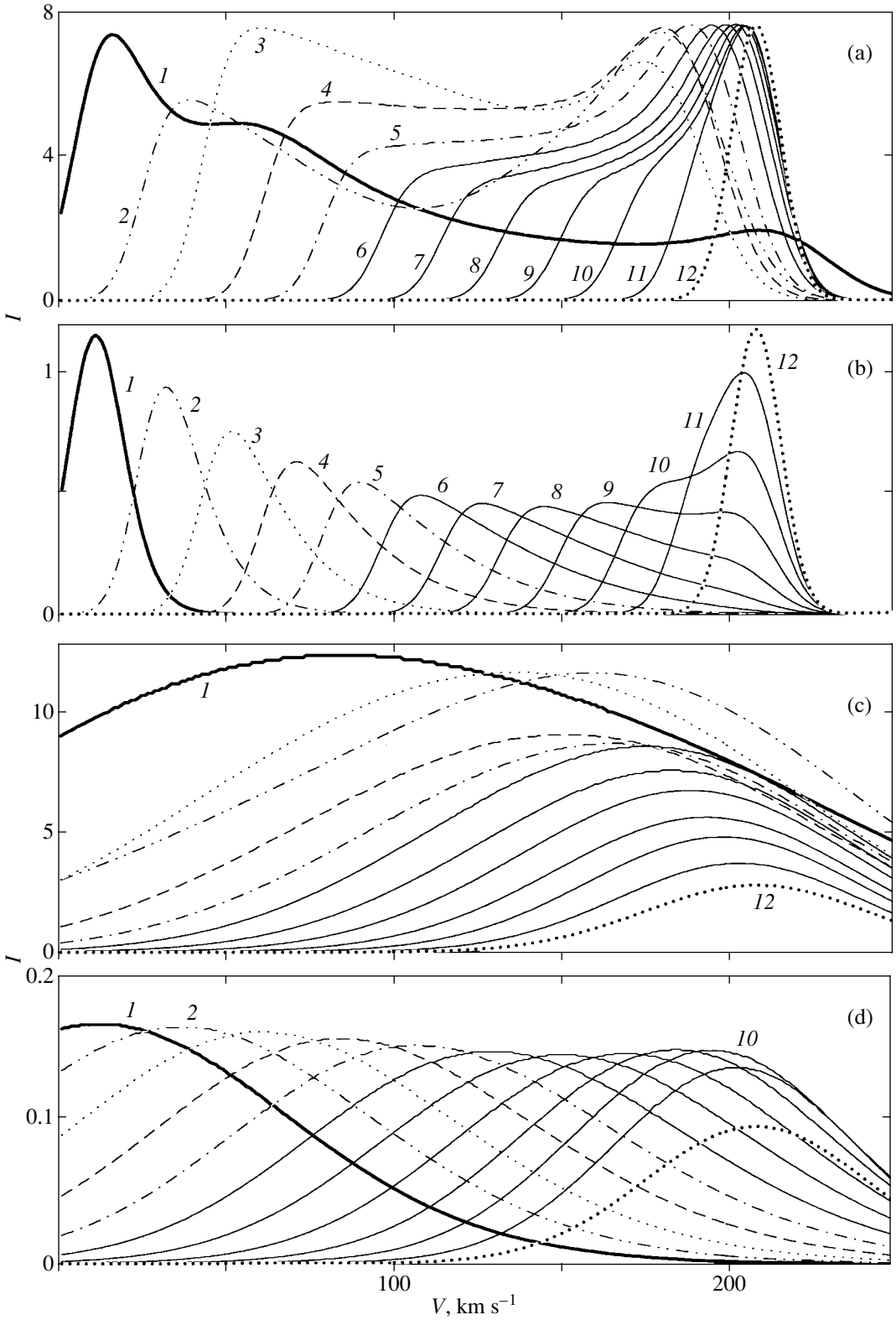

Fig. 6. (a) The line profiles $I(V)$ at various galactocentric distances for a model gaseous disk with a velocity dispersion $c_r(0) = 15$ km s^{-1} and radial scale length $L_c = 9$ kpc (without an allowance for absorption). The functions $I(V)$ are normalized arbitrarily. The disk is broken down into 12 zones; the numbers indicate the zone numbers in order of increasing distance from the disk center. (b) The same for the model of a very dusty disk with $\tau_0 = 2.2$ kpc^{-1}. (c) The same for the model of an absorption-free stellar disk with $c_r(0) = 100$ km s^{-1} and $L_c = 3$ kpc. (d) The same for the model of a very dusty disk with $\tau_0 = 2.2$ kpc^{-1}.

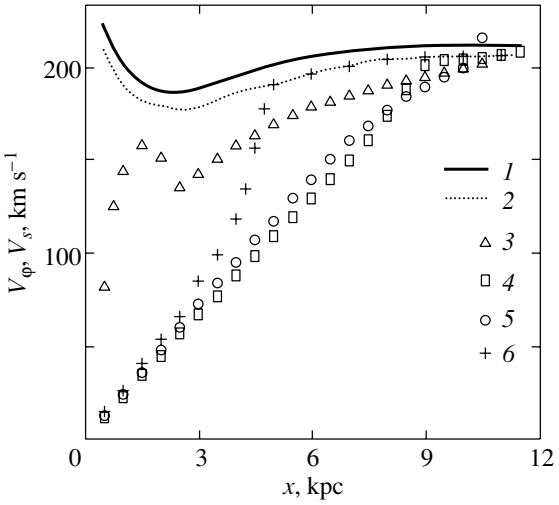

Fig. 7. The specified galactic rotation curve ($V_\varphi(r)$, curve *1*) in comparison with the measured rotation velocities $V_s(x)$ constructed from the maxima of the function $I(V)$ (see the text) for the following models: (*2*) an absorption-free gaseous disk; (*3*) an absorption-free stellar disk; (*4*) a gaseous disk with strong absorption ($\tau_0 = 2.2$ kpc^{-1}); (*5*) a stellar disk with strong absorption ($\tau_0 = 2.2$ kpc^{-1}), and (*6*) a gaseous disk with weak absorption ($\tau_0 = 0.73$ kpc^{-1}). In all cases, the radial scale length of the gas and dust distribution was assumed to be 3 kpc, and τ_0 refers to 3 kpc.

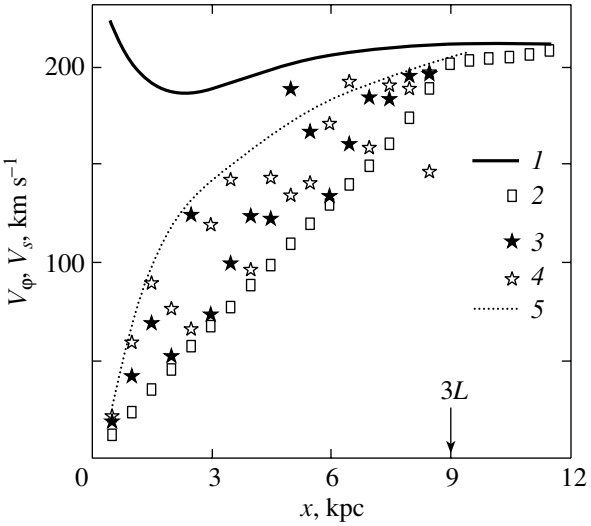

Fig. 8. The radial profile of the actual rotational velocity for a model galaxy (V_φ, curve *1*) and the measured velocities for an edge-on galaxy (the same as Fig. 7) for the following models: (*2*) a gaseous disk with strong absorption and a smooth dust distribution; (*3* and *4*) a disk with the same parameters and a random distribution of absorbing regions (the filled and open symbols refer to the two halves of the disk), and (*5*) a fitting curve.

In a very dusty disk, the dependences $V_s(x)$ derived by the two methods differ little for the gaseous and stellar populations (curves *4* and *5* in Fig. 7). In both cases, the inferred rotation curve $V_s(x)$ does not give a correct idea of the shape of the actual rotation curve in the inner disk.

Of greatest interest is the intermediate case where the absorption is strong in the central region of the galaxy (the line profile exhibits only one peak, at low velocities), and, starting from some value of x, the regions near the major axis that are responsible for the high-velocity peak significantly contribute to the observed radiation. In this case, the rotation curve constructed from the positions of the peaks in the line profiles exhibits a sharp "jump" from velocities much lower that the rotational velocity to velocities close to the latter (curve *6* in Fig. 7). The weaker the absorption in the galaxy, the closer to the center this transition occurs. By varying τ_0 in the models under consideration, we found that the rise in the measured rotational velocity occurs at a radius r at which the absorption drops below $0.3{-}0.5^m$ per 1 kpc. Such a step in the rotation curve is actually observed in several edge-on galaxies (see the example in Fig. 1b).

The calculations described in Subsections 3.2 and 3.3 refer to the rotation curve $V_{\varphi,3}$ (see Fig. 2b). The main conclusions remain valid for the cases $V_{\varphi,2}$ and $V_{\varphi,1}$.

3.3. Models with a Nonuniform Dust Distribution

As observations indicate, the dust distribution in the disks of galaxies is highly asymmetric and nonunofirm on small scales ($\ll L$). As an illustration, let us consider a model in which the absorbing regions are distributed by "spots" randomly scattered over the disk. We will characterize the concentration of dust in the ith cloud ($i = 1, ..., m$) with central coordinates $(x_\mathrm{d}^{(i)}, y_\mathrm{d}^{(i)})$ by the quantity $\tau^{(i)}$, which obeys law (6). In this model, the cloud sizes $l_\mathrm{d}^{(i)}$ were specified randomly from the interval $0.1L \le l_\mathrm{d}^{(i)} \le 0.5L$.

Figure 8 shows the radial dependence of the velocity $V_s(x)$ in the model with $m = 50$ and $\tau_0 = 2.2$ (symbols *3* and *4*). Clearly, the scatter of points or the irregular shape of the curve $V_s(x)$, which is asymmetric relative to the center of the galaxy, result from the existence of randomly located transparency corridors, which allow the regions located deep in the disk to be observed in some directions. The amplitude of the velocity variations can be significant, and, as was suggested by Goad and Roberts (1981), to obtain the rotation curve, we must draw the upper envelope of the points in the $V_s(x)$ diagram. However, even in this case, the shape of the rotation curve can be traced only approximately. If the mean dust density is sufficiently low, so that we observe the regions located near the major axis at different distances x, the above procedure actually makes it possible to obtain the

rotation curve. However, this is most likely true for the outer regions of the galaxy where τ_0 is small. For the model under consideration, even the envelope of the data points in the $V_s - r$ diagram (the dotted line in Fig. 8) is far from the specified shape of the rotation curve.

It would be natural to expect another effect produced by a nonuniform dust distribution for galaxies with a well-developed spiral structure. A certain orientation of the spiral arms toward which the interstellar medium concentrates leads to different disk transparencies on different sides of the center. Where the spiral arm is located on the side of the galaxy facing the observer, the line of sight penetrates the disk to a smaller depth, which decreases the rotation velocity estimate. As a result, the measured curves $V_s(x)$ are asymmetric relative to the center. Such cases are actually observed (see Fig. 1c). The curve drawn through higher measured velocities should be considered to be closer to the actual shape of the rotation curve.

At large x, all of the observed rotation curves ($V_s(x)$) in the models considered in this and previous sections flatten out , which corresponds to the specified rotational velocity of the model galaxy. Therefore, the measured maximum rotation velocities of edge-on disks must differ little from the actual values.

4. DISCUSSION AND CONCLUSIONS

Simple axisymmetric disk models for edge-on galaxies clearly show that the effects of geometrical projection, internal absorption, and velocity dispersion are the factors that can irreparably distort the observed shape of the rotation curve, particularly in the inner galaxy, making it similar to the shape imitating rigid rotation. For this reason, the rotation curves with a large velocity gradient in the central region undergo the greatest distortion, while the rotation curves of low-mass galaxies, which usually monotonically rise to the optical disk boundaries, undergo the smallest distortion. That is why in many cases, the observed rotation curves of edge-on galaxies rise almost linearly out to the peripheral disk regions.

The errors in the measured velocities of the stellar disk (as estimated from absorption lines) increase appreciably due to the higher (than for the gas) velocity dispersion of the disk stars. For the central region of the galaxy, the error in the estimated velocity can be 20–50% even in the absence of absorption.

The projection effect, as well as the absorption effect, tends to straighten out the observed rotation curve. However, its role can be significantly reduced if the velocity at a given galactocentric distance is measured from the position of the high-velocity peak (or the high-velocity cutoff) in the line profile rather than from its centroid. In this case, in the absence of absorption, the actual shape of the rotation curve of the galaxy can be accurately reproduced from observations even for the inner disk. This method of measurement may be applied to lenticular galaxies with a low dust content and to galaxies whose rotation curves are constructed from radio observations.[2]

Unfortunately, the low intensity of the emission and the nonuniform distribution of the emission regions and absorbing medium make it difficult to measure the shapes of the optical line profiles for actual edge-on galaxies with spectral and spatial resolutions that would allow detailed comparisons with model profiles. However, the asymmetry or the double-peaked line profiles for regions with moderate absorption that follows from the models can be found and taken into account when analyzing the observed rotation curve (see Subsection 3.2).

Strong internal absorption in the disk qualitatively changes the situation. As the models show, the two methods of measuring the velocity (from the position of the line peak and centroid) yield a monotonically (almost linearly) rising $V_s(x)$ curve up to galactocentric distances of several radial brightness scale lengths L. The double-peaked pattern of the line profiles disappears. This effect is only enhanced if there is a shortage of gas in the central region of the galaxy. The actual shape of the rotation curve in the opaque disk region can no longer be reconstructed from observations without using additional data. The transition from underestimated to actual rotation velocities occurs at a galactocentric distance where the absorption is equal to several tenths of a magnitude per 1 kpc. In this case, the observed rotation curve can exhibit a step, which is actually observed in some galaxies (see Subsection 3.2).

Curiously, contrary to the expectations, the line-of-sight velocity curves $V_s(x)$ for some edge-on galaxies exhibit no rigid rotation. In these galaxies, the central region is characterized by a high line-of-sight velocity gradient (Fig. 1c). Such a behavior implies either a very low dust content in the galaxy or (more likely) a significant deviation of the disk inclination from $i = 90°$. A deviation of several degrees can be enough for the effects of projection and internal absorption to become negligible (the accurate estimate of this angle depends on the disk thickness and the spatial distribution of the radiation sources and absorbing medium). The projection effect depends not only on the disk inclination i but also

[2] This approach is similar to the method for constructing the rotation curve by drawing the envelope in the position–velocity diagram based on radio observations (the envelope-tracing method) (Sofue 1996).

on the spectrograph slit width. Thus, if the slit is along the major axis of the galaxy and if its width is comparable to the apparent disk thickness (more precisely, to the size of the minor axis of the ellipse that bounds the disk region being measured), then the disk will be perceived as seen edge-on even if its inclination differs from 90°.

To summarize, note that although the shapes of the rotation curves of edge-on galaxies are generally of little use in estimating the masses of the individual components (particularly for galaxies with steep central gradients in the rotation velocity), their analysis can yield a correct estimate of the rotation velocities for the outer-disk regions and, consequently, a rough estimate of the total mass within a sufficiently large radius. In some cases, analysis of the observed rotation curve can provide information about the distribution of the absorbing medium in the galaxy.

ACKNOWLEDGMENTS

We are grateful to D. I. Makarov for useful discussions and help in choosing the illustrations of the galactic rotation curves. This work was supported by the Russian Foundation for Basic Research (project no. 01-02-17597) and, in part, by the Federal Science and Technology Program "Research and Development in Priority Fields of Science and Technology" (contract no. 40.022.1.1.1101).

REFERENCES

1. M. Baes and H. Dejonghe, Mon. Not. R. Astron. Soc. **335**, 441 (2002).
2. R. Bottema, Astron. Astrophys. **275**, 16 (1993).
3. F. C. van den Bosch, B. E. Robertson, and J. J. Dalcanton, Astron. J. **119**, 1579 (2000).
4. A. Bosma, K. C. Freeman, and E. Athamassoula, Astrophys. J. **400**, L21 (1992).
5. J. W. Goad and M. S. Roberts, Astrophys. J. **250**, 79 (1981).
6. R. Giovanelli and M. P. Haynes, Astrophys. J. **571**, L107 (2002).
7. I. D. Karachentsev and Zhou Xu, Pis'ma Astron. Zh. **17**, 321 (1991) [Sov. Astron. Lett. **17**, 135 (1991)].
8. I. D. Karachentsev, V. E. Karachentseva, and S. L. Parnovsky, Astron. Nachr. **313**, 97 (1993).
9. D. I. Makarov, A. N. Burenkov, and N. V. Tyurina, Pis'ma Astron. Zh. **25**, 813 (1999) [Astron. Lett. **25**, 706 (1999)].
10. D. I. Makarov, I. D. Karachentsev, and A. N. Burenkov, astro-ph/0006158 (2000).
11. D. I. Makarov, I. D. Karachentsev, A. N. Burenkov, *et al.*, Pis'ma Astron. Zh. **23**, 734 (1997a) [Astron. Lett. **23**, 638 (1997a)].
12. D. I. Makarov, I. D. Karachentsev, N. V. Tyurina, and S. S. Kaisin, Pis'ma Astron. Zh. **23**, 509 (1997b) [Astron. Lett. **23**, 445 (1997b)].
13. Y. Sofue, Astrophys. J. **458**, 120 (1996).

Translated by A. Dambis

Astronomy Letters, Vol. 29, No. 7, 2003, pp. 447–462. Translated from Pis'ma v Astronomicheskiĭ Zhurnal, Vol. 29, No. 7, 2003, pp. 508–525.

A Unified Theory of the Formation of Galactic Bars

V. L. Polyachenko and E. V. Polyachenko*

Institute of Astronomy, Russian Academy of Sciences, Pyatnitskaya ul. 48, Moscow, 109017 Russia

Received January 21, 2003

Abstract—We give arguments for a basically unified formation mechanism of slow (Lynden-Bell) and fast (common) galactic bars. This mechanism is based on an instability that is akin to the well-known instability of radial orbits and is produced by the mutual attraction and alignment of precessing stellar orbits (so far, only the formation of slow bars has been explained in this way). We present a general theory of the low-frequency modes in a disk that consists of orbits precessing at different angular velocities. The problem of determining these modes is reduced to integral equations of moderately complex structure. The characteristic pattern angular velocities Ω_p of the low-frequency modes are of the order of the mean orbital precession angular velocity $\bar{\Omega}_\mathrm{pr}$. Bar modes are also among the low-frequency modes; while $\Omega_\mathrm{p} \approx \bar{\Omega}_\mathrm{pr}$ for slow bars, Ω_p for fast bars can appreciably exceed even the maximum orbital precession angular velocity in the disk $\Omega_\mathrm{pr}^\mathrm{max}$ (however, it remains of the order of these precession angular velocities). The possibility of such an excess of Ω_p over $\Omega_\mathrm{pr}^\mathrm{max}$ is associated with the effect of "repelling" orbits. The latter tend to move in a direction opposite to the direction in which they are pushed. We analyze the pattern of orbital precession in potentials typical of galactic disks. We note that the maximum radius of an "attracting" circular orbit r_c can serve as a reasonable estimate of the bar length l_b. Such an estimate is in good agreement with the available results of N-body simulations. © *2003 MAIK "Nauka/Interperiodica".*

Key words: *galaxies, groups and clusters of galaxies, intergalactic gas.*

1. INTRODUCTION

Presently, all galactic bars are separated into two types: common, fast and Lynden-Bell, slow bars (see, e.g., Sellwood and Wilkinson 1993; Polyachenko 1994). This separation is made along several lines. On the one hand, it is believed that different bar angular velocities can manifest themselves in the fact that the former (common) bars end near corotation (or the $4:1$ resonance), while the latter (Lynden-Bell) bars end not far from the inner Lindblad resonance. Different bar names, fast and slow, correspond to this formal difference. On the other hand, distinctly different formation mechanisms are ascribed to these two types of bars. Whereas the physical mechanism is absolutely transparent for slow, Lynden-Bell bars (the mutual attraction and coalescence of slowly precessing orbits), the situation for fast bars is so far uncertain and confused. Fast bars in galactic stellar disks have long been thought to be formed when the disks rapidly rotate, much as is the case with classical incompressible strongly flattened (and, hence, rapidly rotating) Maclaurin spheroids. However, as was first convincingly showed by Toomre (1981), galactic bar modes actually have little in common with incompressible "edge" modes. Therefore, a different formation mechanism must correspond to them. As this mechanism, Toomre (1981) suggested swing amplification, which is now an almost universally accepted mechanism that accounts for the origin of normal (SA) spirals. However, a simple extension of the Toomre mechanism to SB galaxies is hardly possible. In particular, the existence of the traveling spiral density waves with which the swing amplification is associated (it must occur outside the bar, near corotation) is difficult to suspect in these galaxies. The attempt to associate fast bar modes in specific model stellar disks with swing amplification that was made, for example, by Athanassoula and Sellwood (1986) appears rather artificial. It seems more natural to find a bar-formation mechanism (recall that we consider here fast bars) that would be directly related to the instability of the innermost region of the galactic disk.

The properties of the families of periodic orbits in rotating bar potentials found by Contopoulos (1975) and Contopoulos and Mertzanides (1977) are of fundamental importance for the theory of galactic bars. Among them, the so-called x_1 family of orbits elongated along the bar within the corotation circle plays a central role. It is assumed (quite reasonably) that the figures of the galactic bars are composed of these periodic and almost periodic orbits. We emphasize,

*E-mail: epolyach@inasan.rssi.ru

however, that the aforesaid applies only to the theory of already formed bars and, strictly speaking, has no direct bearing on the bar-formation mechanism itself. In particular, this is true for the linear stage of the bar-forming instabilities. Clearly, the orbits considered by Contopoulos are captured ones in the bar potential and the capture itself is, of course, a nonlinear process.

Nevertheless, it is common practice to draw some natural, at first glance, conclusions about the bar-formation mechanisms (including the possible instabilities at the linear stage) from the described picture of the bar-forming orbits. The angular velocity Ω_p of a fast bar is higher (occasionally much higher) than the maximum precession angular velocity Ω_{pr}^{max}. At the same time, our intuition tells us that the angular modulation of the distribution of precessing orbits (i.e., the figure of the bar formed by the Lynden-Bell mechanism) must rotate with a velocity of the order of the mean orbital precession angular velocity. This conclusion would imply that the Lynden-Bell mechanism is unsuitable for explaining the formation of fast bars. Therefore, it is generally believed that, actually, the growing bar causes the orbits to change their shape by adjusting to the bar that gains in strength and becomes increasingly thin. The fact that this effect can be significant even at the linear stage is justified in the theory of a weak bar (see, e.g., Sellwood and Wilkinson 1993). These authors showed in terms of the linear theory that initially circular orbits in the bar potential transform into slightly flattened or elongated ovals oriented relative to the bar in the same way as the general orbits of the x_1 family.

However, the following two objections can be raised with regard to what has been said in the last paragraph.

(1) Circular orbits cannot be typical representatives of the orbits of an unperturbed disk (except for the model of a cold disk that is of little interest in our case) until the bar-perturbed velocities exceed the velocity dispersion in the initially axisymmetric disk. Clearly, this is primarily true for the initial growth stage of the instability (from a sufficiently low level).

(2) The conclusion suggested by our intuition that the angular velocity Ω_p of the density wave in a system of precessing orbits cannot be higher than the maximum precession angular velocity Ω_{pr}^{max} is supported by the practice of similar calculations of unstable modes in numerous models of galactic disks. These calculations indicate that, in all cases, the wave angular velocity Ω_p is lower than the maximum angular velocity Ω_{max} of the disk stars.[1] However, the analogy is incomplete because of the possible "donkey" behavior of stellar orbits that was discovered by Lynden-Bell and Kalnajs (1972): the orbit accelerates when it is pulled back and decelerates when it is pushed forward. This behavior takes place when the following condition derived by Lynden-Bell (1979) is satisfied: $(\partial\Omega_{pr}/\partial L)|_{J_f} < 0$, where L is the angular momentum of the star, $J_f = J_r + L/2$ is the Lynden-Bell adiabatic invariant, and J_r is the radial action. As we show below, if stellar orbits with donkey behavior are involved in the bar-forming instability, then the bar angular velocity can be higher than Ω_{pr}^{max}.

The latter remark opens up the possibility of constructing a theory of fast bar modes as the corresponding density waves of precessing orbits, i.e., quite similar to the theory of Lynden-Bell bars. Note that Kalnajs (1973) was the first to give attention to the possible alignment of freely precessing orbits (and the formation of a bar in this way) in his theory of kinematic waves. Of great importance for Kalnajs' theory, who considered nearly circular orbits, was the fact that the precession angular velocity $\Omega_{pr}(r) = \Omega(r) - \kappa(r)/2$ (where $\Omega(r)$ is the disk angular velocity, $\kappa(r)$ is the epicyclic frequency, and $\kappa^2 = 4\Omega^2 + rd\Omega^2/dr$) was independent of the radius. Note, incidentally, that Lynden-Bell (1979) also required the same condition of approximate constancy for $\Omega_{pr}(r)$ in his more general treatment of the problem.

Actually, different stars in a galaxy precess with different angular velocities. However, it is important that the precession angular velocities (as in most cases the bar angular velocities Ω_p) are much lower than the characteristic azimuthal frequencies Ω_2 of the disk stars, let alone the radial frequencies Ω_1. If the inequality

$$|\Omega_p - \Omega_{pr}|/\Omega_1 \ll 1 \qquad (1)$$

is valid for some orbit, then this orbit as a whole (rather than individual stars in it) will act as an elementary object during the interaction with the gravitational field of the bar. If condition (1) is satisfied for most of the disk orbits involved in the bar formation, then we consider the processes (e.g., bar instabilities) in a model disk that consists of a system of precessing orbits. As Lynden-Bell (1979) noted, condition (1) implies that the adiabatic invariant $J_f = J_r + L/2$ is conserved. In fact, this conservation makes the problem of the bar instability one-dimensional: it will suffice only to trace the change in the angular positions of the orbital semimajor axes under the gravitational attraction from the bar.

We will solve the problem of the bar density wave of orbits precessing at different angular velocities, which

[1] Note that there is, probably, no general proof of this property of the oscillation-frequency spectrum for a gravitating disk.

is quite similar to the standard statement of the problem of the density waves (in particular, barlike ones) of stars in differentially rotating disks. It appears that inequality (1) is not satisfied with a margin for all of the orbits involved in the bar mode, in particular, of course, for fast bars. Nevertheless, in the latter case, $|\Omega_\mathrm{p} - \Omega_\mathrm{pr}| \sim \Omega_\mathrm{pr} \sim \Omega_\mathrm{G}$, where $\Omega_\mathrm{G} \sim \sqrt{GM_d/a^3}$ is the characteristic gravitational (Jeans) frequency (G is the gravitational constant, M_d is the mass of the (active) disk, and a is its radius); at $\Omega_\mathrm{pr}/\Omega_1 \ll 1$, we then remain within the scope of approximation (1). However, even if the weaker inequality $\Omega_\mathrm{pr}/\Omega_1 < 1$ (e.g., by several times rather than by an order of magnitude) is satisfied for some of the orbits, our model will, probably, yield qualitatively correct results. In any case, this approach is better justified than, for example, the analysis of the spiral structure in the galaxy M 33 (Shu *et al.* 1971) using the formulas of the Lin–Shu theory. Strictly speaking, the latter is applicable only to tightly wound multiturn spirals (note that quite reasonable results are obtained even in this case!).

The material in this paper is presented in the following order.

In Section 2, we describe the model of precessing orbits in a general form and derive the basic equations of the theory that are suitable for analyzing the disk low-frequency modes concerned. These equations can be most easily derived from the general kinetic equation for a stellar disk by using the action–angle variables (I_1, I_2; w_1, w_2). The derivation involves introducing the slow angular variable $\bar{w}_2 = w_2 - w_1/2$ and averaging over the fast angular variable w_1 (actually, over the radial stellar oscillations). In simple cases, the problem directly reduces to analyzing moderately cumbersome dispersion relations. In more general cases, integral equations of various complexity are obtained. However, even in the most general situation, the integral equation obtained in the model of the disk of orbits does not compare in complexity with the very cumbersome integral equations of Kalnajs (1965) and Shu (1970) for the normal modes of the stellar disk. It should be remembered that, in contrast to the incomparably simpler problem of analyzing tightly wound spirals, using these integral equations to analyze the large-scale modes (primarily the bar modes) generally remains the only possibility (except, of course, the N-body methods). As we see, the actual simplification is achieved in analyzing the low-frequency modes. Note that, in this case, the description of gravitating systems is similar to the drift approximation in plasma physics (see, e.g., Chew *et al.* 1956) but for orbits of a much more general form. In our opinion, the most important advantage of our approach is that the simple physical mechanisms of the processes (instabilities) developing in the disk become absolutely transparent. At the same time, the possibility of elucidating these physical mechanisms when using the general Kalnajs–Shu integral equations or N-body simulations is lost almost completely.

In Section 3, we analyze the dispersion relation for a model disk composed of two types of orbits that differ by the precession angular velocities Ω^1_pr and Ω^2_pr ($\Omega^2_\mathrm{pr} > \Omega^1_\mathrm{pr}$) and, in general, by the signs of the Lynden-Bell derivative $(\partial\Omega_\mathrm{pr}/\partial L)|_{J_f} \equiv \Omega'_\mathrm{pr}$. For opposite signs of this quantity, the angular velocity of the unstable wave is shown to be $\mathrm{Re}\Omega_\mathrm{p} > \Omega^2_\mathrm{pr}$, i.e., higher than the maximum precession angular velocity of the orbits in the disk. We believe that this result is an important argument for a basically unified formation mechanism of slow and fast bars. At the end of Section 3, we also give other arguments for the possibility that $\Omega_p > \Omega^\mathrm{max}_\mathrm{pr}$.

In Section 4, we present the results of our calculations of the precession angular velocities Ω_pr and the quantity Ω'_pr, which is of greatest importance for the theory, for several typical potentials. In particular, we determine the regions where $\Omega'_\mathrm{pr} > 0$ or $\Omega'_\mathrm{pr} < 0$. We make the natural assumption that the bar is formed by "attracting" orbits with $\Omega'_\mathrm{pr} > 0$.[2] The bar length l_b must then be equal to the maximum radius of the apocenter r_max calculated from the sufficiently populated orbits from the region where $\Omega'_\mathrm{pr} > 0$. Therefore, in general, apart from the overall pattern of orbital precession (it is determined by the potential Φ_0), calculating l_b also requires specifying the equilibrium distribution function f_0. However, as a first approximation, we can probably assume that $l_\mathrm{b} \approx r_\mathrm{c}$, where r_c is the radius of the circular orbit in which $\Omega'_\mathrm{pr} = 0$ (these radii were calculated for all of the potentials that we considered); in circular orbits, $\Omega'_\mathrm{pr} > 0$ at $r < r_\mathrm{c}$ and $\Omega'_\mathrm{pr} < 0$ at $r > r_\mathrm{c}$. Clearly, the estimate $l_\mathrm{b} \approx r_\mathrm{c}$ must satisfactorily correspond to the true bar length l_b primarily for fast bars.

Note that our determination of the length of the forming bar has nothing in common with the standard determinations that relate this length to the position of one of the resonances: the corotation resonance (CR), the inner Lindblad resonance (ILR), or the 4 : 1 resonance. Clearly, depending on the disk potential and the stellar distribution function, our estimated bar

[2] Note that "repelling" orbits with $\Omega'_\mathrm{pr} < 0$ can also be involved in the formation of the entire bar mode, i.e., not only the central bar but also the spirals adjacent to it (as was pointed out above, this can even be of importance in explaining the phenomenon of a fast bar).

length can take on widely differing values (including values close to any of the above three resonances). Interestingly, this is, probably, also true for slow bars (slow in the sense that for them, $\Omega_p \approx \bar{\Omega}_{pr}$, where $\bar{\Omega}_{pr}$ is the mean precession angular velocity of the orbits involved in bar formation). Thus, we call into question the earlier view (see, e.g., Lynden-Bell 1979; Polyachenko and Polyachenko 1995) that slow bars must necessarily end near the ILR. Strictly speaking, our estimate of the bar length refers to the bars being formed by instability (rather than the already formed bars) at the initial linear stage. However, we doubt that, subsequently, the bar length can significantly change.

In Section 5, we briefly formulate the most important conclusions and discuss some of the immediate prospects for the work in this field.

2. BASIC EQUATIONS FOR STUDYING THE LOW-FREQUENCY MODES AND THEIR PRELIMINARY ANALYSIS

2.1. Derivation of the Basic Equations

To derive the basic equations of our theory, it is most convenient to use the description of the stellar disk using the action–angle variables $(\mathbf{I};\mathbf{w}) = (I_1, I_2; w_1, w_2)$ that properly takes into account the double periodicity of the stellar motion in an equilibrium axisymmetric potential. Note that $I_1 = J_r$ (J_r is the radial action) and $I_2 = L$ (L is the angular momentum). We proceed from the linearized kinetic equation in its standard form (see, e.g., Fridman and Polyachenko 1984)

$$\frac{\partial f_1}{\partial t} + \Omega_1\frac{\partial f_1}{\partial w_1} + \Omega_2\frac{\partial f_1}{\partial w_2} = \frac{\partial f_0}{\partial I_1}\frac{\partial \Phi_1}{\partial w_1} + \frac{\partial f_0}{\partial I_2}\frac{\partial \Phi_1}{\partial w_2}, \tag{2}$$

where $f_0(\mathbf{I})$ and $f_1(\mathbf{I},\mathbf{w},t)$ are the unperturbed and perturbed distribution functions, respectively; Φ_1 is the gravitational-potential perturbation; Ω_1 and Ω_2 are the radial and azimuthal stellar oscillation frequencies in the equilibrium potential $\Phi_0(r)$, respectively; and $\Omega_i = \partial E(\mathbf{I})/\partial I_i$ (E is the energy expressed in terms of $\mathbf{I}$, $i = 1, 2$). By substituting $\bar{w}_2 = w_2 - w_1/2$ and $\bar{w}_1 = w_1$, we reduce Eq. (2) to

$$\frac{\partial f}{\partial t} + im\Omega_{pr} f + \Omega_1\frac{\partial f}{\partial w_1} = \frac{\partial f_0}{\partial I_1}\frac{\partial \Phi}{\partial w_1} + im\Phi\left(\frac{\partial f_0}{\partial I_2} - \frac{1}{2}\frac{\partial f_0}{\partial I_1}\right), \tag{3}$$

where the perturbations are assumed to be proportional to $\exp(im\bar{w}_2)$:

$$\Phi_1 = \Phi\exp(im\bar{w}_2), \quad f_1 = f\exp(im\bar{w}_2),$$

m is the azimuthal number (integer and even) and $\Omega_{pr}(\mathbf{I}) = \Omega_2 - \Omega_1/2$ is the precession angular velocity of the orbit with the actions (I_1, I_2). If, in addition, we change from the actions (I_1, I_2) to (E, L) (the equilibrium distribution function is most often specified in the variables (E, L)), then the linearized kinetic equation takes the form

$$\frac{\partial F}{\partial t} + im\Omega_{pr}F + \Omega_1\frac{\partial F}{\partial w_1} = \Omega_1\frac{\partial F_0}{\partial E}\frac{\partial \Phi}{\partial w_1} + im\Phi\left(\frac{\partial F_0}{\partial L} + \Omega_{pr}\frac{\partial F_0}{\partial E}\right), \tag{4}$$

where $F_0(E, L) = f_0(I_1, I_2)$. Note that Eq. (4) in this form is also valid when the potential Φ_0 is an "almost Coulomb" one, i.e., is mainly determined by the large central mass. In this case, $\bar{w}_2$ and Ω_{pr} must only be defined differently: $\bar{w}_2 = w_2 - w_1$ and $\Omega_{pr} = \Omega_2 - \Omega_1$. Disregarding the self-gravitation of the system and the quadrupole moment of the central body, we then have $\Omega_{pr} = 0$, as it should be for closed Keplerian orbits. The azimuthal number m in this case can be even and odd.

As was noted by Lynden-Bell (1979) and explained in detail in Section 1, $J_f = I_1 + I_2/2$ and $L = I_2$ are the most appropriate variables that should be used in place of (I_1, I_2) or (E, L) to study the low-frequency modes.

It is easy to see that J_f and L are the actions that are canonically conjugate with the angular variables $\bar{w}_1$ and $\bar{w}_2$ introduced above. Indeed, by the formal change of variables $(I_1, I_2; w_1, w_2) \equiv (\mathbf{I},\mathbf{w}) \to (J_f, L; \bar{w}_1, \bar{w}_2) \equiv (\mathbf{J},\bar{\mathbf{w}})$, we make sure that the canonical Hamilton equations in the variables $(\mathbf{I},\mathbf{w})$

$$\dot{I}_1 = -\frac{\partial H}{\partial w_1}, \quad \dot{I}_2 = -\frac{\partial H}{\partial w_2}, \qquad \dot{w}_1 = \frac{\partial H}{\partial I_1}, \quad \dot{w}_2 = \frac{\partial H}{\partial I_2}, \tag{5}$$

where $H(I_1, I_2; w_1, w_2) = H_0(I_1, I_2) + \Phi_1(I_1, I_2; w_1, w_2)$ is the Hamiltonian, in the variables $(\mathbf{J},\bar{\mathbf{w}})$ also retain the canonical form

$$\dot{J}_f = -\frac{\partial \bar{H}}{\partial \bar{w}_1}, \quad \dot{I}_2 = -\frac{\partial \bar{H}}{\partial \bar{w}_2}, \qquad \dot{\bar{w}}_1 = \frac{\partial \bar{H}}{\partial J_f}, \quad \dot{\bar{w}}_2 = \frac{\partial \bar{H}}{\partial L}, \tag{6}$$

where $\bar{H}(J_f, L; \bar{w}_1, \bar{w}_2) = H(I_1, I_2; w_1, w_2)$.

In the unperturbed state when $\bar{H} = \bar{H}_0(J_f, L) = H(I_1, I_2)$, we have

$$\bar{w}_2^{(0)} = \Omega_{pr}t \quad (\Omega_{pr} = \Omega_2 - \Omega_1/2).$$

This equation clearly shows that the angular variable $\bar{w}_2$ is slow, because $|\Omega_{pr}| \ll |\Omega_2|, |\Omega_1|$. In this

situation, averaging over the fast variable, in our case, $\bar{w}_1$, is relevant to the study of the low-frequency modes with frequencies of the order of $\Omega_{\rm pr}$. The averaging procedure yields (see, e.g., Arnold *et al.* 2002)

$$\dot{J}_f \approx -\frac{1}{2\pi}\int\limits_0^{2\pi}\frac{\partial\bar{H}}{\partial\bar{w}_1}d\bar{w}_1 = 0, \qquad (7)$$

$$\dot{L} \approx -\frac{1}{2\pi}\int\limits_0^{2\pi}\frac{\partial\bar{H}}{\partial\bar{w}_2}d\bar{w}_1 = -\frac{\partial\bar{\Phi}}{\partial\bar{w}_2},$$

$$\dot{\bar{w}}_2 \approx \frac{1}{2\pi}\int\limits_0^{2\pi}\frac{\partial\bar{H}}{\partial L}d\bar{w}_1 = \Omega_{\rm pr}(J_f, L) + \frac{\partial\bar{\Phi}}{\partial L}.$$

The first of these equations implies the adiabatic invariance of J_f. Lynden-Bell (1979) introduced the quantity J_f based on the standard definition of the adiabatic invariant (Arnold *et al.* 2002):

$$J_f = \oint \mathbf{v}d\mathbf{r},$$

where the integral is taken over the complete radial stellar oscillation in a quadratic potential. We then have

$$J_f = \oint v_r dr + \frac{1}{2}\oint v_\varphi r d\varphi = \oint v_r dr + \frac{1}{2}\oint I_2 d\varphi = I_1 + \frac{1}{2}I_2,$$

where we took into account the fact that the star makes two complete radial oscillations in the time of its complete turn in azimuth.

Changing to the variables $(J_f, L; \bar{w}_1, \bar{w}_2)$ in Eq. (3), we obtain a kinetic equation in the form that is most convenient for subsequent use:

$$\frac{\partial\mathcal{F}}{\partial t} + im\Omega_{\rm pr}\mathcal{F} + \Omega_1\frac{\partial\mathcal{F}}{\partial w_1} = \frac{\partial\mathcal{F}_0}{\partial J_f}\frac{\partial\Phi}{\partial w_1} + im\Phi\frac{\partial\mathcal{F}_0}{\partial L}, \qquad (8)$$

where $\mathcal{F}_0(J_f, L) = f_0(I_1, I_2)$ and we took into account the fact that $\partial f_0/\partial I_2 - \frac{1}{2}\partial f_0/\partial I_1 = \partial\mathcal{F}_0/\partial L$.

Let us assume that the scatter of precession angular velocities about some mean value $\bar{\Omega}_{\rm pr}$, $\Delta\Omega_{\rm pr} = \overline{[(\Omega_{\rm pr} - \bar{\Omega}_{\rm pr})^2]}^{1/2}$, and the characteristic gravitational frequency $\omega_{\rm G}$ are small: $\bar{\Omega}_{\rm pr}$, $\omega_{\rm G} \ll \Omega_1$ (for the definition of $\omega_{\rm G}$, see Section 1). These inequalities are the easiest to justify by assuming that we consider a system of stars with almost the same (in reality, low compared to Ω_1) precession angular velocities inside a massive halo that is not involved in the perturbations but that gives a dominant contribution to the equilibrium potential Φ_0. It should be understood that the actual massive spherical component of the galaxy does not need to play the role of the halo, because, in general, different groups of orbits take a completely different part in the instability; as a first approximation, an active group of orbits can be commonly assumed to be inside a massive halo composed of other disk stars. A low-frequency mode ($\propto \exp(-i\bar{\omega}t)$) in the frame of reference that rotates with the angular velocity $\bar{\Omega}_{\rm pr}$, with $\bar{\omega} \equiv \omega - m\bar{\Omega}_{\rm pr} \sim \omega_{\rm G}$, $\Delta\Omega_{\rm pr}$, in which the slow precession-induced dispersion of the orbits is offset by their mutual gravitational attraction, can exist under the conditions written above. It would be natural to expect that when the self-gravitation dominates over the orbital precession velocity dispersion, an instability that leads to the deformation of the system (under the effect of the largest-scale growing modes) must develop. However, it is easy to understand that even for systems with nearly radial orbits, this is true only if the torque that changes the angular momentum of the stars in orbits also causes their precession angular velocity to change in the same direction (see Section 1 and the discussion in Subsection 2.2).

We find the sought-for solution for the low-frequency modes from the perturbation theory. We assume that $\mathcal{F} = \mathcal{F}^{(1)} + \mathcal{F}^{(2)}$, where $\mathcal{F}^{(1)}$ corresponds to the permutational mode that is obtained from Eq. (8) if the terms proportional to $\Delta\Omega_{\rm pr}$ and $\Phi \propto G$ are discarded: $\omega = 0$ (or $\omega = m\bar{\Omega}_{\rm pr}$ at $\bar{\Omega}_{\rm pr} \neq 0$)[3] and $\partial\mathcal{F}^{(1)}/\partial w_1 = 0$; i.e., $\mathcal{F}^{(1)} = \mathcal{F}^{(1)}(J_f, L)$ is a (so far) arbitrary function of the integrals of motion, which is subsequently specified by using the periodicity condition for the solution of the next approximation.

The equation for $\mathcal{F}^{(2)}$ is

$$-i\omega\mathcal{F}^{(1)} + im\Omega_{\rm pr}\mathcal{F}^{(1)} + \Omega_1\frac{\partial\mathcal{F}^{(2)}}{\partial w_1} = \frac{\partial\mathcal{F}_0}{\partial J_f}\frac{\partial\Phi}{\partial w_1} + im\Phi\frac{\partial\mathcal{F}_0}{\partial L}. \qquad (9)$$

Given the periodicity of the functions $\mathcal{F}^{(2)}$ and Φ, averaging (9) over w_1 in the interval $(0, 2\pi)$ yields

$$-(\bar{\omega} - m\delta\Omega_{\rm pr})\mathcal{F}^{(1)} \approx m\frac{\partial\mathcal{F}_0}{\partial L}\frac{1}{2\pi}\int\limits_0^{2\pi}\Phi dw_1, \qquad (10)$$

where $\delta\Omega_{\rm pr} = \Omega_{\rm pr} - \bar{\Omega}_{\rm pr}$.

Note that Eq. (10) can also be obtained from the Fourier expansions that were used by Lynden-Bell

[3] Note that, actually, it is only required that the inequality $|\omega - m\Omega_{\rm pr}| \sim |\Omega_{\rm p} - \Omega_{\rm pr}| \ll \Omega_1$ be satisfied; the frequency ω (or the wave angular velocity $\Omega_{\rm p} = \omega/m$) is not determined in the first approximation.

and Kalnajs (1972) in their study of the resonant interactions of spiral density waves with disk stars. Naturally, it is more convenient to proceed from the transformed system (6) rather than from system (5), used by Lynden-Bell and Kalnajs. The stellar orbits can be determined from the perturbation theory. The first-order orbits are sought by solving Eqs. (6) with the unperturbed orbits substituted into their right-hand sides (when calculating the forces). For the first-order correction $\Delta_1 J_i$ to J_i ($J_1 = J_f$, $J_2 = L$), we then obtain $\Delta_1 J_i = \partial\chi/\partial\bar{w}_i$, where at a fixed azimuthal number m,

$$\chi = \frac{1}{2\pi}\sum_l \psi_{lm}(\mathbf{J})\frac{\exp[i(l\bar{w}_1 + m\bar{w}_2 - \omega t)]}{i(l\Omega_1 + m\Omega_{\rm pr} - \omega)} \quad (11)$$

and $\psi_{lm}(\mathbf{J})$ are the Fourier expansion coefficients

$$\Phi_1(\mathbf{J}, \bar{\mathbf{w}}, t) \quad (12)$$
$$= \frac{1}{2\pi}\sum_l \psi_{lm}(\mathbf{J})\exp[i(l\bar{w}_1 + m\bar{w}_2 - \omega t)].$$

Since $\Omega_{\rm pr} \ll \Omega_1$, we can separate out the dominating term in (11) (with $l = 0$, when a small denominator appears under the assumption of $\omega = m\Omega_{\rm p} \sim \Omega_{\rm pr}$):

$$\chi = \frac{1}{2\pi}\psi_{0m}(\mathbf{J})\frac{\exp[i(m\bar{w}_2 - \omega t)]}{i(m\Omega_{\rm pr} - \omega)}. \quad (13)$$

As is clear from (12),

$$\frac{1}{2\pi}\psi_{0m}(\mathbf{J}) = \bar{\Phi}_1 \equiv \frac{1}{2\pi}\int_0^{2\pi}\Phi_1 d\bar{w}_1.$$

Consequently,

$$\Delta_1 J_f = \frac{\partial\chi}{\partial\bar{w}_1} = 0, \quad (14)$$
$$\Delta_1 L = \frac{\partial\chi}{\partial\bar{w}_2} = -\bar{\Phi}_1\frac{m}{\omega - m\Omega_{\rm pr}},$$

where the factor $\exp[i(m\bar{w}_2 - \omega t)]$ was omitted. Finally, we obtain the perturbation of the distribution function as

$$\mathcal{F}_1 = \mathcal{F}_0(J_f, L + \Delta L) - \mathcal{F}_0(J_f, L) \approx \Delta L\frac{\partial\mathcal{F}_0}{\partial L}$$
$$= -\frac{\partial\mathcal{F}_0}{\partial L}\bar{\Phi}_1\frac{m}{\omega - m\Omega_{\rm pr}},$$

which closely matches (10). Of course, the calculations could be reduced to a minimum if we immediately used the averaged equations (7).

Let us return to the derivation of the basic equations. Having relation (10) and using the Poisson equation, we obtain after simple transformations

$$\Phi = -G\int d\mathbf{J}'\mathcal{F}^{(1)}(\mathbf{J}') \quad (15)$$
$$\times \int d\bar{\mathbf{w}}'\Gamma(r, r', \varphi' - \varphi)\exp[im(\bar{w}_2' - \bar{w}_2)],$$

where $d\mathbf{J}' = dJ_f' dL'$; $d\bar{\mathbf{w}}' = d\bar{w}_1' d\bar{w}_2'$; and Γ is Green's function:

$$\Gamma = \frac{1}{r_{12}}, \quad r_{12} = [r^2 + r'^2 - 2rr'\cos(\varphi' - \varphi)]^{1/2}. \quad (16)$$

Relation (15) is an integral equation for function $\Phi(\mathbf{J}, w_1)$ when we take into account expression (10) for $\mathcal{F}^{(1)}$ in terms of Φ. The coordinates of the stars r, φ, r', and φ' in (15) and (16) must be expressed in terms of $\mathbf{J}$, $\mathbf{J}'$, $\bar{\mathbf{w}}$, and $\bar{\mathbf{w}}'$, with

$$r = r(\mathbf{J}, w_1), \quad r' = r'(\mathbf{J}', w_1'),$$
$$\bar{w}_2' - \bar{w}_2 = (w_2' - w_2) - (w_1' - w_1)/2,$$
$$\varphi' - \varphi \equiv \delta\varphi = w_2' - w_2 + \phi(\mathbf{J}, \mathbf{J}', w_1, w_1');$$

we are not writing out the expression for the function ϕ. Since the perturbed potential can always be written as

$$\Phi_1(r, \varphi) = \bar{\Phi}_1(r)\exp(im\varphi) = \Phi\exp(im\bar{w}_2),$$

we have

$$\Phi = \bar{\Phi}_1(r)\exp[im\delta(\mathbf{J}, w_1)].$$

($\delta = \varphi - \bar{w}_2$ is a known function of $\mathbf{J}$ and w_1); therefore, the integral equation (15) is actually the equation for the unknown function $\Phi_1(r)$ of only one variable. The same can also be said about the integral equations of Kalnajs and Shu mentioned in Section 1, though; however, our equation is incomparably simpler. Equation (15) is rather asymmetric but it can be simplified. The right-hand side of Eq. (15) depends on w_1 only via Γ and $\exp[im(\bar{w}_2' - \bar{w}_2)]$. Therefore, averaging (15) over w_1, for the function

$$\chi(\mathbf{J}) = \bar{\Phi} = \frac{1}{2\pi}\int_0^{2\pi}\Phi dw_1,$$

we obtain the integral equation

$$\chi(\mathbf{J}) = \frac{Gm}{2\pi}\int d\mathbf{J}'\Pi(\mathbf{J}, \mathbf{J}')\frac{\partial\mathcal{F}_0(\mathbf{J}')/\partial L'}{\omega - m\delta\Omega_{\rm pr}(\mathbf{J}')}\chi(\mathbf{J}'), \quad (17)$$

where

$$\Pi(\mathbf{J}, \mathbf{J}') = \int dw_1 dw_1' d\delta w_2\Gamma(r, r', \delta\varphi) \quad (18)$$
$$\times \exp(im\delta w_2)\exp[-im(w_1' - w_1)/2]$$
$$= \int dw_1 dw_1' d\delta\bar{w}_2\Gamma(r, r', \delta\varphi)\exp(im\delta\bar{w}_2),$$
$$\delta w_2 \equiv w_2' - w_2, \quad \delta\bar{w}_2 \equiv \bar{w}_2' - \bar{w}_2. \quad (19)$$

The physical meaning of $\Pi(\mathbf{J},\mathbf{J}')$ is that the torque δM acting on some isolated (trial) orbit with the action $\mathbf{J}$ from all of the orbits with a fixed action $\mathbf{J}'$, i.e., identical in shape but with all of the possible orientations of the major axes, is proportional to it:

$$\delta M = \frac{imG}{2\pi}\exp(im\bar{w}_2)\Pi(\mathbf{J},\mathbf{J}')\mathcal{F}^{(1)}(\mathbf{J}')d\mathbf{J}'. \quad (20)$$

For an almost Coulomb field $\Phi_0(r)$, $J_f^C = I_1 + I_2$ takes the place of the Lynden-Bell invariant $J_f = I_1 + I_2/2$ in (17) and $\exp[-im(w_1' - w_1)]$ (with an arbitrary m) appears in (19) in place of $\exp[-im(w_1' - w_1)/2]$ (with the condition of an even m).

2.2. The Instability of Elongated Orbits

We hope to reduce Eq. (17) to one-dimensional integral equations in the following two extreme cases: (1) when the distribution function $\mathcal{F}_0(\mathbf{J})$ is similar to the δ function in L near some L_0; we will note this circumstance by writing $\mathcal{F}_0 = \Delta_1(J_f, L - L_0) \approx \delta(L - L_0)\varphi_0(J_f)$, and (2) for systems with nearly circular orbits; in this case, $f_0 = \Delta_2(I_1, I_2)$, where $\Delta_2 \approx \delta(I_1)\bar{\varphi}_0(I_2)$. Below, we consider the first case in detail. Technically, the second case is slightly more complex; we will return to it in a separate paper.

Thus, we assume that $\mathcal{F}_0 = \Delta_1(J_f, L - L_0)$. Since the functions Π and χ change only slightly on the characteristic scale of the change of the function $(\partial\mathcal{F}_0/\partial L')/[\bar{\omega} - m\delta\Omega_{\rm pr}(J_f', L')]$ in L', Eq. (17) can be reduced to the following integral equation for the function of one variable $\psi(J) \equiv \chi(J, L' = L_0)$ (below, for brevity, we omit the subscript f in the Lynden-Bell integral J_f):

$$\psi(J) = \frac{Gm}{2\pi}\int dJ' P(J,J')S_0(J')\psi(J'), \quad (21)$$

where

$$P(J,J') = \Pi(J,J',L = L_0, L' = L_0), \quad (22)$$

$$S_0(J') = \int dL' \frac{\partial\mathcal{F}_0(J',L')/\partial L'}{\bar{\omega} - m\delta\Omega_{\rm pr}(J',L')}. \quad (23)$$

A more convenient form for the function $S_0$is obtained after the integration of (23) by parts:[4]

$$S_0(J') = -m\int dL' \frac{\mathcal{F}_0(J',L')\partial\Omega_{\rm pr}(J',L')/\partial L'}{[\bar{\omega} - m\delta\Omega_{\rm pr}(J',L')]^2}, \quad (24)$$

where the derivative $\partial\Omega_{\rm pr}/\partial L'$ can be calculated at $L' = L_0$ and factored outside the integral sign over L'.

For nearly radial orbits, we can set $L_0 = 0$ when calculating the function $P(J,J')$. In addition, it is easy to verify that $\delta\varphi \equiv \varphi' - \varphi \approx \bar{w}_2' - \bar{w}_2$ for such orbits. Therefore, the function Π can be represented in this case in a slightly simpler form:

$$\Pi(\mathbf{J},\mathbf{J}') = \int dw_1 dw_1' J_m[r(\mathbf{J},w_1), r(\mathbf{J}',w_1')], \quad (25)$$

where

$$J_m(r,r') = \frac{1}{2\pi}\int_0^{2\pi} d\alpha\Gamma(r,r',\alpha)\cos m\alpha. \quad (26)$$

If the orbits are purely radial (an azimuthally "cold" system); i.e., $\mathcal{F}_0 = \delta(L)\varphi_0(J)$, then

$$S_0(J') = -\frac{m}{\bar{\omega}^2}A(J')\varphi_0(J'), \quad (27)$$

where

$$A(J') = \left.\frac{\partial\Omega_{\rm pr}(J',L')}{\partial L'}\right|_{L'=0}. \quad (28)$$

Accordingly, the integral equation (21), which then describes the instability of the radial orbits in a cold system, is

$$\psi(J) = -\frac{Gm^2}{2\pi\omega^2}\int dJ' P(J,J')A(J')\varphi_0(J')\psi(J'). \quad (29)$$

It is easy to prove the positiveness of the function $J_m(r,r')$ from (26) and, hence, $\Pi(\mathbf{J},\mathbf{J}')$ in (25) and, above all, the function $P(J,J')$ from (22) at $L_0 = 0$, which appears in Eq. (29). Let us do this explicitly. Expanding the function $(r^2 + r'^2 - 2rr'\cos\alpha)^{-1/2}$ in terms of Legendre polynomials, we obtain

$$J_m(r,r') = \sum_{n=0}^{\infty} F_n(r,r')\frac{1}{\pi}\int_0^{\pi} d\alpha P_n(\cos\alpha)\cos m\alpha,$$

where

$$F_n(r,r') = r_<^n/r_>^{n+1}, \quad r_< \equiv \min(r,r'), \quad r_> \equiv \max(r,r'), \quad (30)$$

and P_n are the Legendre polynomials. The positive definiteness of J_m now follows from the fact that $P_n(\cos\alpha)$, in turn, can be expanded in terms of the cosines of the multiple angles with positive coefficients (Gradshtein and Ryzhik 1971),

$$P_n(\cos\alpha) = \frac{(2n-1)!!}{2^{n-1}n!} \times \left[\cos n\alpha + \frac{1}{1}\frac{n}{2n-1}\cos(n-2)\alpha + \ldots\right]$$

[4] It is easy to see that in going from (17) to (21) with the function S_0 in form (24), we disregard the terms that contain additional smallness of the order of $\Omega_{\rm pr}/\Omega_1$.

$$\equiv \sum_k{}' A_k^{(n)} \cos k\alpha,$$

with all $A_k^{(n)} > 0$ (the prime implies that the evenness of k must be identical to the evenness of n), as well as from the inequality

$$\frac{1}{\pi}\int_0^\pi d\alpha \cos m\alpha \cos n\alpha = \frac{\delta_{mn}}{2}.$$

As a result, we also obtain a convenient representation of $J_m(r, r')$ in the form of a simple series:

$$J_m(r, r') = \frac{1}{2}\sum_{n\geq m}{}' F_n(r, r') A_m^{(n)} > 0.$$

With the proved positiveness of the function $P(J, J')$, the sign of the integrand in (29) and, hence, the sign of ω^2 (i.e., the stability or instability of a system with purely radial orbits) depend on the sign of $A(J')$ defined by equality (28). If $A > 0$ for all orbits of the system under consideration (i.e., for all values of J or, equivalently, for any energies of the radial stellar oscillations E), then $\omega^2 < 0$. Consequently, for $A > 0$, the radial orbit instability takes place. In contrast, for $A < 0$, a purely oscillation mode takes the place of the instability. The most compact formula to calculate the quantity $A(E)$ is

$$A(E) = \frac{1}{(2E)^{1/2}} \times \frac{\lim\limits_{r_0\to 0}\left\{\int\limits_{r_0}^{r_{\max}} \frac{dx}{x^2[1-\Phi_0(x)/E]^{1/2}} - \frac{1}{r_0}\right\}}{\int\limits_0^{r_{\max}} \frac{dx}{[2E-2\Phi_0(x)]^{1/2}}},$$

where $\Phi_0(r_{\max}) = E$.

The inequality $(\partial\Omega_{\rm pr}/\partial L)|_{L=0} > 0$ is only a necessary (but not sufficient) condition for the instability of radial orbits and, in particular, the bar formation. The insufficiency of this criterion is clear even from the fact that the decelerating torque from the bar may be ineffective for high (on average) orbital precession angular velocities. To determine the true bar-formation conditions, we must solve the problem on the stabilization of the radial orbit instability by a finite precession velocity dispersion (while also making sure that the bar mode ($m = 2$) is preferential). Actually, the bar-formation criterion is nothing but the instability condition for the bar mode of the type under consideration. Therefore, we turn to the derivation of the stabilization conditions for the instability in systems with nearly radial orbits.

For certainty, we adopt the Maxwell distribution function in L:

$$\mathcal{F}_0 = \frac{1}{\sqrt{\pi}L_T}\exp(-L^2/L_T^2)\varphi_0(J), \qquad (31)$$

where L_T is the thermal spread. Assuming in (23) that $\bar{\omega} = \omega = 0$, $L_0 = 0$, $\delta\Omega_{\rm pr} = \Omega_{\rm pr} \approx A(J)L$, we will then have for the stability boundary of the system

$$S_0(J') = 2\varphi_0(J')/mL_T^2 A(J'),$$

so the integral equation (21) takes the form

$$\psi(J) = \frac{G}{\pi L_T^2}\int dJ' P(J, J')\frac{\varphi_0(J')}{A(J')}\psi(J'). \qquad (32)$$

This equation is almost identical to Eq. (29). A comparison of these two equations leads us to conclude that there is a simple relationship between the instability increment γ for a system with purely radial orbits, $\gamma^2 = -\omega^2$, and the orbital angular momentum dispersion that is minimally required for the stabilization of this instability:

$$(L_T)_{\min} = 2^{1/2}\gamma/m\bar{A}, \qquad (33)$$

where $\bar{A}$ is a quantity averaged over the orbits of different energies E.

Relation (33) acquires a definite meaning when all of the stars have almost the same energy $E \approx E_0$, because in this case we can set $\bar{A} = A(E_0)$. If we change to the distribution in precession angular velocities $\Omega_{\rm pr} = AL$ in (31), then we will have a clearer relation in place of (33):

$$(\Omega_{\rm pr})_T = 2^{1/2}\gamma(m)/m, \qquad (34)$$

where $(\Omega_{\rm pr})_T$ denotes the thermal spread of precession angular velocities, and the instability increment γ is written as $\gamma(m)$ to emphasize that, in general, it depends on the azimuthal number m. However, since the dependence $\gamma(m)$ is weak,[5] it follows from (34) that the modes with the minimum possible m are most difficult to stabilize (in this sense, they are most unstable). For nearly radial orbits, $m_{\min} = 2$, which corresponds to the formation of an elliptical bar from an initially circular disk. All of the modes with odd m, in particular, the $m = 1$ mode, are suppressed in this case: for these modes, oppositely directed (and equal in magnitude) torques would act on the two halves of the elongated orbit; they break but do not rotate such orbits—"spokes."

[5] For example, $\gamma(m) \propto m^{1/2}$ for $m \gg 1$. For $m \gg 1$, expression (25) for the function Π simplifies, because in this case $J_m \approx \delta(r - r')/m$. Therefore, one of the integrations in (25) is removed. It is most convenient to derive the asymptotic expression for J_m directly from the Poisson equation by assuming that $m^2\Phi_1/r^2 \gg |d^2\Phi_1/dr^2|, |r^{-1}d\Phi_1/dr|$.

On the other hand, it can be shown that, for example, for nearly circular orbits in a potential similar to the potential of a central point mass, precisely the $m = 1$ mode is preferential.

To conclude this section, we give the integral equation of type (21) in a form convenient for calculating the low-frequency modes of a stellar disk with the equilibrium distribution function $f_0(E, L)$ that contains an appreciable fraction of elongated orbits:

$$f(E_1) = \int_{E_{\min}}^{E_{\max}} K(E_1, E_2) f(E_2) dE_2, \qquad (35)$$

where

$$K(E_1, E_2) = -\frac{\pi}{M_1(E_1)} \qquad (36)$$
$$\times \int_0^{L_{\max}} \frac{f_0(E_1, L_1)}{(\Omega_\mathrm{p} - \Omega_\mathrm{pr}^{(1)})^2} \Omega'_\mathrm{pr}(E_1, L_1) dL_1$$
$$\times \int_0^a \int_0^a dx dy \rho^{(E_1)}(x) \rho^{(E_2)}(y) J_m(x, y).$$

We assume that the torque produced by the attraction of two elongated orbits can be approximately calculated by replacing each actual oval orbit with a precessing spoke that coincides with the semimajor axis of the oval; the linear density of the spoke is $\rho_l^{(E)} = 1/v_r(E) = 1/\sqrt{2E - 2\Phi_0(r)}$, E is the energy of the star, v_r is its radial velocity, $M_1(E) = \int_0^a \rho_l^{(E)}(r) dr$ is the mass of the half-spoke, and $2a$ is the spoke length:

$$\Omega'_\mathrm{pr}(E, L) = \left.\frac{\partial \Omega_\mathrm{pr}}{\partial L}\right|_{J_f} = \frac{\partial \Omega_\mathrm{pr}}{\partial L} + \Omega_\mathrm{pr} \frac{\partial \Omega_\mathrm{pr}}{\partial E}.$$

Using Eq. (35) (which is given without its derivation), one of us (Polyachenko 1992) calculated the "anomalously low-frequency" bar modes that Athanassoula and Sellwood (1986) encountered in their N-body simulations of the linear stability of some accurate models for stellar disks. These frequencies were anomalously low in comparison with the frequencies of the standard (fast) bars that the above authors obtained for most of the models studied. Actually, the angular velocities of the low-frequency modes are approximately equal to the mean orbital precession angular velocities in the central disk region. Therefore, we can say that, here, the instability of elongated orbits takes place. Figures 1a and 1b show how the typical orbit involved in the instability of a slow bar mode appears; it corresponds to the energy and angular momentum of the star averaged over the bar region. The orbit is actually strongly elongated, which justifies the use of Eq. (35) with

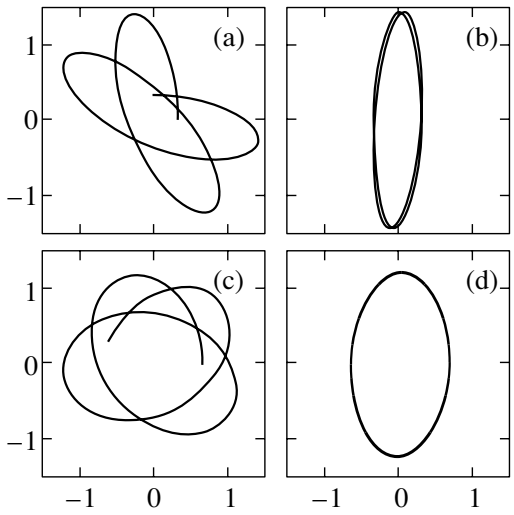

Fig. 1. Typical stellar orbits in the Shuster models considered by Athanassoula and Sellwood (1986) (a) in the models with the lowest mean precession angular velocities and angular momenta; (b) the same as (a) in the frame of reference that corotates with the precessing orbit; (c) in most models; and (d) the same as (c) in the frame of references that corotates with the precessing orbit.

kernel (36). The calculated instability increments (Polyachenko 1992) proved to be in good agreement with those obtained in their N-body simulations by Athanassoula and Sellwood (1986). On the other hand, Figures 1c and 1d show a similar typical orbit for the models in which only a fast bar orbit develops. This mode is much rounder than that in Figs. 1a and 1b. Therefore, to find the low-frequency eigenmodes in these models, it seems more appropriate to use the general integral equation (15) or (17). However, even the integral equation (35), (36), although it is definitely a rough approximation for these models, may give satisfactory numerical agreement with the N-body results of Athanassoula and Sellwood. We plan to study all of these questions in a separate paper.

3. DISCUSSION OF THE POSSIBLE EXISTENCE OF EIGENMODES WITH RELATIVELY HIGH FREQUENCIES ($\mathrm{Re}\Omega_\mathrm{p} > \Omega_\mathrm{pr}^{\max}$)

3.1. The Bar Mode in a Two-Component Model Disk

We write the dispersion relation that is derived from (35) and (36) for a one-component system with the equilibrium distribution function $f_0 = A\delta(E - E_0^{(1)})\delta(L - L_0^{(1)})$ as

$$1 + \frac{g_1}{(\Omega_\mathrm{p} - \Omega_1)^2} = 0, \qquad (37)$$

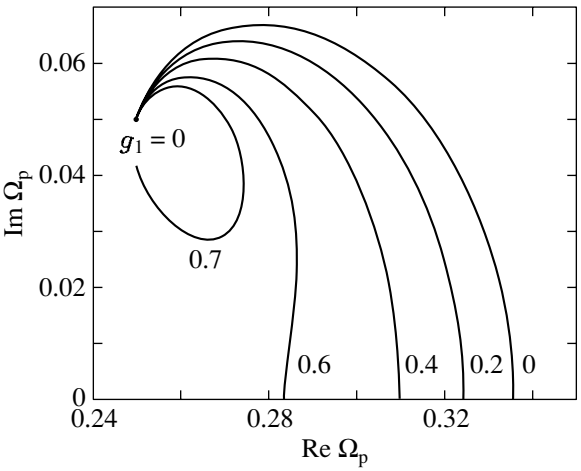

Fig. 2. Trajectories of the unstable root in a two-component model with $g_1 < 0$ and $g_2 > 0$ for several values of the coefficient α: 0, 0.2, ..., 0.7. The absolute value of g_1 increases along the trajectory; the starting point corresponds to $g_1 = 0$.

where $\Omega_1 \equiv \Omega_{pr}(E_0^{(1)}, L_0^{(1)})$ and we use the notation $g_1 \propto \Omega'_{pr}(E_0^{(1)}, L_0^{(1)})$ for the coefficient whose exact expression can be easily obtained from (35) and (36) by substituting the δ-shaped distribution function. The instability in (37) corresponds to $g_1 > 0$.

Let us now consider a two-component system with the distribution function $f_0 = A\delta(E - E_0^{(1)})\delta(L - L_0^{(1)}) + B\delta(E - E_0^{(2)})\delta(L - L_0^{(2)})$. Simple manipulations with the equation that is obtained after substituting this expression into (35) and (36) then yield the dispersion relation

$$1 + \frac{g_1}{(\Omega_p - \Omega_1)^2} + \frac{g_2}{(\Omega_p - \Omega_2)^2} + \alpha\frac{g_1 g_2}{(\Omega_p - \Omega_1)^2(\Omega_p - \Omega_2)^2} = 0, \quad (38)$$

where $g_2 \propto \Omega'_{pr}(E_0^{(2)}, L_0^{(2)})$ is similar to the earlier introduced coefficient g_1 for the first component, $\Omega_2 \equiv \Omega_{pr}(E_0^{(2)}, L_0^{(2)})$, and the following notation is used:

$$\alpha = 1 - \frac{I_0^2(E_0^{(1)}, E_0^{(2)})}{I_0(E_0^{(1)}, E_0^{(1)})I_0(E_0^{(2)}, E_0^{(2)})}, \quad (39)$$

$$I_0(E_0^{(i)}, E_0^{(j)}) \equiv \int_0^{a_i}\int_0^{a_j} dxdy\rho^{(E_i)}(x)\rho^{(E_j)}(y)J_m(x,y). \quad (40)$$

The possible positions of $\mathrm{Re}\Omega_p$ for unstable roots ($\gamma \equiv \mathrm{Im}\Omega_p > 0$) turn out to significantly depend on whether the signs of the coefficients g_1 and g_2 are identical (positive in the case of instability) or different, i.e., on whether there are orbits with donkey behavior in the disk for which $g_1 \propto \Omega'_{pr}(E_0^{(1)}, L_0^{(1)}) < 0$ (we assume that $g_2 > 0$).

Let us first prove that the inequality $\Omega_1 \le \mathrm{Re}\Omega_p \le \Omega_2$ holds at positive g_1 and g_2. To prove this, it will suffice to calculate

$$A_{1,2} \equiv \mathrm{Im}\frac{g_{1,2}}{(\Omega_p - \Omega_{1,2})^2} = -\frac{2g_{1,2}\gamma\Delta_{1,2}}{(\Delta_{1,2}^2 + \gamma^2)^2},$$

$$\Delta_{1,2} \equiv \mathrm{Re}\Omega_p - \Omega_{1,2};$$

$$B \equiv \mathrm{Im}\frac{\alpha g_1 g_2}{(\Omega_p - \Omega_1)^2(\Omega_p - \Omega_2)^2} = -\frac{2g_1 g_2 \alpha\gamma}{(\Delta_1^2 + \gamma^2)^2(\Delta_2^2 + \gamma^2)^2} \times [(\Delta_2^2 + \gamma^2)\Delta_1 + (\Delta_1^2 + \gamma^2)\Delta_2].$$

If $\mathrm{Re}\Omega_p > \Omega_2$, then $\Delta_1 > 0$, $\Delta_2 > 0$. Thus, in this case, the imaginary part of the left-hand side of Eq. (38) would be strictly negative for $\gamma > 0$:

$$A_1 + A_2 + B < 0$$

(rather than equal to zero) when it is considered that $\alpha > 0$. The latter follows from the Cauchy–Bunyakowsky inequality (the positiveness of the weighting function $J_2(x, y)$ was proven in the previous section).

Similarly, for $\mathrm{Re}\Omega_p < \Omega_1$, all of the inequalities reverse (except, of course, $\alpha > 0$) $\Delta_1 < 0$, $\Delta_2 < 0$:

$$A_1 + A_2 + B > 0.$$

The situation for $g_2 > 0$ and $g_1 < 0$ is completely different. Figure 2 shows the trajectories of the only unstable root in the complex Ω_p plane for a fixed $g_2 = 0.05^2 > 0$ ($\Omega_1 = 0$ and $\Omega_2 = 0.25$ are also fixed) and negative g_1 that change along each trajectory from $g_1 = 0$ to some $(g_1)_{min}$ at which this root also becomes real. Different trajectories correspond to different values of the parameter α.

An important point is not only the fact that $\mathrm{Re}\Omega_p$ can be larger than Ω_2 but also the fact, following from our calculations, that $\mathrm{Re}\Omega_p$ can significantly exceed Ω_2 (in our example, by a factor of approximately 1.5).

3.2. Additional Arguments

The sources of the increase in $\mathrm{Re}\Omega_p$ discussed in this section when repelling orbits are taken into account can be found even in the dispersion relation (37) for a one-component system. Indeed, for $g_1 > 0$ (the unstable case where the orbits under consideration are attracting), we have

$$\Omega_p = \Omega_1 \pm i\sqrt{g_1}. \quad (41)$$

Therefore, here, $\mathrm{Re}\Omega_\mathrm{p} = \Omega_1$; i.e., $\mathrm{Re}\Omega_\mathrm{p}$ matches $\bar{\Omega}_\mathrm{pr}$ (or $\Omega_\mathrm{pr}^\mathrm{max}$, which is equivalent in this case). On the other hand, for $g_1 < 0$ (the stable case that corresponds to repelling orbits),

$$\Omega_\mathrm{p}^\pm = \mathrm{Re}\Omega_\mathrm{p}^\pm = \Omega_1 \pm \sqrt{-g_1}. \quad (42)$$

In this case, the root Ω_p^+ corresponds to $\mathrm{Re}\Omega_\mathrm{p} > \Omega_\mathrm{pr}^\mathrm{max}$ (while for the second root, we can see that $\mathrm{Re}\Omega_\mathrm{p} < \Omega_\mathrm{pr}^\mathrm{min}$).

The dispersion relation (37) for $g_1 < 0$, to within the notation, is identical to the dispersion relation for the electron Langmuir oscillations of a cold plasma:

$$1 - \frac{\omega_\mathrm{p}^2}{(\omega - kV)^2} = 0, \quad (43)$$

where $\omega_\mathrm{p} = \sqrt{4\pi e^2/m_e}$ is the plasma frequency (e and m are the electron charge and mass, respectively); k is the perturbation wave number; and, for the completeness of the analogy, we use the frame of reference in which the plasma moves at a velocity V. This analogy, of course, is by no means surprising, because repelling orbits (for $g_1 < 0$) are actually quite similar to (also repelling!) electrons. By analogy with our two solutions $\Omega_\mathrm{p}^\pm$, in the plasma case (43) we have

$$\left(\frac{\omega}{k}\right)^\pm - V = \pm\frac{\omega_\mathrm{p}}{k}, \quad (44)$$

which corresponds to two oppositely traveling (in the frame of reference comoving with the plasma) symmetric electron density waves. Clearly, the orbit density waves can be interpreted in exactly the same way (in the frame of reference rotating with the precession velocity Ω_1).

However, the real situation in which the disks have a continuous distribution of orbits in energy and angular momentum (and, accordingly, in precession angular velocity) rather than a δ-shaped distribution introduces a certain asymmetry by setting off the faster mode. The point is that, actually, the precession angular velocities Ω_pr occupy the entire band from zero to some $\Omega_\mathrm{pr}^\mathrm{max}$: $0 \le \Omega_\mathrm{pr} \le \Omega_\mathrm{pr}^\mathrm{max}$. Therefore, a slower wave with $\Omega_\mathrm{p}^- < \bar{\Omega}_\mathrm{pr}$ will be damped because of its resonant interaction with corotating[6] orbits, which are certain to be found. This damping in the usual description of the disk as a group of stars (rather than orbits) corresponds to the standard damping at the inner Lindblad resonance (see, e.g., Lynden-Bell and Kalnajs 1972). Expressions for the damping decrements can be derived (in a way simpler than the standard method) from the dispersion relations that generalize (37) to the distributions of orbits spread over Ω_pr; for very simple cases, these dispersion relations also appear quite similar to the corresponding dispersion relation for the oscillations of a warm electron plasma (Polyachenko 1991).

For a fast wave, Ω_p^+ can easily become larger than $\Omega_\mathrm{pr}^\mathrm{max}$; clearly, such a wave will be undamped (in our approximation), because there are no orbits corotating with the wave in this case. The search for (to be more precise, the simplest description in terms of our theory) such undamped modes seems of relevant interest for future studies. Incidentally, the standard (Lynden-Bell and Kalnajs 1972) resonant instability of the wave generated by "ordinary" corotation, where $\Omega_\mathrm{p} = \Omega(r_\mathrm{CR})$ and $\Omega(r)$ is the angular frequency of the star in circular orbits, can cause a slight growth of these modes. However, the treatment of this instability is outside the validity range of our theory.

To conclude this section, we note that we used an approximation that was quite justifiable only for sufficiently elongated orbits. At the same time, the repelling orbits must be fairly round. Therefore, let us introduce the dispersion relation for a one-component system with arbitrarily elongated orbits based on the general integral equation (17). Substituting the distribution function

$$\mathcal{F}_0(\mathbf{J}') = A\delta(J' - J_0)\delta(L' - L_0)$$

into (17) yields

$$\psi(L) = -\frac{GA}{2\pi}\left[\left(\frac{\Omega'_\mathrm{pr}(L_0)}{(\Omega_\mathrm{p} - \Omega_\mathrm{pr}(L_0))^2}\pi(L, L_0) + \frac{1}{\Omega_\mathrm{p} - \Omega_\mathrm{pr}(L_0)}\left.\frac{\partial\pi(L, L')}{\partial L'}\right|_{L_0}\right)\psi(L_0) + \frac{\pi(L, L_0)}{\Omega_\mathrm{p} - \Omega_\mathrm{pr}(L_0)}\psi'(L_0)\right], \quad (45)$$

where $\psi(L) = \chi(J_0, L)$ and $\pi(L, L') \equiv \Pi(J_0, L; J_0, L')$. Differentiating (45) with respect to L and assuming that $L = L_0$, we obtain an equation that, together with Eq. (45), at $L = L_0$ forms a homogeneous system of equations for the unknowns $\psi(L_0)$ and $\psi'(L_0)$. Setting the determinant of this system equal to zero, we derive a dispersion relation that can be transformed into

$$1 + \frac{GA}{2\pi}\frac{\pi(L_0, L_0)\Omega'_0}{(\Omega_\mathrm{p} - \Omega_0)^2} + \frac{GA}{2\pi}\pi(L_0, L_0) \times \frac{\left.\frac{\partial \ln\pi(L, L')}{\partial L'}\right|_{L_0} + \left.\frac{\partial \ln\pi(L, L_0)}{\partial L}\right|_{L_0}}{\Omega_\mathrm{p} - \Omega_0} \quad (46)$$

[6] In our case, this implies orbits with $\Omega_\mathrm{pr} = \Omega_\mathrm{p}$; in the usual description, this is the inner Lindblad resonance rather than the corotation one!

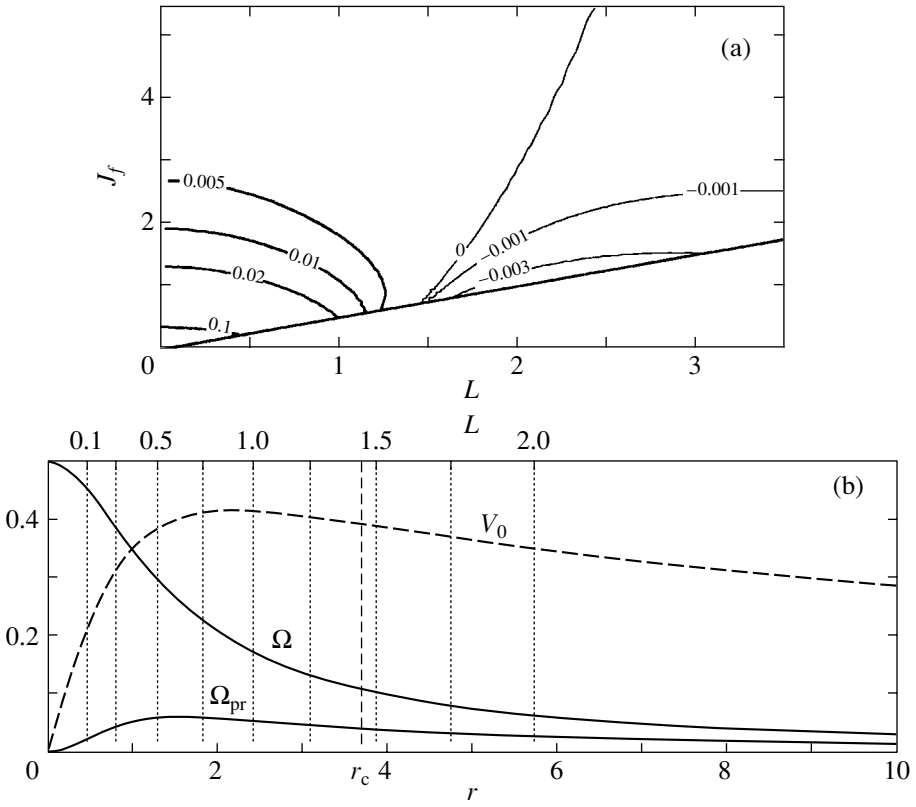

Fig. 3. (a) The pattern of orbital precession for the isochronic model in the Lynden-Bell (J_f, L) plane. The straight line $J_f = L/2$ corresponds to circular orbits. The isolines for the Lynden-Bell derivative $\Omega'_{\rm pr}$ are shown. (b) The disk angular velocity $\Omega(r)$, the rotation curve $V_0(r)$, and the precession angular velocity of circular orbits $\Omega_{\rm pr}(r)$ for the isochronic model.

$$-\left(\frac{GA}{2\pi}\right)^2 \pi^2(L_0,L_0)\frac{\left.\dfrac{\partial^2 \ln \pi(L,L')}{\partial L\partial L'}\right|_{L_0}}{(\Omega_{\rm p}-\Omega_0)^2} = 0,$$

where we denoted $\Omega_0 \equiv \Omega_{\rm pr}(J_0, L_0)$ and $\Omega'_0 \equiv \Omega'_{\rm pr}(J_0, L_0)$ and took into account the fact that

$$\frac{\pi(L_0,L_0)\left.\dfrac{\partial^2\pi(L,L')}{\partial L\partial L'}\right|_{L_0} - \left.\dfrac{\partial\pi(L_0,L')}{\partial L'}\right|_{L_0}\left.\dfrac{\partial\pi(L,L_0)}{\partial L}\right|_{L_0}}{\pi^2(L,L_0)} = \left.\frac{\partial^2 \ln \pi(L,L')}{\partial L\partial L'}\right|_{L_0}.$$

In general, all of the terms that appear in the dispersion relation (46) are of the same order of magnitude. Only for strongly elongated orbits (small L) can the last two terms be discarded as containing additional smallness of the order of $\Omega_{\rm pr}/\Omega_1$. Thus, the dispersion relation

$$1 + \frac{GA}{2\pi}\frac{\pi(L_0,L_0)\Omega'_0}{(\Omega_{\rm p}-\Omega_0)^2} = 0, \qquad (47)$$

which, as can be easily seen, corresponds to the Lynden-Bell pattern of instability growth, is strictly justifiable only in this case. However, at low values of the ratio $\omega_{\rm G}/\Omega_0$ ($\omega_{\rm G}^2 = g$ in the notation of this section), the two additional (compared to (47)) terms of the dispersion relation (46) are small in comparison with the remaining terms exactly in the ratio $\omega_{\rm G}/\Omega_0$ and, then, as before, $\Omega_{\rm p}^+ \approx \Omega_0 + \omega_{\rm G} > \Omega_0$. Clearly, in this situation, for example, a twofold excess of $\Omega_{\rm p}^+$ above Ω_0 (which corresponds to the validity boundary of approximation (47)) would come as no surprise. However, an accurate analysis of Eq. (46) becomes model-dependent and will be the subject of a future, more detailed analysis. This is also true for the corresponding refinements of the dispersion relation for two-component models.

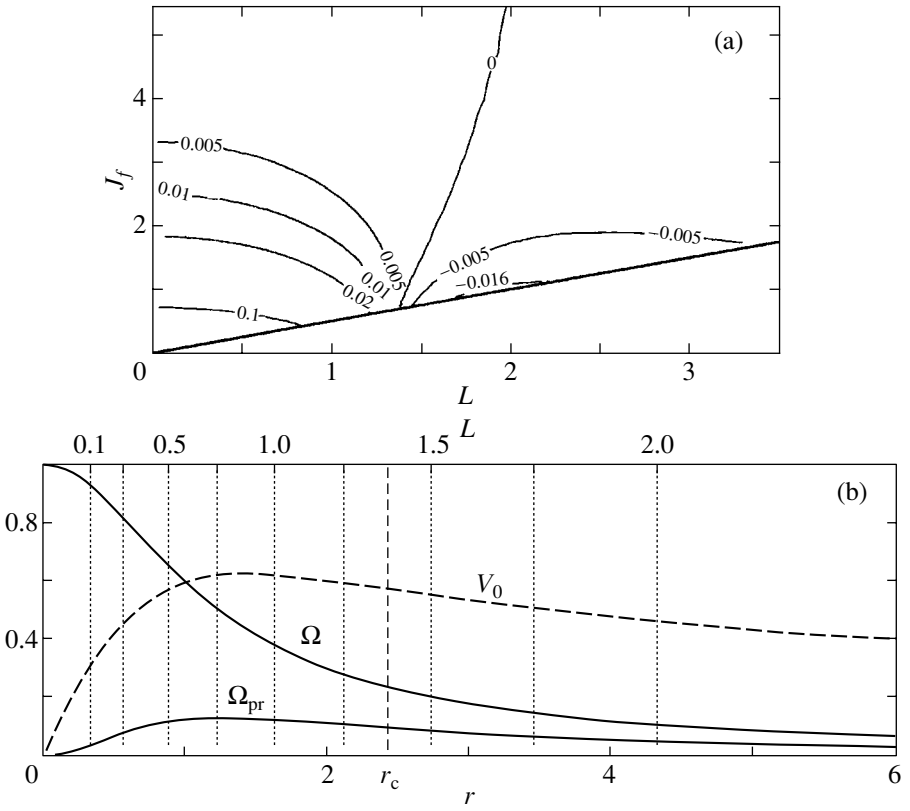

Fig. 4. Same as Fig. 3 for the Schuster potential.

4. THE PATTERN OF ORBITAL PRECESSION IN SOME POTENTIALS

Figures 3a, 4a, 5a, and 6a show the lines of constant derivative $\Omega'_{\rm pr} \equiv (\partial\Omega_{\rm pr}/\partial L)_{J_f}$ in the (J_f, L) plane for several typical potentials. Figures 3b, 4b, 5b, and 6b show the angular velocities $\Omega(r)$ of the stars in circular orbits, the rotation curves $V_0(r) = r\Omega(r)$, and the precession angular velocities of nearly circular orbits $\Omega_{\rm pr}(r) = \Omega(r) - \kappa(r)/2$ (where $\kappa(r)$ is the epicyclic frequency) for the same potentials.

The first pair of these figures (Figs. 3a, 3b) corresponds to the isochronic potential

$$\Phi_0(r) = -\frac{1}{1+\sqrt{1+r^2}}.$$

This case was considered by Lynden-Bell (1979). Here, the frequencies $\Omega_1(J_f, L)$ and $\Omega_2(J_f, L)$, along with the quantities $\Omega_{\rm pr}(J_f, L) = \Omega_2(J_f, L) - \Omega_1(J_f, L)/2$ and $\Omega'_{\rm pr}(J_f, L)$ concerned, can be calculated analytically. For us, the example of the isochronic potential served as a test for the general numerical scheme of calculating $\Omega_{\rm pr}$ and $\Omega'_{\rm pr}$ for arbitrary potentials $\Phi_0(r)$.

In addition to the isochronic potential, we performed calculations for the Schuster potential

$$\Phi_0(r) = -\frac{1}{\sqrt{1+r^2}}$$

(Figs. 4a, 4b), the logarithmic potential $\Phi_0(r) = \ln r$, which corresponds to a flat rotation curve $V_0 = \text{const}$ (Figs. 5a, 5b), and the potential of an exponential disk (Freeman 1970)

$$\Phi_0(r) = rI_1(r/2)K_0(r/2),$$

where I_1 and K_0 are the corresponding Bessel functions (Figs. 6a, 6b).

Qualitatively, Figs. 3a, 4a, 6a and 3b, 4b, 6b are similar but differ greatly from Figs. 5a and 5b for the logarithmic potential (which is quite natural). Of greatest interest in Figs. 3a, 4a, and 6a seems to be the possibility of determining the critical values ($L_{\rm c}$) that separate the regions of attracting (for $L < L_{\rm c}$) and repelling (for $L > L_{\rm c}$) nearly circular orbits. The critical radii ($r_{\rm c}$) that correspond to these $L_{\rm c}$ are shown in Figs. 3b, 4b, and 6b. It would be natural to take $r_{\rm c}$ as an estimate of the length $l_{\rm b}$ of the bar that is formed by the instability mechanism under consideration, at least at the linear stage. In all cases, $r_{\rm c}$ is much larger than the radii r_m and r'_m that correspond to the maxima of the rotation curve $V_0(r)$

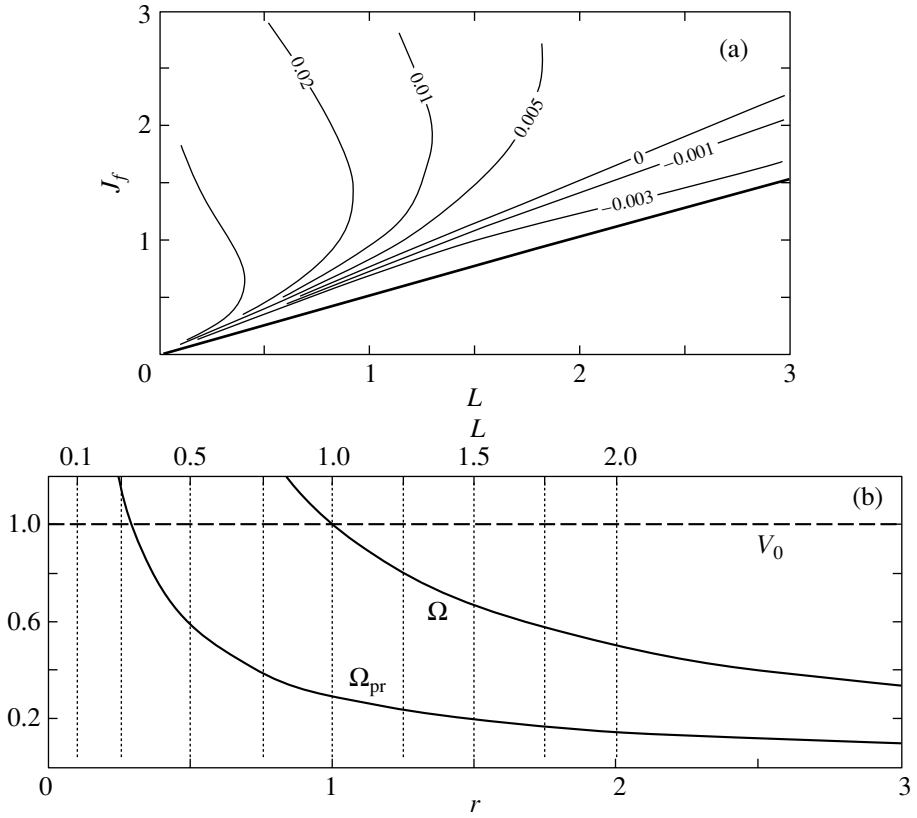

Fig. 5. Same as Fig. 3 for the logarithmic potential.

and the function $\Omega_{\rm pr}(r)$. If we assume (as is commonly done for fast bars) that the bar ends near corotation, then we will have the following estimate of the bar angular velocity for the Schuster potential at $l_{\rm b} \approx r_{\rm c}$: $\Omega_{\rm p} \approx 0.23$ (see Fig. 4b). The corresponding frequency $\omega = 2\Omega_{\rm p} \approx 0.46$ is typical of most of the models (in the Schuster potential) studied by Athanassoula and Sellwood (1986). These bars were commonly classified as fast ones, having in mind, primarily, the putative non-Lynden-Bell mechanism of their formation. However, we see that the Lynden-Bell mechanism may, probably, lead to the formation of such bars.

Below, we also point out some other curious properties, which are apparently common to the pattern of orbital precession in potentials $\Phi_0(r)$ of the types that correspond to Figs. 3a, 4a, and 6a:

(1) The precession angular velocity $\Omega_{\rm pr}^{\rm max}$ that corresponds to the maximum of the curve $\Omega_{\rm pr}(r)$ in circular orbits is an absolute maximum for the precession angular velocities $\Omega_{\rm pr}(J_f, L)$ of any orbits; $\Omega_{\rm pr}^{\rm max}$ for the three models is given in the first row of the table.

(2) $\Omega_{\rm pr}'^{\rm max}$ is reached in circular orbits at the disk center ($J_f \to J_r \to 0,\ L \to 0$); $\Omega_{\rm pr}'^{\rm max}$ for the three models are given in the third row of the table.

(3) $\Omega_{\rm pr}'^{\rm min}$ is also reached at some point in a circular orbit; $\Omega_{\rm pr}'^{\rm min}$ are given in the fourth row of the table.

A few words should be said separately about the precession pattern in the logarithmic potential, which is typical of most of the disks of many spiral galaxies (Fig. 5a). Here, of greatest interest is the fact that $\Omega_{\rm pr}' < 0$ in a narrow sector adjacent to the line of circular orbits $J_f = L/2$. However, the narrowness of this sector is apparent: actually, the orbits of all stars in any reasonable model of a spiral galaxy lie in the (J_f, L) plane deep inside this sector, in the immediate vicinity of the line of circular orbits. Using the epicyclic approximation (which is quite natural in our case), we can easily show that the straight lines in the (J_f, L) plane are the lines of constant ratio (c_r/V_0), where V_0 and c_r are the circular and radial velocities, respectively so $L = rV_0$ and the epicycle size is $a = c_r/\kappa$, $I_1 = \kappa a^2/2$. The equations of these straight lines are $I_1 = \beta L$ (or $J_f = (0.5 + \beta)L$), where the coefficient $\beta = \alpha^2/2\sqrt{2}$ is numerically small ($\alpha \equiv c_r/V_0$).

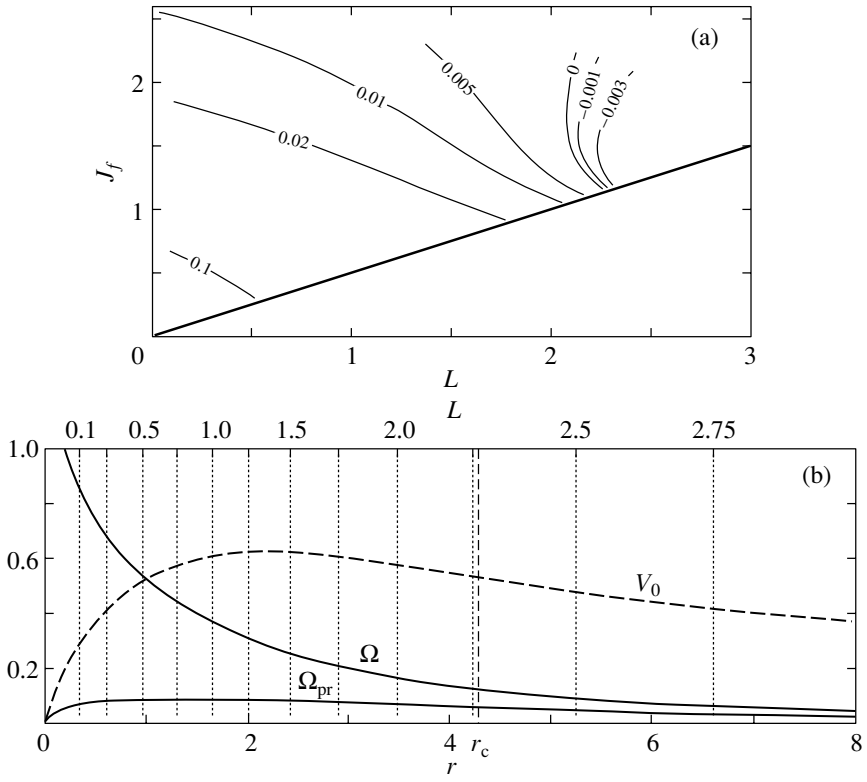

Fig. 6. Same as Fig. 3 for the potential of an exponential disk.

To conclude this section, we note that the arrays of values obtained above for the functions $\Omega_{pr}(J_f, L)$ and $\Omega'_{pr}(J_f, L)$ will subsequently be used in solving integral equations (17) and (21) to determine the eigenfrequencies and shapes of the bar modes (primarily for stellar models in the Schuster potential).

5. CONCLUSIONS

Below, we formulate and discuss some of the conclusions that were drawn from our theory.

(1) We gave several arguments for the universality of the bar-formation mechanism that may be responsible for the formation of not only slow bars but also fast bars. It would be natural to formulate the essence of this mechanism by representing the stellar disk as a group of precessing orbits. This representation adequately fits the problem under consideration, because the angular velocities of the bars (including fast ones) are much lower than the characteristic oscillation frequencies of individual stars (Ω_1 and Ω_2) but are just of the order of the orbital precession angular velocities (Ω_{pr}). In such a disk, we search for unstable normal modes (primarily the bar mode) as the density wave of precessing orbits that "rigidly" travels in azimuth at some velocity Ω_p, although different orbits precess at different angular velocities (an analogue of the differentiality of the disk rotation when the disk of a spiral galaxy is viewed as a group of individual stars).

An unstable bar mode is formed if there is a sufficiently massive group of attracting orbits in the central disk region (the location of the future bar) that meet the Lynden-Bell requirement $\Omega'_{pr} > 0$ and, at the same time, if the precession velocity dispersion of these active orbits is not too large (otherwise, the orbits will just "run away" from the perturbation region under the effect of "thermal" motion). The latter condition is natural for the basically Jeans mechanism of the instability under consideration. Accurate instability criteria can be obtained by solving the basic equations that were derived in Section 2; for some simple cases, the corresponding dispersion relations are given there in explicit form. The bar angular velocity Ω_p significantly depends on the extent to which the repelling orbits of stars with $\Omega'_{pr} < 0$ (i.e., the orbits with donkey behavior) are involved in the bar formation. If such orbits are only slightly involved in the bar formation, then $\Omega_p \approx \bar{\Omega}_{pr}$; such bars it would be natural to call slow. If, however, the role of "repelling" orbits is significant, then we can obtain fast bars with Ω_p that considerably exceeds $\bar{\Omega}_{pr}$ (nevertheless, Ω_p can still be of the order of $\bar{\Omega}_{pr}$, remaining within the scope of our theory). In Section 3, we showed this possibility by using a two-component disk model

Table 1

Parameter	Isochronic model	Schuster model	Exponential disk
$\Omega_{\rm pr}^{\rm max}$	0.058	0.13	0.087
$r_{\rm c}$	3.7	2.4	4.3
$\Omega'^{\rm max}_{\rm pr}$	0.3–0.35	0.4–0.45	0.35
$\Omega'^{\rm min}_{\rm pr}$	−0.0105	−0.021	−0.025

as a simple example. Thus, from our point of view, the difference between slow and fast bars is mainly quantitative and is not fundamental in nature: they are formed by the same physical mechanism. Note that even from general considerations, the Jeans mechanism (to which our mechanism essentially belongs) is always most natural and preferred in gravitational problems.

(2) So far, the theory suggested above has been confirmed only by the calculation of the lowest frequency modes for disk models in the Schuster potential and by the comparison with the N-body results of Athanassoula and Sellwood (1986). These modes clearly correspond to slow bars: for them, $\Omega_{\rm p} \sim \bar{\Omega}_{\rm pr}$. A crucial decisive test for the most interesting prediction of our theory—its applicability to fast bars—will be the correspondence of the mode eigenfrequencies calculated from the integral equations that we derived above (see Section 2) to the frequencies of fast bars obtained in N-body simulations (in particular, to most of the bar modes from Athanassoula and Sellwood (1986)). This problem will be the subject of our study in the immediate future. For now, we have restricted our analysis only by pointing out some of the favorable facts that follow from the general analysis of the pattern of orbital precession for several potentials that we performed in Section 4. These facts are consistent the formation of a fast bar by the alignment of attracting orbits. First, we noted that the maximum radius ($r_{\rm c}$) of nearly circular orbits with $\Omega'_{\rm pr} > 0$, which can serve as a natural estimate of the bar length $l_{\rm b}$, is much larger than the size of the region ($\sim r_m$) of nearly rigid disk rotation in all reasonable models. Moreover, if we take the standard condition $l_{\rm b} \sim r_{\rm CR}$ (where $r_{\rm CR}$ is the corotation radius), then, for $l_{\rm b} \sim r_{\rm c}$, we obtain an estimate ($\omega \approx 0.46$) for the models in the Schuster potential studied by Athanassoula and Sellwood (1986) for a typical mode eigenfrequency that is in good agreement with their results.

REFERENCES

1. V. I. Arnold, V. V. Kozlov, and A. I. Neishtadt, *Mathematical Aspects of Classical and Celestial Mechanics* (Moscow: URSS, 2002).
2. E. Athanassoula and J. Sellwood, Mon. Not. R. Astron. Soc. **221**, 213 (1986).
3. G. Chew, M. Goldberger, and F. Low, Proc. Roy. Soc. **236**, 112 (1956).
4. G. Contopoulos, Astrophys. J. **201**, 566 (1975).
5. G. Contopoulos and C. Mertzanides, Astron. Astrophys. **61**, 477 (1977).
6. K. C. Freeman, Astrophys. J. **160**, 811 (1970).
7. A. M. Fridman and V. L. Polyachenko, *Physics of Gravitating Systems* (Springer-Verlag, New York, 1984).
8. I. S. Gradshteĭn and I. M. Ryzhik, *Tables of Integrals, Sums and Series* (Nauka, Moscow, 1971).
9. A. J. Kalnajs, Doctoral Dissertation (Harvard Univ., 1965).
10. A. J. Kalnajs, Proc. Astron. Soc. Australia **2**, 174 (1973).
11. D. Lynden-Bell, Mon. Not. R. Astron. Soc. **187**, 101 (1979).
12. D. Lynden-Bell and A. J. Kalnajs, Mon. Not. R. Astron. Soc. **157**, 1 (1972).
13. V. L. Polyachenko, ASP Conf. Ser. **66**, 103 (1994).
14. V. L. Polyachenko, Pis'ma Astron. Zh. **17**, 877 (1991) [Sov. Astron. Lett. **17**, 371 (1991)].
15. V. L. Polyachenko, Astron. Zh. **69**, 10 (1992) [Sov. Astron. **36**, 5 (1992)].
16. V. L. Polyachenko and E. V. Polyachenko, Pis'ma Astron. Zh. **22**, 337 (1996) [Astron. Lett. **22**, 302 (1996)].
17. J. A. Sellwood and A. Wilkinson, Rep. Progr. Phys. **56**, 173 (1993).
18. F. H. Shu, Astrophys. J. **160**, 89 (1970).
19. F. H. Shu, R. V. Stachnik, and J. C. Yost, Astrophys. J. **166**, 465 (1971).
20. A. Toomre, *Structure and Evolution of Normal Galaxies*, Ed. by S. M. Fall and D. Lynden-Bell (Cambridge Univ. Press, Cambridge, 1981), p. 111.

Translated by V. Astakhov

Astronomy Letters, Vol. 29, No. 7, 2003, pp. 463–467. Translated from Pis'ma v Astronomicheskiĭ Zhurnal, Vol. 29, No. 7, 2003, pp. 526–531.

Estimating the Interstellar Extinction and the Contribution from an Accretion Shock to the Formation of Emission Continuum in DS Tau and DG Tau

A. S. Kravtsova*

Sternberg Astronomical Institute, Universitetskii pr. 13, Moscow, 119992 Russia

Received December 11, 2002

Abstract—We analyze the UV spectra of the young stars DG Tau and DS Tau taken with the STIS spectrograph from the Hubble Space Telescope. For these stars, we found the upper limits of the interstellar extinction A_V. Their values proved to be lower than those obtained by other authors from optical observations. For DS Tau, DG Tau, and TW Hya, we also determined the ratio of the flux in the C IV 1550 doublet lines to the excess continuum flux. It proved to be an order of magnitude lower than its value predicted by the accretion-shock (AS) models of Lamzin (1998) and Calvet and Gullbring (1998). It thus follows that for these stars, the emission continuum originates mainly in the accretion disk and/or the boundary layer rather than in the AS, as has been thought previously. Since a similar conclusion has previously been reached for DR Tau, T Tau, and RY Tau, we may assume that the disks around most young stars reach the stellar surface and accretion mainly proceeds through the boundary layer.

Key words: *T Tauri stars, disk accretion, stellar wind.*

INTRODUCTION

T Tauri stars are young stars with masses $\simeq 1 M_\odot$ at the stage of contraction to the main sequence. According to current views, their activity is attributable to mass accretion from the protoplanetary disk onto the central star with a large-scale magnetic field $\sim 10^3$ G in strength, which stops the disk at a distance of ~ 3–$5 R_*$ from the stellar surface. It is generally believed that the disk matter becomes frozen in magnetic field lines and falls to the star along them, accelerating to a velocity of ~ 300 km s^{-1}, and then decelerates in a shock wave. In this model, the line and continuum emission observed in classical T Tauri stars is attributed to the radiation from an accretion shock (AS) (see Najita *et al.* (2000) and references therein).

Kravtsova and Lamzin (2002a, 2002b) have found that the disks around T Tau, RY Tau, and DR Tau reach the stellar surface; the bulk of the accreted matter settles in the equatorial plane of the star and only a small fraction of it flows through the magnetosphere. This conclusion was drawn from comparison of the computed (Lamzin 1998, 2003; Calvet and Gullbring 1998) and observed ratios of the flux in the C IV 1550 doublet lines to the bolometric flux of the emission continuum. Here, we determine this ratio for three more young stars: DS Tau, DG Tau, and TW Hya. We also estimate an upper limit for the interstellar extinction toward DS Tau and DG Tau, because the true flux in the C IV 1550 doublet lines cannot be determined without it.

OBSERVATIONAL DATA

The spectra of DS Tau and DG Tau that we analyze here were obtained in 2000–2001 with the Space Telescope Imaging Spectrograph (STIS) in the medium-resolution mode (programs ID 8206 and 8627). These spectra were taken from the HST archival database (http://archive.stsci.edu/hst/target_descriptions. html). We processed the spectra using the IRAF v2.11 (http://iraf.noao.edu/iraf) and STSDAS/TABLES v2.02 (http://ra.stsci.edu/STSDAS) software packages and the standard techniques described in Chapter 21 of the "HST Data Handbook" (http://www. stsci.edu/documents/datahandbook.html). For each star, Table 1 gives the dates of observations, the spectrum identification numbers in the archive, and the wavelength range covered.

ESTIMATING THE INTERSTELLAR EXTINCTION A_V

We determined the interstellar extinction for DS Tau and DG Tau from their UV spectra. Our

*E-mail: kravts@sai.msu.ru

Table 1. Information on the STIS observations

Star	Date	Spectrum code	$\Delta\lambda$, Å
DS Tau	Aug. 24, 2000	o5cf01010	1650–2300
		o5cf01020	2275–3000
		o5cf01030	1200–1715
		o5cf01040	1200–1715
DG Tau	Feb. 20, 2001	o63l03010	2275–3000
		o63l03020	2275–3000
		o63l03030	2275–3000
		o63l03040	2275–3000

method is based on the fact that the interstellar extinction curve has a maximum near 2200 Å (Bless and Savage 1972), which produces a local dip in the observed spectrum of the star. If we correct the observed continuum energy distribution for interstellar extinction with different values of A_V, then the dip will disappear at some value of A_V and a hump will appear near 2200 Å in place of the dip at larger values. Using this method, we cannot accurately determine A_V without prior knowledge of the undistorted spectral energy distribution for the star. However, an upper limit for A_V can be obtained even without this information: although the position of the hump and its width depend on the star's spectral energy distribution, it would be natural to attribute the very appearance of a hump near 2200 Å starting from some A_V to interstellar extinction; for more details, see Kravtsova and Lamzin (2002a, 2002b).

Figures 1a and 1c show the observed spectra of DS Tau and DG Tau smoothed over 100 data points for clarity. We determined the continuum levels for these stars in several spectral regions examples of which are shown in Fig. 2; here, the smoothing was performed over eight data points. Since these spectral regions contain absorption and emission lines, the continuum level can be determined reliably.[1] Through these data points, we drew a fifth-degree polynomial fit for DG Tau and a cubic spline for DS Tau. They were subsequently taken as the continuum level (see the lower curves in Figs. 1b and 1d). These figures show the spectral energy distributions for DS Tau and DG Tau corrected for interstellar extinction with different values of A_V.

[1] As we see from Table 1, the archive contains spectra for DS Tau in the wavelength range from 1700 to 2300 Å. However, they have such a low quality that the continuum level in this range cannot be drawn reliably. For this reason, the corresponding spectral region is not shown in Fig. 1c.

As we see from Fig. 1, the hump mentioned above appears in the curves for DG Tau at $A_V > 0^m.8$, which allows $A_V = 0^m.8$ to be taken as an upper limit of the interstellar extinction for this star. Similarly, it is reasonable to take $A_V = 0^m.5$ as an upper limit for DS Tau. Note that we used the so-called standard interstellar extinction law $A_\lambda(\lambda)$ (Seaton 1979). However, Kravtsova and Lamzin (2002b) showed that the final A_V value depends only slightly on the chosen extinction law.

For comparison, we give the A_V values obtained by analyzing the optical spectra of DS Tau and DG Tau: $0^m.9$ and $1^m.41$, respectively (White and Ghez 2001). As we see from Fig. 1, these values yield anomalously large humps. Kravtsova and Lamzin (2002a, 2002b) obtained a similar discrepancy for nine other young stars, suggesting the presence of a systematic effect. Analysis of the nature of this effect is beyond the scope of our work. We only point out that it may result from a deviation of the extinction law in the dense dust cloud that surrounds young stars from the standard law typical of the interstellar medium.

THE CONTRIBUTION OF THE FLUX IN THE C IV 1550 LINE DOUBLET TO THE TOTAL LUMINOSITY

If the excess continuum of young stars originates in the AS, then more than 2% of the entire accretion energy must be radiated in the C IV 1550 Å doublet lines (Lamzin 1998, 2003; Calvet and Gullbring 1998). However, for T Tau, DR Tau, and RY Tau, this value proved to be almost two orders of magnitude lower than the computed value (Kravtsova and Lamzin 2002a, 2002b). It thus follows that in these stars, only a small fraction of the veiling continuum originates in the accretion shock. Since this conclusion is of great importance, below we determine the relative intensity of the C IV 1550 Å lines for three more stars: TW Hya, DG Tau, and DS Tau.

Let us first compare the fluxes in the C IV 1550 doublet lines and in the UV (1200–3000 Å) continuum for DG Tau and DS Tau using HST/STIS spectra. The point is that K5-type stars, which DG Tau and DS Tau are, emit virtually no UV radiation. Therefore, the measured flux in the wavelength range from 1200 to 3000 Å is completely attributable to the accretion luminosity.

All our measurements for DS Tau were carried out by using HST/STIS spectra. As the continuum level, we took the fitting curve obtained above; we determined the flux in the C IV 1550 doublet lines from the spectral region shown in Fig. 3. For DG Tau, the continuum flux in the range 2275–3000 Å, where

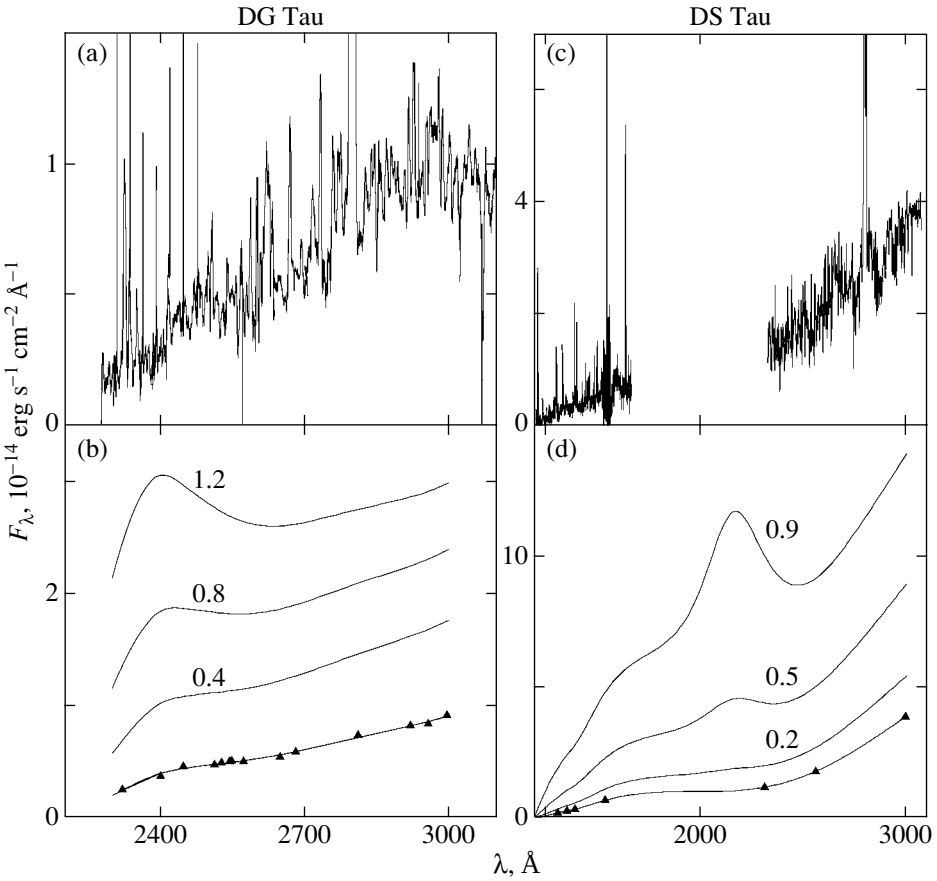

Fig. 1. The UV spectra of DG Tau and DS Tau: (a and c) the observed spectra and (b and d) the continuum energy distributions corrected for interstellar extinction with different values of A_V. In the case of DG Tau, the curves with $A_V = 0^m.8$ and $1^m.2$ were compressed along the y axis by factors of 1.4 and 2.2, respectively, for clarity. The spectral flux density is along the y axis. The triangles indicate the continuum level determined directly from the spectra.

the bulk of the UV radiation from the star is concentrated, was also determined from HST/STIS spectra. However, since no observations were made from the Hubble Space Telescope in the wavelength range $\lambda < 2275$ Å, we took the flux in the C IV 1550 doublet lines from Valenti *et al.* (2000), who gave the flux averaged over three IUE spectra.

Our results are presented in Table 2. All fluxes were corrected for interstellar extinction with the A_V values given in the table; they are in units of 10^{-10} and 10^{-13} erg cm^{-2} s^{-1} for the continuum and the lines, respectively. We see that even the ratio $\xi_{UV} = F_{\rm CIV}/F_{UV}$ is slightly lower than that predicted by theory and is virtually independent of the existing uncertainty in A_V. It can be shown that ξ_{UV} also weakly depends on the chosen extinction law.

Since the theory uses the bolometric luminosity of the emission continuum, the ratio $\xi = F_{\rm CIV}/F_{\rm ac}$ must be even smaller than ξ_{UV}. To determine precisely how much smaller it is, let us estimate the total accretion luminosities of DG Tau and DS Tau.

DS Tau. Figure 4 shows the spectral energy distribution for this star constructed from its mean U, B, V, $R_{\rm c}$, $I_{\rm c}$, K, and L magnitudes (Kenyon and Hartmann 1995) and from our UV data. All fluxes were corrected for interstellar extinction with $A_V = 0^m.5$. This distribution is the superposition of the radiation from the star itself and the accretion radiation. A lower limit for the accretion luminosity can be estimated by fitting the theoretical energy distribution of a K5-type subgiant (Pickles 1998) indicated by the heavy line in Fig. 4 to the observed continuum. The

Table 2. UV fluxes

Star	A_V	$F_{-13}^{\rm CIV}$	$F_{-10}^{\rm c,UV}$	ξ_{UV}
DG Tau	0.8	3.4	0.2	0.017
	1.4	14	0.93	0.015
DS Tau	0.5	12	0.74	0.016
	0.9	30	2.1	0.014

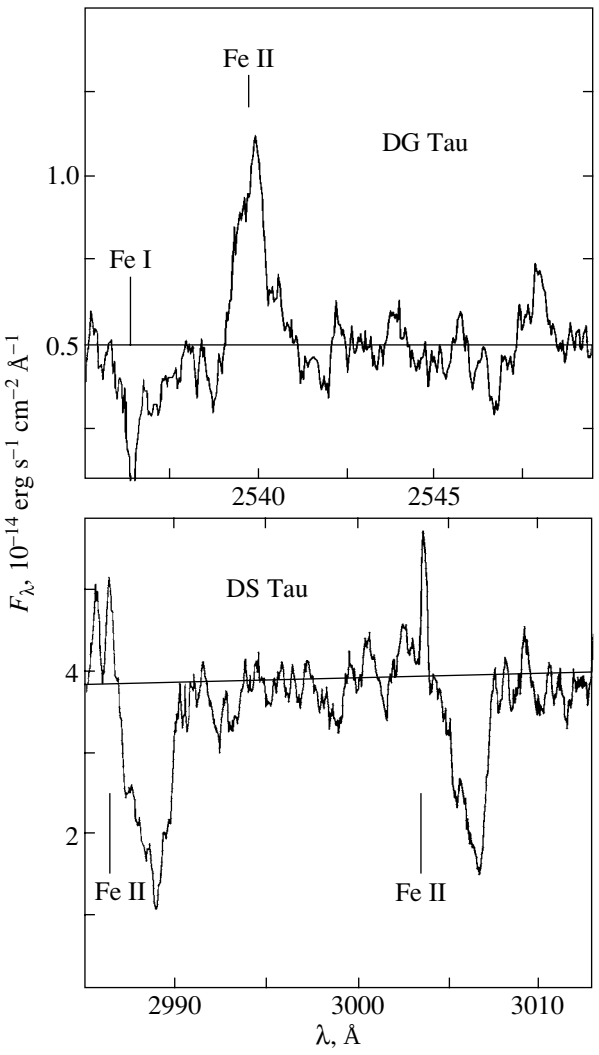

Fig. 2. Examples of the spectral regions for DS Tau and DG Tau in which the continuum level was determined.

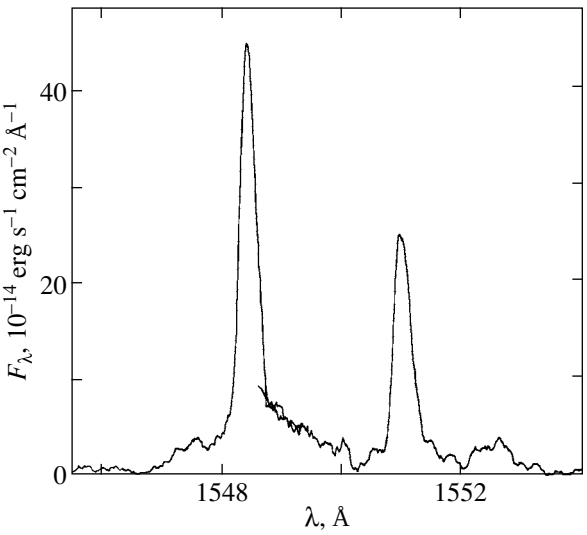

Fig. 3. The spectral regions of DS Tau near the C IV 1550 doublet lines.

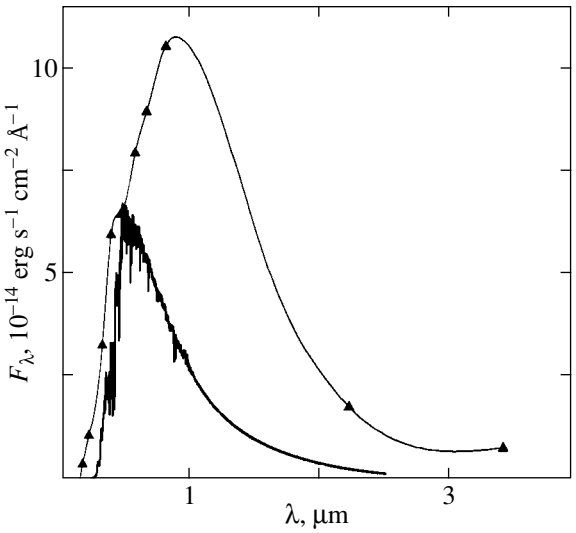

Fig. 4. The spectral energy distribution of DS Tau corrected for interstellar extinction with $A_V = 0\overset{m}{.}5$. The wavelength in μm is along the x axis and the spectral flux density in 10^{-14} erg cm^{-2} s^{-1} is along the y axis. The heavy line represents the spectral energy distribution for a K5-type subgiant.

difference between the total and fitted energy distributions gives a lower limit for the accretion luminosity of DS Tau.

The accretion flux from DS Tau determined in this way is 9.7×10^{-10} erg cm^{-2} s^{-1}, which corresponds to $\xi \simeq 2 \times 10^{-3}$. If $0\overset{m}{.}9$ (White and Ghez 2001) is taken as A_V, then ξ will only increase by a factor of 1.5; if the spectral type of the star is assumed to be K5 V rather than K5 IV, then ξ will also increase, but only by 25%. On the other hand, recall that the F_{ac} value obtained above is only a lower limit. Therefore, the actual value of ξ for DS Tau must be lower.

DG Tau. The emission continuum of this star is so strong that almost no photospheric lines can be seen in its spectrum (Hessman and Guenter 1997). Therefore, we can assume that virtually the entire observed luminosity of DG Tau is attributable to accretion, while the contribution of the radiation from the star itself is negligible. White and Ghez (2001) calculated the bolometric luminosity of DG Tau by assuming that $A_V = 1\overset{m}{.}4$. In order that our ξ estimate be self-consistent, we took the flux in the C IV 1550 doublet lines obtained with the same A_V from Table 2. Since the distance to the star is 140 pc, $F_{ac} = 2 \times 10^{-9}$ erg cm^{-2} s^{-1} and ξ is equal to 7×10^{-4}.

According to our data, A_V for DG Tau does not exceed $0\overset{m}{.}8$. It can be easily seen that decreasing A_V will result in even smaller ξ because, as in the case of

DS Tau, the bulk of the stellar luminosity is emitted in the infrared.

DISCUSSION

We found that the ratio ξ of the luminosity in the C IV 1550 doublet lines to the bolometric luminosity of the emission continuum is $\sim$0.2 and $\sim$0.07% for DS Tau and DG Tau, respectively. At the same time, theory predicts that ξ must be more than $\sim$2% if the entire emission continuum originates in the AS. Consequently, there is also a powerful source of continuum in these stars. It cannot be explained by the radiation from the disk, because the latter cannot emit more than half of the total accretion luminosity (Lipunov 1989). Hence, accretion onto the star proceeds not only through the magnetosphere and the AS but also through the disk, which touches the stellar surface. Thus, the low value of ξ implies that the bulk of the matter falls to the star in the equatorial plane and the emission continuum originates mainly in the boundary layer.

It turns out that a similar conclusion can also be reached for TW Hya. According to Batalha *et al.* (2002), the accretion rate onto the surface of TW Hya is $\simeq 3\times10^{-9}M_\odot$ yr^{-1} and the gas infall velocity is $V = 300$ km s^{-1}. These data allow us to estimate the accretion luminosity of the star, $L_{\rm ac} = \dot{M}V^2/2$, and the bolometric flux near the Earth by assuming that the distance to TW Hya is 50 pc (Soderblom *et al.* 1998). The C IV line flux from TW Hya is 1.2×10^{-12} erg cm^{-2} s^{-1} (Valenti *et al.* 2000) and $A_V = 0.1\pm0.1$ (Batalha *et al.* 2002). We infer from these data that $\xi \simeq 10^{-3}$ for $A_V = 0$ and approximately twice as large for $A_V = 0.3$. Thus, we again obtain a value that is an order of magnitude lower than the theoretical value. Therefore, the magnetic field of TW Hya does not hold the disk, although the accretion rate in this case is two orders of magnitude lower than, for example, that for DR Tau (Kravtsova and Lamzin 2002a).

CONCLUSIONS

Having analyzed the UV spectra, we obtained an upper limit of the interstellar extinction A_V for the young stars DS Tau and DG Tau. These values proved to be lower than those inferred by White and Ghez (2001) from optical observations. Previously, Kravtsova and Lamzin (2002a, 2002b) found a similar discrepancy for nine more T Tauri stars. The cause of this effect requires special investigation.

We also found that the ratio of the flux in the C IV doublet lines to the emission continuum flux for the stars DS Tau, DG Tau, and TW Hya is at least an order of magnitude smaller than that predicted by theory. Such a discrepancy also takes place for the stars DR Tau, T Tau, and RY Tau (Kravtsova and Lamzin 2002a, 2002b). Thus, in all six stars, which were actually chosen at random, accretion proceeds mainly not through the magnetosphere but through the disk into the equatorial region of the star. In other words, the disk is not halted by the star's magnetic field and reaches its surface even in the case of TW Hya with a low accretion rate. This conclusion may imply that a similar situation takes place in most young stars.

ACKNOWLEDGMENTS

I am grateful to S.A. Lamzin for a discussion and to the referees for helpful remarks. This work was supported by the Russian Foundation for Basic Research (project no. 02-02-16070), as was the study of Kravtsova and Lamzin (2002b)—this circumstance was not noted in the latter paper by our negligence.

REFERENCES

1. C. Batalha, N. M. Batalha, S. H. P. Alencar, *et al.*, Astrophys. J. **580**, 343 (2002).
2. R. C. Bless and B. D. Savage, Astrophys. J. **171**, 293 (1972).
3. N. Calvet and E. Gullbring, Astrophys. J. **509**, 802 (1998).
4. F. V. Hessman and E. W. Guenter, Astron. Astrophys. **321**, 497 (1997).
5. S. J. Kenyon and L. Hartmann, Astrophys. J. Suppl. Ser. **101**, 117 (1995).
6. A. S. Kravtsova and S. A. Lamzin, Pis'ma Astron. Zh. **28**, 748 (2002a) [Astron. Lett. **28**, 676 (2002a)].
7. A. S. Kravtsova and S. A. Lamzin, Pis'ma Astron. Zh. **28**, 928 (2002b) [Astron. Lett. **28**, 835 (2002b)].
8. S. A. Lamzin, Astron. Zh. **75**, 367 (1998) [Astron. Rep. **42**, 322 (1998)].
9. S. A. Lamzin, Astron. Zh. **80** (2003, in press) [Astron. Rep. **47** (2003, in press)].
10. V. M. Lipunov, *Astrophysics of Neutron Stars* (Nauka, Moscow, 1989).
11. J. Najita, S. Edwards, G. Basri, and J. Carr, *Protostars and Planets IV*, Ed. by V. Manningc, A. P. Boss, and S. S. Russel (Arizona Univers. Press, 2000), p. 457.
12. A. J. Pickles, Publ. Astron. Soc. Pac. **110**, 863 (1998).
13. M. J. Seaton, Mon. Not. R. Astron. Soc. **187**, 75 (1979).
14. D. R. Soderblom, J. R. King, L. Siess, *et al.*, Astrophys. J. **498**, 385 (1998).
15. J. A. Valenti, C. M. Johns-Krull, and J. L. Linsky, Astrophys. J., Suppl. Ser. **129**, 399 (2000).
16. R. J. White and A. M. Ghez, Astrophys. J. **556**, 265 (2001).

Translated by A. Dambis

Astronomy Letters, Vol. 29, No. 7, 2003, pp. 468–479. Translated from Pis'ma v Astronomicheskiĭ Zhurnal, Vol. 29, No. 7, 2003, pp. 532–544.

An Electronic Version of the Second Volume of the General Catalogue of Variable Stars with Improved Coordinates

N. N. Samus'[1,2*], V. P. Goranskii[2], O. V. Durlevich[2], A. V. Zharova[2], E. V. Kazarovets[1], N. N. Kireeva[1], E. N. Pastukhova[1], D. B. Williams[3], and M. L. Hazen[4]

[1] *Institute of Astronomy, Russian Academy of Sciences, ul. Pyatnitskaya 48, Moscow, 119017 Russia*

[2] *Sternberg Astronomical Institute, Universitetskii pr. 13, Moscow, 119992 Russia*

[3] *American Association of Variable Star Observers, 25 Birch St., Cambridge, MA 02138-1205, USA*

[4] *Harvard Observatory, 60 Garden St., Cambridge, MA 02138 USA*

Received February 5, 2003

Abstract—We present a new electronic version of the second volume of the fourth edition of the General Catalogue of Variable Stars (GCVS), which contains data on 13 480 variable stars in the constellations Cygnus–Orion (the order of constellations in the Catalogue follows the Latin alphabet). The new version takes into account the Name Lists of Variable Stars from no. 67 to 76 for the same constellations. The main distinctive feature of the new version is that it contains improved equatorial J2000.0 coordinates for 13 446 stars (including those for 5052 stars with an allowance made for proper motions), based on the identifications with positional catalogs using finding charts, as well as on our new measurements. We searched for a number of stars on original plates from the collections of several observatories and using digital sky survey images. The new version also includes a file of remarks to the second and third GCVS volumes. Apart from a complete update of the positional information, we took into account several corrections that were found to be necessary after the publication of the second GCVS volume (1985). We present a list of references to new Internet resources. © *2003 MAIK "Nauka/Interperiodica"*.

Key words: *stars—variable and peculiar.*

INTRODUCTION

This paper is a continuation of our previous publication on the new electronic version of Volume I of the General Catalogue of Variable Stars (GCVS) with improved coordinates (Samus' *et al.* 2002) and presents a similar version for Volume II of the GCVS.

The new electronic version is based on the fourth edition of the GCVS (Kholopov *et al.* 1985–1988). Volumes I–III of the latter contain data on 28 435 variable stars of our Galaxy (without including the named variables that proved to be nonexistent, e.g., minor planets mistaken for stars, artifacts due to double plate exposures, etc.). Given the subsequent ten Name Lists of Variable Stars (nos. 67 to 76), the number of Galactic variables named in 2001 exceeded 37 300. The standard accuracy of the variable star coordinates presented in the GCVS (to within 1 s in right ascension and 0.1 arcmin in declination, with a substantial fraction of all GCVS stars having even less accurate coordinates than the standard accuracy or just erroneous coordinates) does not meet the present-day requirements that were formulated in more detail by Samus' *et al.* (2002). Therefore, we decided to prepare a new GCVS version with improved coordinates for all of the catalogued stars, where possible, which also takes into account the proper motions of the stars if they can be found in existing positional catalogs.

METHODS FOR PREPARING THE CATALOGUE

The methods for preparing the Catalogue were described in detail by Samus' *et al.* (2002). In general, they did not change. In the past year, the possibilities for the effective identification of variable stars with positional catalogs have further improved. Apart from the sources listed in Samus' *et al.* (2002), we actively used several new catalogs in our work on the new version of the GCVS Volume II: the US Naval Observatory CCD Astrograph Catalog (Zacharias *et al.* 2000), which contains more than 27 000 000 stars; the 2.2 μm LMASS All Sky Survey (Skrutskie *et al.* 2000), whose current version covers almost half of the sky area and includes more than 162 000 000 stars; and the Guide Star Catalogue, version 2.2 (STScI 2001), which includes more than 435 000 000

*E-mail: samus@sai.msu.ru

stars. Unfortunately, in most cases where the UCAC1 catalogue could be the only source of a variable star's proper motion, the errors in the catalogued proper motions were too large, so we could not make use of such proper-motion information. By the end of our work on the new version of Volume II, we gained access to the B1.0 Catalog of the US Naval Observatory (Monet *et al.* 2003), which contains more than 1 000 000 000 objects; so far, we have used it only in a few cases.

As before, our main tool for visualizing astronomical catalogs and retrieving data from them was the SIMFOV code written by A.A. Volchkov (A. Volchkov and O. Volchkov 2003). During our work on the electronic version of the GCVS Volume II, changes were made to the code, which allowed us to use also the 2MASS and UCAC1 catalogues for our identifications. Recall that this code makes it possible to display a chart of the selected sky field on the required scale, which shows objects of the catalogs from the selected list, and then view it by zooming in and out and retrieve information in the corresponding catalog pertaining to any image. The same code enables the automatic identification of user lists with catalogs by coordinates with (or without) an allowance for the similarity of the magnitudes. Viewing images, retrieving information, and comparing lists are possible for the coordinates referred to any equinox. Thanks to the database on variable stars supported by the GCVS team, we have at our disposal the most complete information about the published finding charts for variables; unpublished charts for several thousand stars were provided by their discoverers and other researchers. In particular, the photographic finding charts for hundreds of stars in the constellations Libra and Ophiuchus sent to the GCVS team in the 1960s by the discoverer of their variability, Dr. L. Plaut (the Netherlands), helped us immensely in preparing the new version of the GCVS Volume II.

The numerous publications that appeared in recent years and that contain identifications and accurate coordinates of variable stars from selected lists (see, e.g., López and Girard 1990; Kato 1999a, 1999b; Skiff 1999a, 1999b, 1999c; Kinnunen and Skiff 2000a, 2000b, 2000c; López and Lépez 2000; Webbink *et al.* 2002) were very helpful in checking our results. However, we identified all of the stars from these papers independently; we found a number of mistakes both in our original identifications and in some of the cited papers. Examples of the mistakes found in these publications are described below in the remarks on individual stars.

In several cases, especially in very crowded star fields, it was difficult to identify the computer-displayed chart showing objects of a catalog(s) with the variable star's published drawn or photographed finding chart. In such situations, we examined images of the Digitized Sky Survey (DSS; the Hubble Space Telescope Science Institute) or images from the Aladin Sky Atlas (the Strasbourg Astronomical Data Center,) and the US Naval Observatory Image and Catalog Archive. These archives contain several images of the same field, which often makes it possible to rediscover a variable star without examining plate stacks. However, if necessary, we used the plate collections of the Sternberg Astronomical Institute and the Harvard Observatory and rediscovered the variable stars that were "lost" because of the absence of finding charts and inaccurate coordinates. We widely used the marks of the discoverers on the plates of the Harvard stacks and the discoverers' notebooks in the Harvard archive (among some 13 000 variable stars discovered at the Harvard Observatory, about 3000 objects have no published finding charts).

If a variable star was absent in the existing positional catalogs, then we measured the coordinates on original plates or available digitized sky images. This was also often done to determine the coordinates for the variable components of visual double stars or the coordinates of variable stars in clusters.

Specific problems were associated with variable stars in nebulae. Whereas solving these problems for numerous stars in nebulae in Monoceros actually reduced to measuring the coordinates for an unusually large fraction of variables in this constellation using DSS images, the images of the DSS and other similar surveys for the region of the Orion Nebula, which is even richer in variable stars, are often overexposed and do not allow the identification of stars.

Jones and Walker (1988) presented photographic *I*-band charts and coordinates for 1053 variable stars in the central part of the Orion Nebula; in the absence of a particular star in the positional catalogues, we used the coordinates measured by these authors. Immediately after the publication of the paper by Jones and Walker (1988), the GCVS authors meticulously compared the photographic charts of Jones and Walker with the available charts of variable stars in the Orion Nebula. As a result, we compiled a table of identifications of the objects from the list of Jones and Walker with known variable stars, which is still used by the GCVS team. We have now opened electronic access to this table, along with other our tables of identifications of variable stars (ftp://ftp.zeus.sai.msu.ru/pub/groups/cluster/gcvs/gcvs/iv). Identifications using the tables at this address are provided to users of the GCVS electronic version when they request information on any variable star via the search engine of our site (http://www.sai.msu.su/groups/cluster/gcvs/cgi-bin/search_new.html).

Table 1. Corrected data for the variable stars in Orion discovered by Maffei (1963)

No. in Maffei's chart	GCVS	Max	Min	Type
25	V796 Ori	15.5	16.4 I	IN
26	V798 Ori	15.2	17.2 P	INS
27	V802 Ori	15.6	18.0 B	UVN
28	V810 Ori	15.5	16.5 I	IN
29	V811 Ori	15.8	16.8 I	IN
30	V814 Ori	15.5	17.3 B	IN
31	V819 Ori	15.6	17.4 P	IN
32	V832 Ori	14.5	16.6 P	INS
33	V838 Ori	16.6	17.3 P	IN

Initially, we took the positions of 163 variables in the Orion Nebula from the list of Jones and Walker (1988) and independently measured the coordinates for 70 other variable stars in this region. Subsequently, we were able to identify 80% of these stars absent in the positional catalogs that we used with the 2MASS catalogue (Skrutskie *et al.* 2000); the identifications were checked by using the J, H, and K images of the 2MASS survey provided by the Aladin Star Atlas.

We also encountered great difficulties in identifying the nine Orion variables discovered by Maffei (1963). In the 1960s, when compiling another Name-List of Variable Stars, P.N. Kholopov noticed that the coordinates of these variables (nos. 25–33 in Table IV from Maffei 1963) published by the discoverer disagreed with the chart presented by this author. According to the GCVS tradition of considering a finding chart as a major tool for identifying variable stars, it was then decided to correct the coordinates in accordance with the chart; all of the other information in each row of the table was taken without any changes. When preparing our new version of the GCVS Volume II, we found that such a correction of the discoverer's table leads to incorrect information about the variability ranges and types, while the remarks to Table IV refer to the correct stars. We have decided not to change the now traditional correspondence between the GCVS names of these stars and their numbers in the chart and in the remarks published by Maffei. Table 1 presents corrected data on the variability ranges and types for the stars of this list. The notation is standard for the GCVS.

Previously (Samus' *et al.* 2002), we noted our cautious attitude toward the charts from the atlas of Tsesevich and Kazanasmas (1971), which, in general, is helpful and, in many cases, the only available tool for identifying variable stars. In compiling the new version of the GCVS Volume II, we again found numerous mistakes in this atlas. Particularly many mistakes were found for variables in Norma. Thus, for example, five of the 12 charts (for BF, CG, CI, CT, and DE Nor) on sheet IV-28 of the atlas alone proved to be erroneous; besides, the chart for AX Nor on the same sheet is upside down.

During our work, we found dozens of omissions in the tables of identifications of variable stars with the principal catalogs (BD, CoD, CPD, HD, etc.) in the GCVS Volume IV. We made appropriate changes to the electronic version of the catalogue. After finishing the preparation of the electronic version of the catalogue, we checked it through its automatic (by coordinates) identification with the GSC; as a result, we revealed and corrected several errors.

RESULTS

The electronic version of Volume II is available at ftp.zeus.sai.msu.ru/pub/groups/cluster/gcvs/gcvs/vol2/ or www.sai.msu.su/groups/cluster/gcvs/gcvs/vol2/.

The new electronic version of the GCVS Volume II contains, in its main table (vol2.dat), information about 13 480 objects (except for the stars that were erroneously named for the second time or proven to be nonexistent) in the constellations Cygnus–Orion, which are mostly variable stars of our Galaxy discovered and named before 2001; i.e., it covers the variable stars of the fourth edition of the GCVS and the Name-Lists nos. 67–76 (for the same constellations). For 13 446 variable stars, our version presents new equatorial J2000.0 coordinates (vol2_pos.dat); proper motions are taken into account for 5052 of these stars. We have not yet been able to determine accurate coordinates for 34 variable stars because of the absence of finding charts or the lack of information for star identification. Recall that the new version of the GCVS Volume I (Samus' *et al.* 2002) did not present accurate coordinates for 209 of the 10 558 stars; given that this version was continuously corrected, the number of GCVS Volume I stars without accurate coordinates reduced to 182 by the end of 2002. The main table is supplemented with a list of remarks to Volumes II and III (rem.txt), which has been published electronically for the first time. A detailed description of the files can be found in the file readme.txt of the electronic version.

The vol2.dat *File*

The structure of the main table (vol2.dat) corresponds to the structure of the combined table in the 4th GCVS edition and the Name Lists (Kholopov *et al.* 1998; see also www.sai.msu.su/groups/cluster/gcvs/gcvs/iii/iii.dat). The differences between these tables were described in detail by Samus' *et al.* (2002); here, we repeat this information for the convenience of users.

(1) Instead of the B1950.0 coordinates, we present new improved equatorial J2000.0 coordinates (right ascensions to within $0^s.1$ and declinations to within $1''$). The coordinates that could not be improved were recalculated to the equinox J2000.0 from old rough coordinates by taking precession into account.

(2) The latest Name Lists, up to no. 76, were included.

(3) We rectified the serious mistakes that were found during our work on the GCVS in other columns of the main table, in the references, and in the remarks. For the stars without published finding charts but identified by us in the GSC (Lasker *et al.* 1990), GSC2.2, or US Naval Observatory (USNO) A1.0/A2.0/B1.0 catalogs, we now give the symbol of the corresponding catalog (GSC, GSC2.2, USNO) as a reference to the finding chart.

The main table is presented in the standard (for the GCVS) form, i.e., in the order of constellations and GCVS variable-star names. The table includes the following information: J2000.0 equatorial coordinates, variability types, magnitudes at maximum and minimum light, photometric systems of magnitudes, epochs of minima or maxima, periods of brightness variations, durations of brightness rise from minimum to maximum or eclipse durations, spectral types, and references. For the stars from the Name List nos. 67–76, which appeared after the publication of the GCVS 4th edition, we present not all of the columns of the table but only the coordinates, variability types, magnitudes, and references; the missing data will be added to the 5th edition of the GCVS.

The vol2_pos.dat *File*

The positional information based on our identifications with principal astrometric catalogs, on published data, or on our new measurements (see below) is provided for 13 446 variable stars of the new version of Volume II (including stars of the new Name Lists in the same constellations) in the table vol2_pos.dat. This table is presented in the same order as the main table and consists of the following columns:

(1) The star number in the system traditional for the electronic GCVS versions;

(2) The GCVS star name;

(3) Improved equatorial J2000.0 coordinates (right ascensions to within $0^s.01$ and declinations to within $0''.1$);

(4) A flag indicating that the coordinates are actually rougher than the new accuracy standard of the catalogue, because we were unable to determine more accurate coordinates and find them in source catalogs or journal publications. The flag is a colon (:) in the position that follows the coordinates;

(5) Proper motions (in arcseconds per year for both coordinates), to within $0''.001$ per year;

(6) The epoch of the given coordinates. No epoch is presented when published coordinates are used unless it was specified in the paper and could be established;

(7) A flag indicating uncertainty in a variable star's identification with the corresponding source catalog (a question mark in the corresponding position);

(8) A brief designation of the source of astrometric data. In several cases, the designation of a catalog is followed by the symbol "+pm," implying that this catalog contains the position for a certain epoch that we reduced to the epoch 2000.0 using information about the star's proper motion from another source.

Below, we provide a list of principal catalogs and data sources approximately in the order of our preference during the identifications of variable stars (see also a description of the catalogs for A.A. Volchkov's SIMFOV visualization code that we used at the site www.simfov.ru). Note that most of the deviations from this order of preference stem from the fact that the SIMFOV code does not yet work with the GSC2.2, FASTT, and USNO B1.0 catalogs. In fact, we considered the coordinates from several positional catalogs based on the plates of Schmidt surveys or catalogs of comparable accuracy as being equal in value.

Hip is the Hipparcos Catalogue (ESA 1997).

Tyc2 is the Tycho Catalogue (Høg *et al.* 2000). In the only case in Volume II (V2238 Cyg) where the star was absent in the second Tycho catalogue but present in the first catalogue (ESA 1997), the source is indicated as Tyc1.

PPM is the Positions and Proper Motions (Röser *et al.* 1991–1993).

NPM is the Lick Northern Proper Motion Program (Klemola *et al.* 1987).

AC is the Four-Million Star Catalogue (see Gulyaev and Nesterov 1992).

ACT is the ACT Reference Catalog (Urban *et al.* 1997).

FASTT lists the coordinates of variable stars (in the equatorial region of the sky) measured with the Flagstaff Astrometric Scanning Transit Telescope of the US Naval Observatory (Henden and Stone 1998).

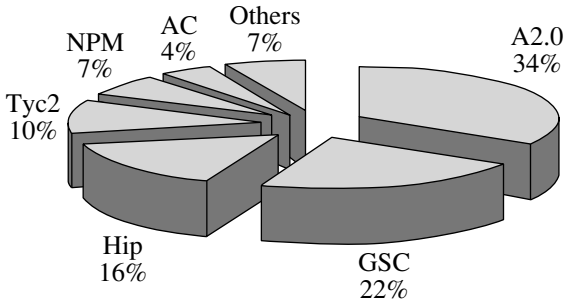

The sector diagram illustrating the distribution of stars from the new version of the GCVS Volume II in the sources of accurate coordinates.

GSC2.2 is the Guide Star Catalogue, Version 2.2 (STScI, 2001).

UCAC1 is US Naval Observatory CCD Astrograph Catalog (Zacharias *et al.* 2000).

GSC is the Guide Star Catalog (Lasker *et al.* 1990). The symbol "ns" that accompanies the GSC reference means that the object is marked in the cited catalogue as nonstellar.

A2.0, B1.0 is a Catalog of Astrometric Standards (Monet *et al.* 1998) (there are a few cases where the star could be found only in the previous version of the catalog; they are marked as A1.0); The Whole-Sky USNO-B1.0 Catalog of 1 045 913 669 Sources (Monet *et al.* 2003).

2MASS is the Two Micron All Sky Survey (Skrutskie *et al.* 2000).

IRAS is the Infrared Astronomical Satellite Catalogue of Point Sources (Neugebauer *et al.* 1988). We used this catalogue only when it was impossible to identify a star with a positional catalog or to find a star in the optical range and independently measure its coordinates. There is only one such case in Volume II (V2294 Oph).

For some 330 stars (2.5% of all of the stars in the new version), we measured the coordinates using Digitized Sky Survey images, plates from different collections, or other images. In these case, the source of the coordinates is indicated as "GCVS authors." As a rule, we employed the GSC2.2 or A2.0 catalogue stars as reference stars in our measurements using the Digitized Sky Survey. To measure the rectangular coordinates, we manually pointed the cursor at the photometric centers of stars in commercially available image processing applications with a high magnification. The measurements were reduced by Turner's linear method. The accuracy of our measurements was typically about $0''.5$ both in right ascension and declination. The coordinates taken from current astronomical periodicals are marked "Literature."

We present a fragment (the first 20 stars) of the table vol2_pos.dat as a guide to its contents (Table 2).

The distribution of stars from the new version of the GCVS Volume II in the sources of their coordinates is shown in the figure; the GCVS authors and Literature sources as well as some rarely used catalogs were combined into a sector called "Others."

The rem.txt *File*

The list of remarks for Volumes II and III (rem.txt) includes information that supplements the main table for 6362 stars. In contrast to the printed bilingual version of the 4th GCVS edition (Kholopov *et al.* 1985–1988), all remarks in the file are given only in English; in general, they correspond to the English text of remarks in the printed edition or to the remarks from the Name Lists. The remarks provide, in particular, information about variables in binaries, period variations, the secondary minima of eclipsing variables, and a star's proximity on the sky to star clusters or nebulae. The remarks for unique variable stars contain detailed descriptions of the variability pattern.

COMMENTS ON SOME PROBLEM STARS OF THE ELECTRONIC VERSION

Below, we give comments on individual stars of the GCVS Volume II. We did not set the goal of listing here all of the complex cases that we encountered during our work on the catalogue. It seems that the examples collected below give a good idea of the typical problems the compilers of the catalogue have to solve. The coordinates and identifications adopted for the stars described in the comments are presented in Table 3.

IY Gem. The previous attempt to identify this star using its finding chart (Skiff 1999c) failed.

KN Gem. After we reported (Samus 2001) that the classification of this object as a Mira variable resulted from its misidentification (actually, the Mira is the neighboring variable BR Gem), it was identified with the minor planet (123) Brunhild (Schmeer 2002). This object was not included in Table 3.

VW Gru. López and Lépez (2000) misidentified this Mira star. The variable is absent in positional catalogs, because it is close in the sky to the very bright star HD 213009.

V403 Her – V405 Her. Our reliable identifications of these three RR Lyrae variables differ from those suggested by Skiff (1999b).

ZZ Hyi. We identified this object, which was previously classified as a likely RR Lyrae variable (Geßner 1981a), with the poorly studied galaxy PGC 232232 (Pastukhova 2001).

Table 2. A fragment of the electronic table vol2_pos.dat

GCVS			J2000.0		pm (as/yr)		Epoch	Source
310001	R	Cyg	193649.38	+501159.5	+0.003	−0.009	2000.0	PPM
310002	S	Cyg	200529.85	+575909.5			1952.617	A2.0
310003	T	Cyg	204710.75	+342226.8	+0.039	+0.008	2000.0	Hip
310004	U	Cyg	201936.59	+475339.1	−0.002	+0.001	2000.0	Hip
310005	V	Cyg	204118.27	+480828.8	−0.006	−0.013	2000.0	Hip
310006	W	Cyg	213602.49	+452228.5	+0.064	+0.002	2000.0	Hip
310007	X	Cyg	204324.19	+353516.1	−0.006	−0.003	2000.0	Hip
310008	Y	Cyg	205203.58	+343927.5	+0.003	−0.017	2000.0	Hip
310009	Z	Cyg	200127.46	+500232.6			1983.449	GSC
310010	RR	Cyg	204604.56	+445209.7	+0.001	−0.001	2000.0	Tyc2
310011	RS	Cyg	201323.66	+384344.5	+0.008	+0.002	2000.0	Hip
310012	RT	Cyg	194337.77	+484641.3	−0.009	+0.014	2000.0	Hip
310013	RU	Cyg	214039.09	+541928.9	−0.008	−0.012	2000.0	Hip
310014	RV	Cyg	214316.33	+380103.0	−0.006	−0.008	2000.0	Hip
310015	RW	Cyg	202850.59	+395854.4	−0.003	−0.006	2000.0	Hip
310016	RX	Cyg	201049.59	+474847.2	−0.004	−0.002	2000.0	Hip
310017	RY	Cyg	201023.42	+355649.4	+0.003	+0.001	2000.0	Tyc2
310018	RZ	Cyg	205153.19	+472120.4	−0.000	−0.002	2000.0	AC
310019	SS	Cyg	214242.79	+433509.9	+0.107	+0.030	2000.0	Tyc2
310020	ST	Cyg	203233.48	+545700.5	−0.011	−0.001	2000.0	Tyc2

DM Lac and HQ Lac. Miller and Wachmann (1971) give accurate coordinates for these two stars, but the designations in their charts were mixed up. We adopted the identification based on the coordinates rather than the charts; it is also confirmed by the fact that the number of comparison stars presented by Miller and Wachmann in their table for DM Lac corresponds to their chart for HQ Lac, and vice versa.

EG Lac. As was noted by Kinnunen and Skiff (2000c), Downes and Shara (1993) gave the wrong chart. The object that was classified as a UGSS dwarf nova is bright on the infrared plates of the second Palomar survey (epochs 1993.6003 and especially 1993.7070). Thus, its classification should be refined. Appropriate changes based on our information have presently been made to the catalog of Downes *et al.* (2003).

EU Lac. The chart of Miller and Wachmann (1971) is wrong, but it was possible to make the identification using other published charts and the sufficiently accurate coordinates given by Miller and Wachmann.

IS Lac and PU Lac. The variability of IS Lac was discovered by Miller and Wachmann (1971), who pointed out the star's very red color. The discoverers provide the star's coordinates with a high formal accuracy. There are no red stars at this position, and the chart of Miller and Wachmann corresponds to the carbon variable star PU Vul discovered by Alksne and Alksnis (1972), which lies more than 8′ to the south. In our new GCVS version, we declare that these two stars are identical, retaining PU Lac as the main designation. We were able to find IS Lac thanks to the notes left by the late A.P. Gulyaev (Sternberg Astronomical Institute).

EN Lib and GT Lib. The variability of GT Lib was first announced by Lampland (1914). The star was included in the GCVS based on data of Luyten (1937), who reported its independent discovery and large variability amplitude. Hoffmeister (1949) found the Mira variable EN Lib whose coordinates differed from the adopted position of GT Lib by 3′.5. The identity of Luyten's star and EN Lib was confirmed by our searches in the Harvard Observatory archives.

Although, strictly speaking, it is not known what star was observed by Lampland, we declared that these two stars are identical in the new GCVS version.

EX Lib. This star was identified using the unpublished chart of L. Plaut. The coordinates of this star in our paper (Antipin *et al.* 1994a) on the positions of variable stars in Plaut's field 1 (Plaut 1966) are erroneous by 1^m in right ascension because of a misprint.

AZ Lup. The star could be identified using its correct chart from Tsesevich and Kazanasmas (1971) only after our search in the Harvard Observatory archives that revealed an error of 3° in declination in the coordinates published by the discoverers (Swope and Caldwell 1930). The star lies north of their position.

DY Lup and DZ Lup. These two variable stars were discovered by Hoffleit (1936). She indicated a large (about 3^m) variability amplitude for the first star (HV 7442) and a comparatively small ($0\overset{m}{.}4$) amplitude for the second star. Subsequently, McLeod and Swope (1941) pointed out that HV 7441 was a Mira variable with a variability amplitude of larger than $3\overset{m}{.}5$ and a period of 434^d. The atlas of Tsesevich and Kazanasmas (1971) contains charts for both stars. Using the Harvard Observatory archives, we found that Hoffleit erroneously gave the coordinates of the low-amplitude variable for the Mira star and vice versa. We retained the traditional name DY Lup for the Mira variable and the name DZ Lup for the lower-amplitude variable. It turns out for these identifications that the chart for the bona fide DY Lup is labeled DZ Lup in the atlas of Tsesevich and Kazanasmas (1971). The chart labeled DY Lup is incorrect for both of these two variables.

BV Lyr. Several existing charts do not confirm the identification by Skiff (1999a).

V369 Lyr. We found and measured this possible Nova discovered by Kurochkin (1968) on the original plates of the Sternberg Institute's stacks.

V408 Lyr. The discoverer, Kurochkin (1971), published erroneous coordinates. The star was found on the Sternberg Institute's plates using the marks of N.E. Kurochkin on the plates.

V479 Lyr and V480 Lyr. In the report on the discovery of these two stars (S 10845 and S 10846) (Geßner 1981b), preliminary numbers in the Sonneberg Observatory system were assigned to them and to one more object in order of increasing right ascensions. The chart for S 10845 corresponds to the coordinates for S 10846 and vice versa. We retained the traditional names V479 Lyr (according to Geßner (1983), this is a reddish slow irregular variable fainter in photographic light than V480 Lyr) and V480 Lyr (Geßner (1983) believes it to be a possible β Lyrae variable with a period of about 100^d) in order of their right ascension. This identification is supported by the magnitudes in positional catalogs. According to the ROTSE1 catalogue (Akerlof *et al.* 2000), the star at the position that we adopted for V480 Lyr is a Cepheid with a period of $44\overset{d}{.}5$, which also most likely argues for our identification. Note, however, that Geßner (1983) mentions a faint companion to V479 Lyr, while our identification suggest a faint companion to V480 Lyr.

UW Men. Our quite reliable identification differs from that suggested by López and Girard (1990).

V567 Mon. It was identified reliably. Kato (1999b) identified this variable with another star in the same group of faint objects.

RV Mus and FI Mus. By the suggestion of A.P. Gulyaev, we assume that the Mira star FI Mus, which was identified using the chart of Goossens *et al.* (1980) who announced its discovery, is identical to the Mira RV Mus discovered by Bailey (1923) much earlier. For the latter star, its discoverer gave coordinates that were virtually identical to the accurate coordinates of FI Mus and a possible period that did not differ too much from the period found by Goossens *et al.* but did not publish a finding chart. Our identification of this star, which is confirmed by its variability revealed on DSS images, differs from that suggested for FI Mus by López and Girard (1990). Note that the large errors of the coordinates from Goossens *et al.* (1980) caused significant difficulties in identifying other variable stars as well.

RX Mus and FN Mus. This case, which is similar to the previous one, was found by us. The identification by López and Girard (1990) is correct. This identification was also confirmed by our findings in the Harvard archives.

YZ Mus and GH Mus. Another similar case: the first discovery was by Swope (1931); the Mira period is virtually equal to the value given by Goossens *et al.* (1980). The identification is based on the chart from Shapley and Swope (1931).

AV Mus. Our identification, which was confirmed by information from the Harvard Observatory archives, differs from that suggested by López and Girard (1990).

CR Mus and FP Mus, DY Mus and FX Mus. The stars were named for the second time because of the erroneous coordinates in Goossens *et al.* (1980); their identity was first noted by López and Girard (1990).

SS Nor and QR Nor. The identity of the stars was confirmed by information from the Harvard archive. Morel (1994) gives two different identifications for these stars. His identification of SS Nor is correct, and his candidate for QR Nor is a new, as yet unstudied, red variable whose variability is confirmed by

Table 3. Examples of the coordinates and identifications for problem stars

Star	$\alpha_{2000.0}$	$\delta_{2000.0}$	Epoch	μ_α	μ_δ	Source	Identifications
IY Gem	$06^h28^m53^s.52$	$+18°09'54''.3$	1955.861			A2.0	
VW Gru	22 29 03.2	−43 29 01	1990.781			GCVS authors	IRAS 22260−4344
V403 Her	17 27 28.94	+22 14 30.3	2000.0	−0″.010	+0″.004	NPM	
V404 Her	17 27 41.47	+26 57 49.8	1950.462			A2.0	
V405 Her	17 27 46.96	+26 55 52.2	2000.0	−0.002	−0.002	NPM	
ZZ Hyi	00 27 48.07	−78 37 44.8	1977.769			A2.0	GSC 9350.01587
DM Lac	22 04 35.65	+52 53 58.8	1952.702			A2.0	IRAS 22027+5239
EG Lac	22 50 38.89	+55 14 52.1	1991.7			B1.0	
EU Lac	22 25 31.93	+51 43 38.9	2000.0	0.005	−0.001	AC	GSC 3619.01864
HQ Lac	22 04 25.04	+52 54 26.4	1952.702			A2.0	
PU Lac	22 09 05.52	+50 27 57.8	1952.713			A2.0	IS Lac, GSC 3614.00609, IRAS 22071+5013
EN Lib	15 44 41.06	−28 39 55.1	2000.0	+0.003	−0.003	AC	GT Lib, GSC 6789.00928, IRAS 15416−2830
EX Lib	15 55 41.00	−12 47 33.8	1954.268			A2.0	
AZ Lup	15 22 38.85	−43 06 18.4	1978.227			A2.0	IRAS 15193−4255
DY Lup	14 39 57.20	−43 14 09.2	1980.819			A2.0	IRAS 14367−4301
DZ Lup	14 39 46.13	−43 15 46.7	2000.0	−0.011	−0.004	Tyc2	Tyc2 7818 118 1, GSC 7818.00118, IRAS 14365-4302
BV Lyr	19 17 42.92	+32 57 30.7	2000.0	−0.002	+0.004	Tyc2	Tyc2 2657 1380 1, GSC 2657.1380
V369 Lyr	19 11 55.40	+32 12 07.5	1960.619			GCVS authors	
V408 Lyr	18 59 02.34	+27 28 19.8	1992.422			GSC2.2	
V479 Lyr	18 37 14.65	+42 49 28.5	1982.389			GSC	GSC 3113.00241
V480 Lyr	18 40 23.37	+43 56 20.8	1993.393			GSC2.2	GSC 3130.01641, ROTSE1 J184023.50 +435622.4
UW Men	07 14 09.36	−84 45 47.2	1978.102			GSC	GSC 9497.01189, IRAS 07229−8440
V567 Mon	07 01 56.54	−01 46 30.2	1992.908			GSC2.2	
RV Mus	12 49 07.92	−70 02 46.2	1978.103			A2.0	FI Mus
RX Mus	12 54 13.78	−72 12 24.7	1978.103			A2.0	FN Mus

Table 3. (Contd.)

Star	$\alpha_{2000.0}$	$\delta_{2000.0}$	Epoch	μ_α	μ_δ	Source	Identifications
YZ Mus	$13^h31^m13\overset{s}{.}18$	$-67°41'36\overset{''}{.}2$	1978.103			A2.0	GH Mus
AV Mus	13 47 12.64	−70 38 11.8	1999.140			GSC2.2	
CR Mus	12 58 38.12	−74 17 10.7	2000.0	$-0\overset{''}{.}018$	$+0\overset{''}{.}013$	AC	FP Mus
DY Mus	13 16 58.04	−67 52 30.9	1987.083			GSC	FX Mus, GSC 9242.00218, IRAS 13135−6736
SS Nor	16 13 21.89	−59 46 56.6	1987.384			GSC	QR Nor, GSC 8723.00573, IRAS 16090−5939
EG Nor	16 22 11.68	−61 15 55.0	2000.0	−0.004	−0.008	Tyc2	Tyc2 9037 2327 1, GSC 9037.2327, IRAS 16177−6108
QT Nor	16 34 03.96	−59 05 12.8	1997.318			GSC2.2	GG Nor
RR Oct	20 55 42.61	−74 58 22.3	2000.0	−0.003	−0.019	Tyc2	SV Oct, Tyc2 9333 1112 1, GSC 9333.01112, IRAS 20500−7509
PU Oph	17 01 24.74	−30 06 31.7	1988.395			GSC2.2	V29, V28 (NGC 6266)
V362 Oph	17 09 39.59	−28 45 58.6	1997.321			GSC2.2	NSV 20993
V483 Oph	18 01 19.57	+02 58 01.5	1991.458			GSC2.2	GSC 434.02819, IRAS 17588+0258
V586 Oph	18 27 13.95	+04 17 15.3	2000.0	−0.001	+0.007	AC	GSC 441.00699
V838 Oph	18 01 44.73	+10 23 42.6	2000.0	+0.007	−0.006	Tyc2	Tyc2 1012 997 1, GSC 1012.00997, IRAS 17593+1023
V886 Oph	18 24 14.90	+09 59 43.0	1950.541			A2.0	Uncertain identification
V898 Oph	18 38 27.64	+07 05 21.7	1991.387			GSC2.2	
V1069 Oph	17 41 56.33	−01 01 27.6	1982.627			GSC	GSC 5081.02167
V1077 Oph	17 52 09.68	+06 58 13.0	1953.613			A2.0	
V1110 Oph	18 36 02.59	+07 27 08.8	1990.633			GSC2.2	IRAS 18336+0724
V1111 Oph	18 37 19.26	+10 25 42.4	1991.387			GSC2.2	IRAS 18349+1023
V1113 Oph	18 39 16.55	+08 39 41.0	1991.387			GSC2.2	IRAS 18368+0836
V1496 Oph	17 10 01.87	−17 25 17.9	1980.896			A2.0	
V2040 Oph	18 27 30.89	+10 09 05.9	1993.535			GSC2.2	GSC 1027.01788 (NE component)
V2137 Oph	17 09 59.97	−26 33 56.9	1997.326			GSC2.2	V2 (NGC 6293); Uncertain identification

the Schmidt sky survey images presented by the US Naval Observatory archive.

EG Nor. This virtually unstudied variable, discovered by Hoffleit (1931), was found thanks to the Harvard archives, 1° south of the discoverer's position. The same result was also reported by Webbink *et al.* (2002), who noted that, with corrected coordinates, the star is in the constellation Triangulum Australe. We retain its traditional name.

GG Nor and QT Nor. As was correctly pointed out by Webbink *et al.* (2002), the coordinates of GG Nor published by its discoverer (Hoffleit 1931) were erroneous by 1° in declination (the star lies north of the published position). After its coordinates were corrected, the variable could be identified with the star QT Nor (Luyten 1935; Hoffmeister 1963) that later received its GCVS name. Since correct coordinates were adopted for the latter star from the outset, and we adopted QT Nor as the main name for this object.

RR Oct and SV Oct. The discoverer of the Mira SV Oct, Gerasimovich (1927), published a position for this star that was in error by more than 1° in declination. The bona fide SV Oct, which is located north of the earlier position, was found using Gerasimivich's notebooks stored at the Harvard Observatory and turned out to be identical to the Mira RR Oct, as confirmed by the similarity of the periods in the catalogue. We adopt RR Oct as the primary name.

BE Oph. We failed to find any variable stars at the position given by the discoverer (Beljawsky 1927). Thus, this star was not included in Table 3. Hughes Boyce (1942) reported the study of BE Oph, a Mira variable. However, we found the star that she studied by using information from the Harvard archives at 20′ from the position published by Beljawsky. We consider it impossible to identify this star with BE Oph. On the other hand, the star studied by Hughes Boyce is undoubtedly identical to the variable NSV 07549 = BV 1679, whose discovery was reported by Strohmeier and Knigge (1975). We will include this star in one of the next Name Lists as a new variable.

PU Oph. For historical reasons, this GCVS name refers to a blend of two RR Lyrae variables, V28 and V29, in the globular cluster NGC 6266. The coordinates in Table 3 correspond to V29; the star V28 lies four arcseconds to the north.

V362 Oph. After its coordinates were improved, the object NSV 20993 turned out to be identical to this variable.

V483 Oph. Our identification of this Mira star using the discoverer's chart (Hoffmeister 1957) lead to a significant change in the right ascension. The identification is confirmed by the unusual color index ($B_J - R = -0.8$) in the GSC2.2 catalogue. Richter (1965) pointed out that the star is very red and close to the limit of the "blue" Palomar print; this description contradicts our identification.

V586 Oph. Kinnunen and Skiff (2000a) correctly identified this variable with the GSC, but their coordinates based on the Tyc2 catalogue are inaccurate. A large proper motion is given for the object named Tyc2 441 1241 1 in the latter catalogue; this proper motion is probably due to the erroneous combination of the second epoch for GSC 0441.01241 with the first epoch for V586 Oph = GSC 0441.00699.

V838 Oph. The two finding charts available for this variable in the literature (Hoffmeister 1933; Tsesevich 1952) seem incompatible. We think that they refer to the same star but are severely distorted. This star is identical to a variable point source in the IRAS catalogue. Paloque *et al.* (1961) adopted a different identification , which, in our opinion, is erroneous.

V886 Oph. Our slightly unreliable identification differs from that suggested by Kinnunen and Skiff (2000b).

V898 Oph. We identify this object with a star whose variability was confirmed by using electronic image archives. The identification of Kinnunen and Skiff (2000b) is wrong.

V1069 Oph. The identification problems resulted from the wrong sign of the declination in the report on the discovery of this near-equator variable (Hoffmeister 1966).

V1077 Oph. Layden (1998) identifies this variable incorrectly.

V1110 Oph, V1111 Oph, and V1113 Oph. In our opinion, the identifications of these three red variables by Kato (1999a) are erroneous. In the case of V1110 Oph, the variability of our candidate was confirmed by digital survey images.

V1496 Oph. The coordinates published by the discoverer (Plaut 1968) contradict the unpublished chart that he made available to us. Based on the star's brightness, we preferred the identification in accordance with the chart.

V1548 Oph. Schmeer (2000) identified this dubious Nova (Plaut 1968), for which Plaut sent to us a wrong chart (Antipin *et al.* 1994b), with the minor planet (336) Lacadiera. This object was not included in Table 3.

V2040 Oph. Our identification, which is confirmed by the presence of a close companion southwest of the variable (Götz and Wenzel 1956), differs from that suggested by Kinnunen and Skiff (2000b).

V2061 Oph. The coordinates published by Kukarkin (1962) are, probably, seriously in error. The field shown in the finding chart from this paper could not be found in a rather wide neighborhood on plates of

the Moscow stacks. This star was not included in Table 3.

V2063 Oph. It was found on the Harvard plate of July 19–20, 1932, where it was discovered by Luyten (1937), and identified with the minor planet (64) Angelina. This object was not included in Table 3.

V2137 Oph. Our identification with a star in a blend of two or more components is based on the chart from Clement *et al.* (1982). It remains unreliable, because the chart from Sawyer (1943) leads to a different star.

CONCLUSIONS

Below, we list the Internet addresses that correspond to the new resources presented in this paper.

The version of the GCVS Volume II with improved coordinates is available at ftp://ftp.zeus.sai.msu.ru/pub/groups/cluster/gcvs/gcvs/vol2/ or at http://www.sai.msu.su/groups/cluster/gcvs/gcvs/vol2/. The corrections made to the new version of the GCVS Volume II were taken into account in the catalogue's search engine at http://www.sai.msu.su/groups/cluster/gcvs/cgi-bin/search_new.html.

ACKNOWLEDGMENTS

We wish to thank T.M. Tsvetkova, who prepared the files of remarks to the GCVS Volumes II and III. We are grateful to A.A. Volchkov and J. Manek (Czech Republic), who put the software at our disposal. We are also grateful to S.V. Antipin for assistance, L.N. Berdnikov for providing unpublished finding charts for several southern Cepheids, and C. Lopez (Argentina) and P. Schmeer (Germany) for providing their results before their publication. We wish to thank the researchers who helped us in identifying the lost variables using plates from other observatories. This study was supported in part by the Russian Foundation for Basic Research (project no. 02-02-16069), the Program of Support for Leading Scientific Schools of Russia (project no. 00-15-96627), the Federal Program "Astronomy," and the Program "Nonstationary Processes in Astrophysics" of the Presidium of the Russian Academy of Sciences. We used the Digitized Sky Survey images provided by the Hubble Space Telescope Science Institute under the support of grant NAG W-2166 from the Government of the USA and the data from the US Naval Observatory Flagstaff Station Image and Catalogue Archive (http://www.nofs.navy.mil/data/fchpix/). We are grateful to the referee, Dr. L.R. Yungelson, for valuable remarks.

REFERENCES

1. C. Akerlof, S. Amrose, R. Balsano, *et al.*, Astron. J. **119**, 1901 (2000).
2. Z. Alksne and A. Alksnis, Astron. Tsirk. No. 670 (1972).
3. S. V. Antipin, N. N. Kireeva, and N. N. Samus, Inf. Bull. Var. Stars, No. 4020 (1994a).
4. S. V. Antipin, N. N. Kireeva, and N. N. Samus, Inf. Bull. Var. Stars, No. 4021 (1994b).
5. S. J. Bailey, Harvard Obs. Bull., No. 792 (1923).
6. S. Beljawsky, Astron. Nachr. **230**, 349 (1927).
7. C. M. Clement, P. S. Panchhi, and T. R. Wells, Astron. J. **87**, 1491 (1982).
8. R. A. Downes and M. M. Shara, Publ. Astron. Soc. Pacific **105**, 127 (1993).
9. R. A. Downes, R. F. Webbink, M. M. Shara, *et al.*, *A Catalog and Atlas of Cataclysmic Variable Stars, Living Edition*; http://icarus.stsci.edu/~downes/cvcat/index.html (2003).
10. ESA (European Space Agency), *The Hipparcos and Tycho Catalogues*, SP-1200 (1997).
11. B. P. Gerasimovič, Harvard Obs. Bull., No. 853, 1 (1927).
12. H. Geßner, Mitt. Veränd. Sterne **9**, 57 (1981a).
13. H. Geßner, Mitt. Veränd. Sterne **9**, 115 (1983).
14. H. Geßner, Veröff. Sternwarte Sonneberg **9**, 361 (1981b).
15. M. Goossens, C. Stoop, and C. Waelkens, Inf. Bull. Var. Stars No. 1760 (1980).
16. W. Götz and W. Wenzel, Veröff. Sternwarte Sonneberg **2**, H. 5 (1956).
17. A. A. Henden and R. S. Stone, Astron. J. **115**, 296 (1998).
18. D. Hoffleit, Harvard Obs. Bull., No. 884, 10 (1931).
19. D. Hoffleit, Harvard Obs. Bull., No. 902, 13 (1936).
20. C. Hoffmeister, Astron. Nachr. **289**, 139 (1966).
21. C. Hoffmeister, Eergänzungshefte Astron. Nachr. **12** (1), (1949).
22. C. Hoffmeister, Mitt. Sternwarte Sonneberg No. 22 (1933).
23. C. Hoffmeister, Mitt. Veränd. Sterne, No. 249 (1957).
24. C. Hoffmeister, Veröff. Sternwarte Sonneberg, **6**, 1 (1963).
25. E. Hughes Boyce, Harvard Obs. Ann. **109**, 9 (1942).
26. E. Høg, C. Fabricius, V. V. Makarov, *et al.*, *The Tycho-2 Catalogue* (Copenhagen, 2000), CD-ROM.
27. B. F. Jones and M. F. Walker, Astron. J. **95**, 1755 (1988).
28. T. Kato, Inf. Bull. Var. Stars, No. 4789 (1999a).
29. T. Kato, Inf. Bull. Var. Stars, No. 4790 (1999b).
30. T. Kinnunen and B. A. Skiff, Inf. Bull. Var. Stars, No. 4863 (2000a).
31. T. Kinnunen and B. A. Skiff, Inf. Bull. Var. Stars, No. 4905 (2000b).
32. T. Kinnunen and B. A. Skiff, Inf. Bull. Var. Stars, No. 4906 (2000c).
33. P. N. Kholopov, N. N. Samus', M. S. Frolov, *et al.*, *General Variable Stars Catalogue* (Nauka, Moscow, 1985–1988), Vols. I–III, 4th ed.

34. P. N. Kholopov, N. N. Samus, N. M. Artiukhina, *et al.*, Centre de Données Astronomiques de Strasbourg, II/214A (1998).
35. A. R. Klemola, R. B. Hanson, and B. F. Jones, Centre de Données Astronomiques de Strasbourg, I/199 (1987).
36. B. V. Kukarkin, Perem. Zvezdy **14**, 21 (1962).
37. N. E. Kurochkin, Perem. Zvezdy **16**, 460 (1968).
38. N. E. Kurochkin, Perem. Zvezdy **17**, 620 (1971).
39. C. O. Lampland, Astron. Nachr. **198**, 353 (1914).
40. B. M. Lasker, C. R. Sturch, and B. J. McLean, Astron. J. **99**, 2019 (1990).
41. A. C. Layden, Astron. J. **115**, 193 (1998).
42. C. E. López and T. M. Girard, Publ. Astron. Soc. Pacific **102**, 1018 (1990).
43. C. E. López and H. S. Lépez, Inf. Bull. Var. Stars, No. 4824 (2000).
44. W. J. Luyten, Astron. Nachr. **258**, 122 (1935).
45. W. J. Luyten, Astron. Nachr. **261**, 455 (1937).
46. P. Maffei, Contrib. Oss. Astrofis. Asiago, No. 136 (1963).
47. N. W. McLeod and H. H. Swope, Harvard Obs. Bull., No. 915, 29 (1941).
48. W. J. Miller and A. A. Wachmann, Spec. Vaticana Ricerche Astron. **8** (12) (1971).
49. D. Monet, A. Bird, B. Canzian, *et al.*, *USNO-A V2.0. A Catalog of Astrometric Standards* (US Naval ObservatoryWashington, 1998), 11 CD ROMs.
50. D. G. Monet, S. E. Levine, B. Casian, *et al.*, Astron. J. (2003, in press).
51. M. Morel, Inf. Bull. Var. Stars, No. 4037 (1994).
52. *Abbout 4 000 000 Star Catalog,* Ed. by A. P. Gulyaev and V. V. Nesterov (Izd. Mosk. Gos. Univ., Moscow, 1992).
53. G. Neugebauer, R. J.van Duinen, H. J. Habing, *et al.*, *IRAS Point Source Catalog* (NASA, Washington, 1988).
54. E. Paloque, P. Pretre, and M. Reynis, Ann. Obs. Astron. Toulouse **28**, 7 (1961).
55. E. N. Pastukhova, Inf. Bull. Var. Stars, No. 5196 (2001).
56. L. Plaut, Bull. Astron. Inst. Netherl., Suppl. Ser. **1**, No. 3 (1966).
57. L. Plaut, Bull. Astron. Inst. Netherl., Suppl. Ser. **2**, No. 6 (1968).
58. G. Richter, *Astronomische Abhandlungen, Prof. Dr. Cuno Hoffmeister zum 70. Geburtstage gewidmet* (Leipzig, 1965), p. 98.
59. S. Röser, U. Bastian, L. I. Yagudin, and V. V. Nesterov, *PPM Star Catalogue, Positions, and Proper Motions* (Astronomisches Rechen-Institut, Heidelberg, 1991–1993).
60. N. N. Samus, Inf. Bull. Var. Stars, No. 5083 (2001).
61. N. N. Samus', V. P. Goranskiĭ, O. V. Durlevich, *et al.*, Pis'ma Astron. Zh. **28**, 201 (2002) [Astron. Lett. **28**, 174 (2002)].
62. H. B. Sawyer, Publ. David Dunlap Obs. **1**, No. 14 (1943).
63. P. Schmeer, Private Communication (2000).
64. P. Schmeer, Private Communication (2002).
65. H. Shapley and H. H. Swope, Harvard Obs. Bull. No. 885, 13 (1931).
66. B. A. Skiff, Inf. Bull. Var. Stars, No. 4675 (1999a).
67. B. A. Skiff, Inf. Bull. Var. Stars, No. 4719 (1999b).
68. B. A. Skiff, Inf. Bull. Var. Stars, No. 4720 (1999c).
69. M. F. Skrutskie, S. E. Schneider, R. Stiening, *et al.*, *The Two Micron All Sky Survey* (Centre de Données Astronomiques de Strasbourg, B/2mass, 2000).
70. W. Strohmeier and R. Knigge, Veröff. Sternwarte Bamberg **10** (116) (1975).
71. STScI (The Space Telescope Science Institute and Osservatorio Astronomico di Torino), *The Guide Star Catalogue, Version 2.2* (Centre de Données Astronomiques de Strasbourg, I-271, 2001).
72. H. H. Swope, Harvard Obs. Bull., No. 883, 23 (1931).
73. H. Swope and I. Caldwell, Harvard Obs. Bull., No. 879, 10 (1930).
74. V. P. Tsesevich, Perem. Zvezdy **8**, 422 (1952).
75. V. P. Tsesevich and M. S. Kazanasmas, *Atlas of Variable Stars Guide Maps* (Nauka, Moscow, 1971).
76. S. E. Urban, T. E. Corbin, and G. L. Wyckoff, *The ACT Reference Catalog* (US Naval Observatory, Washington, 1997).
77. A. A. Volchkov and O. A. Volchkov, http://www.simfov.ru (2003).
78. R. F. Webbink, M. L. Hazen, and D. Hoffleit, Inf. Bull. Var. Stars, No. 5298 (2002).
79. N. Zacharias, S. E. Urban, M. I. Zacharias, *et al.*, Astron. J. **120**, 2131 (2000).

Translated by N. Samus'

Astronomy Letters, Vol. 29, No. 7, 2003, pp. 480–485. Translated from Pis'ma v Astronomicheskiĭ Zhurnal, Vol. 29, No. 7, 2003, pp. 545–551.

The Candidate Protoplanetary Object IRAS 22223+4327 Is a Pulsating Variable Star

V. P. Arkhipova*, R. I. Noskova, N. P. Ikonnikova, and G. V. Komissarova

Sternberg Astronomical Institute, Universitetskii pr. 13, Moscow, 119992 Russia

Received January 26, 2003

Abstract—We present our photoelectric UBV observations of the candidate protoplanetary object IRAS 22223+4327 during four visibility seasons. The star exhibited periodic brightness variations with the maximum amplitudes $\Delta U = 0\overset{m}{.}23$, $\Delta B = 0\overset{m}{.}18$, and $\Delta V = 0\overset{m}{.}12$ and a time scale of about 90 days, which is equal to the period derived by other authors from radial velocities. During these brightness variations, a correlation is observed between the $(B-V)$ color index and brightness, which is characteristic of pulsations. We estimated the star's spectral type from our photometric data to be F8 I. We detected a "deficit" of light in the U band. The star's mean brightness and its spectral type appear to have not changed in the past half a century. © *2003 MAIK "Nauka/Interperiodica".*

Key words: *pulsating variable stars, protoplanetary objects, photoelectric observations.*

INTRODUCTION

After its discovery, the IR source IRAS 22223+4327 ($22^{h}24^{m}30\overset{s}{.}67$, $+43°43'0''$ (2000)) was identified with the star BD + 42°4388 = GSC 3212.676 = DO 41288. The star is located at the Galactic latitude $b = -12°$. IRAS 22223+4327 was selected as a candidate protoplanetary object by its characteristic position in the two-color IRAS diagram (Likkel 1989).

The star's spectral type was first determined during a survey of red stars at the Dearborn Observatory (Lee *et al.* 1947). The authors of the survey classified it as a K5 star.

In 1989–1990, Hrivnak (1995) studied its optical spectrum using medium-resolution observations, estimated its spectral type using different criteria as F8–G0Ia, and detected strong Swan absorption bands of C_2 and weaker C_3 bands in the spectrum. He pointed out a discrepancy between the spectral types estimated using criteria in the blue and red spectral ranges. The high carbon abundance in the stellar atmosphere was confirmed by observations of the CO(2-1) and HCN molecules in the millimeter wavelength range (Loup *et al.* 1993). In addition, the star exhibits a prominent emission feature at 21 μm (Kwok *et al.* 1995), which is currently believed to be from carbon compounds. Apart from carbon lines, Hrivnak found enhanced absorption lines of s-process elements (Ba, Sr, and Y) in the star's spectrum. As a result of these studies, IRAS 22223+4327 was classified as a carbon protoplanetary object. Eleven such objects are known to date (Hrivnak 1997).

Like many protoplanetary objects, IRAS 22223+4327 reveals an iron underabundance, [Fe/H] = −0.4, which is attributable to the presence of a dust envelope around the star.

Decin *et al.* (1998) carried out a detailed analysis of the star's chemical composition using high-dispersion spectrograms. They determined the atmospheric parameters $T_e = 6500$ K, $\log g = 1.0$, and $\chi_t = 4.0$ km s^{-1}, which correspond to an F5 I supergiant on the temperature scale of high-luminosity stars, and pointed out a significant discrepancy between the star's temperature obtained by them and earlier estimates. They also found large overabundances of s-process elements, carbon, and nitrogen. In light of the modern theory of stellar evolution, this result may be indicative of a third dredge-up at the stage of the asymptotic giant branch for IRAS 22223+4327, which is believed to be typical of the evolution of the most massive ($\geq 0.7 M_\odot$) candidate protoplanetary objects. The presence of 21-μm emission, which is observed in more massive candidates, can also indicate that the star's mass exceeds its mean value.

The only $UBVR_cI_c$ observations of the star were performed in August 1989 by Kwok *et al.* (1995), who obtained $V = 9\overset{m}{.}69$, $B = 10\overset{m}{.}61$, $U = 11\overset{m}{.}41$, $R_c = 9\overset{m}{.}15$, and $I_c = 8\overset{m}{.}63$. Table 1 lists the published near-IR observations of the star. The discrepancy between the J magnitudes estimated by different

*E-mail: vera@sai.msu.ru

1063-7737/03/2907-0480$24.00

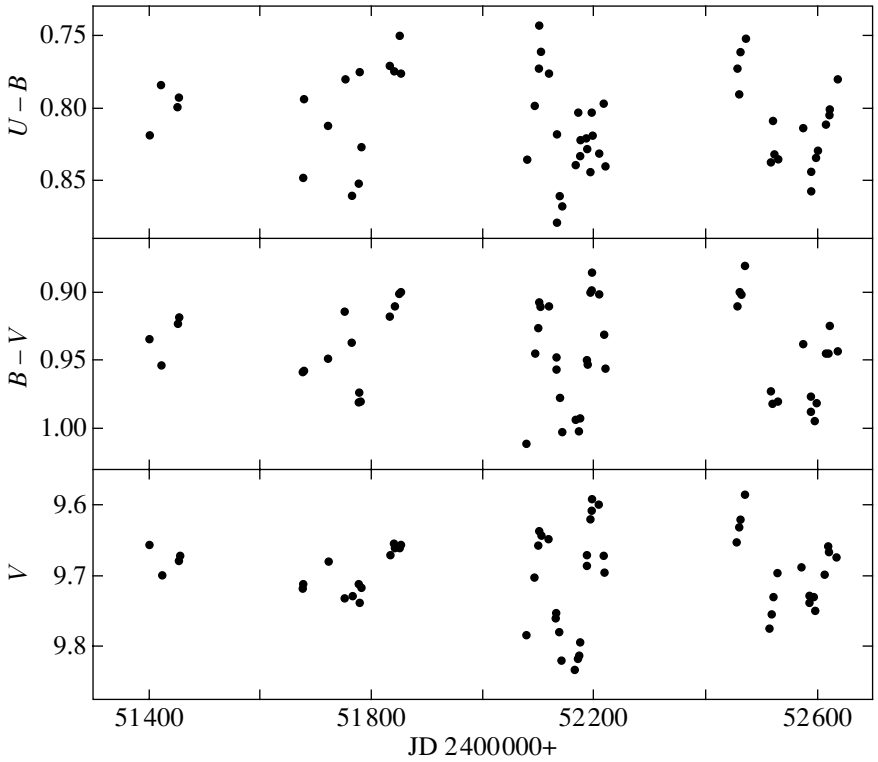

Fig. 1. The V light curve and $U-B$, $B-V$ color curves of IRAS 22223+4327 in 1999–2002.

authors is about $0^m.3$, indicating that the star may be variable.

This study was aimed at searching for the optical photometric variability of IRAS 22223+4327 and determining the variability type. It is part of our program of searching for photometric variability of protoplanetary objects, which has been carried out since 1990. As a result of our program, we have already found or refined the pattern of brightness variations for more than ten supergiants with IR excesses (Arkhipova *et al.* 2000, 2001, 2002). In addition, one of our objectives was to study the secular photometric behavior of IRAS 22223+4327 in connection with the fact that it may belong to more massive and rapidly evolving objects. The latter was also suggested by the discrepancy between the temperatures estimated for the star in the past half century. Finally, it was of considerable interest to estimate the circumstellar component of the total extinction for the star surrounded by a dust envelope.

UBV OBSERVATIONS OF IRAS 22223+4327 AND DATA ANALYSIS

Our UBV observations of IRAS 22223+4327, which were aimed at searching for possible photometric variability, began in 1999. From October 1999 until December 2002, we obtained 56 magnitude estimates for the star with a photoelectric photometer attached to the 60-cm Zeiss-600 telescope at the Crimean Station of the Sternberg Astronomical Institute. A 27″ photometer aperture was used for the observations. The comparison star was HD 212247; its magnitudes ($V = 7^m.97$, $B = 9^m.10$, $U = 10^m.22$) were determined by using the photometric standard HD 199216 as a reference (Hiltner 1956). The measurement accuracy was $\sim 0^m.01$. Table 2 presents the UBV observations of the star in 1999–2002, and Fig. 1 shows the V light curve and $U-B$, $B-V$ color curves. The mean magnitudes estimated from all our observations were $\langle V\rangle = 9^m.70$, $\langle B\rangle = 10^m.65$, and $\langle U\rangle = 11^m.46$. The season of 2001, which spans the time interval JD 2452079–52220 (141 days), was most completely covered by observations. During this period, the star clearly showed sine-wave brightness variations with the maximum amplitudes $\Delta U = 0^m.23$, $\Delta B = 0^m.18$, and $\Delta V = 0^m.12$. The two light maxima in this interval occurred at JD 2452110 and JD 2452200 separated by $\Delta t = 90$ days. Our search for periodicities made by using the entire series of observations with the code written by Yu.K. Kolpakov (Fourier analysis of the time series) revealed the period $P = 90^d.1 \pm 5^d.1$. The phase B light curve folded with a $90^d.1$ period is shown in Fig. 2. This period determination is preliminary, because the number of observations is small. However, it is equal, within the error limits, to the period $P = 89^d$ derived by Hriv-

Table 1. The near-IR observations of IRAS 22223+4327

Date	J	H	K	Author
August 17, 1989	7.89	7.46	7.25	Kwok *et al.* (1995)
November–December 1989	8.15	7.72	7.25	Garcia-Lario *et al.* (1997)
	±0.03	±0.03	±0.03	
June 1990	7.87	7.43	7.20	Garcia-Lario *et al.* (1997)
	±0.02	±0.02	±0.02	

nak (1997) from the unpublished radial velocities of the star. Over the entire period of our observations, the maximum amplitudes of the $(B-V)$ and $(U-B)$ color variations were $\Delta(U-B) \approx 0^m.08$ and $\Delta(B-V) \approx 0^m.05$. The star's brightening is accompanied by a decrease in the $(B-V)$ color index, which is most probably related to a temperature rise as the brightness maximum is approached (see Fig. 3). The correlation between $(U-B)$ and brightness is much weaker.

There are discrepancies in the more recent determinations of the spectral type for IRAS 22223+4327: F8–G0 I (Hrivnak 1995) and F5 I (Decin *et al.* 1998). To improve the spectral type, we can try to use photometric data by simultaneously estimating the star's interstellar reddening.

An allowance made for the interstellar reddening based on the standard law, $(E(U-B)/E(B-V) = 0.72 + 0.05E(B-V))$ (Straizys 1977), does not bring the star into the sequence of normal supergiants in the two-color $U-B$, $B-V$ diagram (Fig. 4). Since the observations of Kwok *et al.* (1995) are in good agreement with our UBV measurements, there are no systematic errors in the photometry. We can assume that one or both color indices of the star are not equal to the normal colors of supergiants. To test this assumption, we constructed the two-color $B-V, V-R_c$ diagram (Fig. 5) and plotted the measurements of Kwok *et al.* (1995) on it. We see no anomaly in the star's position in this diagram and its $B-V$ and $V-R_c$ color indices quite agree with those for a normal F8 I supergiant with a color excess of $E(V-R_c) = 0.25$ or $E(B-V) = 0.30$. Therefore, the $U-B$ color index is anomalous; it is redder than it should be for an F8 I star. This ultraviolet deficit may result from the star's chemical peculiarities that appeared during its evolution. Note also that the $U-B$ color index poorly follows the star's pulsations.

The discrepancies between the recent determinations of the spectral type for the star may well attributable to temperature variations during the pulsation cycle, as is confirmed by the $B-V$ color variations that we detected.

The maximum interstellar extinction in the Galaxy at the latitude $b = -12°$ was estimated using Parenago's formula (Sharov 1963) to be $A_V = 0^m.87$ or $E(B-V) = 0^m.28$. The maximum reddening was estimated from the distribution of neutral hydrogen in the Galaxy and from galaxy counts (Heiles 1976) to be $E(B-V) = 0^m.3$. It thus follows that the circumstellar extinction in IRAS 22223+4327 is most likely

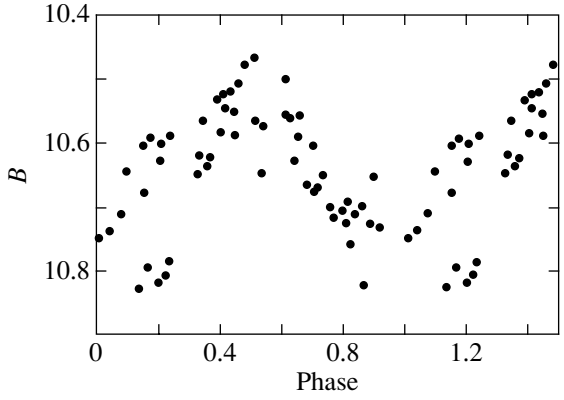

Fig. 2. The B-band phase light curve of IRAS 22223+4327 folded with a $90^d.1$ period.

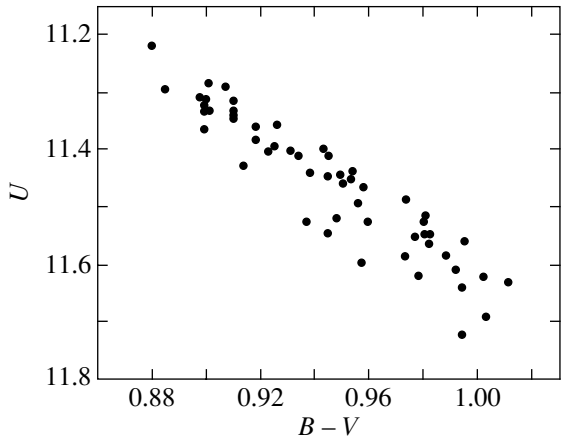

Fig. 3. The color–magnitude diagram for IRAS 22223+4327.

Table 2. The UBV observations of IRAS 22223+4327 in 1999–2002

JD 2400000+	U	B	V	$U-B$	$B-V$	JD 2400000+	U	B	V	$U-B$	$B-V$
51402	11.409	10.590	9.656	0.819	0.934	52172	11.622	10.819	9.817	0.803	1.002
51424	11.438	10.654	9.700	0.784	0.954	52174	11.640	10.807	9.813	0.833	0.994
51452	11.400	10.601	9.678	0.799	0.923	52175	11.608	10.786	9.794	0.822	0.992
51455	11.382	10.589	9.671	0.793	0.918	52186	11.457	10.636	9.686	0.821	0.950
51677	11.525	10.677	9.718	0.848	0.959	52187	11.452	10.624	9.671	0.828	0.953
51678	11.464	10.670	9.712	0.794	0.958	52193	11.363	10.519	9.620	0.844	0.899
51722	11.441	10.629	9.680	0.812	0.949	52195	11.309	10.506	9.608	0.803	0.898
51752	11.426	10.646	9.732	0.780	0.914	52197	11.296	10.477	9.592	0.819	0.885
51765	11.525	10.665	9.728	0.860	0.937	52209	11.331	10.500	9.599	0.831	0.901
51777	11.545	10.693	9.712	0.852	0.981	52217	11.400	10.603	9.672	0.797	0.931
51779	11.486	10.711	9.737	0.775	0.974	52220	11.492	10.652	9.696	0.840	0.956
51781	11.524	10.697	9.717	0.827	0.980	52455	11.337	10.564	9.654	0.773	0.910
51834	11.359	10.588	9.670	0.771	0.918	52459	11.322	10.532	9.633	0.790	0.899
51840	11.340	10.565	9.655	0.775	0.910	52461	11.283	10.522	9.621	0.761	0.901
51842	11.346	10.572	9.662	0.774	0.910	52470	11.218	10.466	9.586	0.752	0.880
51850	11.311	10.561	9.661	0.750	0.900	52515	11.585	10.748	9.775	0.837	0.973
51853	11.333	10.557	9.658	0.776	0.899	52518	11.546	10.737	9.755	0.809	0.982
52079	11.631	10.795	9.784	0.836	1.011	52521	11.544	10.712	9.731	0.832	0.981
52093	11.446	10.648	9.703	0.798	0.945	52528	11.514	10.679	9.698	0.835	0.981
52100	11.356	10.583	9.657	0.773	0.926	52572	11.442	10.628	9.690	0.814	0.938
52101	11.288	10.545	9.638	0.743	0.907	52586	11.550	10.706	9.729	0.844	0.977
52104	11.314	10.553	9.643	0.761	0.910	52587	11.583	10.726	9.738	0.857	0.988
52119	11.333	10.557	9.647	0.776	0.910	52594	11.560	10.726	9.731	0.834	0.995
52132	11.518	10.700	9.752	0.818	0.948	52597	11.561	10.732	9.750	0.829	0.982
52133	11.596	10.717	9.760	0.879	0.957	52613	11.546	10.645	9.700	0.811	0.945
52138	11.619	10.758	9.780	0.861	0.978	52618	11.410	10.605	9.660	0.805	0.945
52142	11.691	10.823	9.820	0.868	1.003	52620	11.394	10.593	9.668	0.801	0.925
52166	11.723	10.827	9.833	0.839	0.994	52634	11.398	10.618	9.675	0.780	0.943

low. This result disagrees with the data of Kwok *et al.* (1995). Based on their model of a star with a dust envelope, they found an appreciable optical depth of the circumstellar dust in the visible wavelength range. It should be noted that Kwok *et al.* (1995) used the maps of Neckel and Klare (1980), which do not cover the Galactic regions with $|b| > 10°$, to estimate the interstellar reddening for IRAS 22223+4327.

THE PHOTOMETRIC HISTORY OF IRAS 22223+4327 AND ITS SPECTRAL TYPE IN THE PAST

As was noted above, there is evidence that IRAS 22223+4327 can belong to the group of more massive post-AGB stars. Hence, one may expect the star's rapid evolution toward planetary nebulae—an increase in the temperature at constant luminosity—

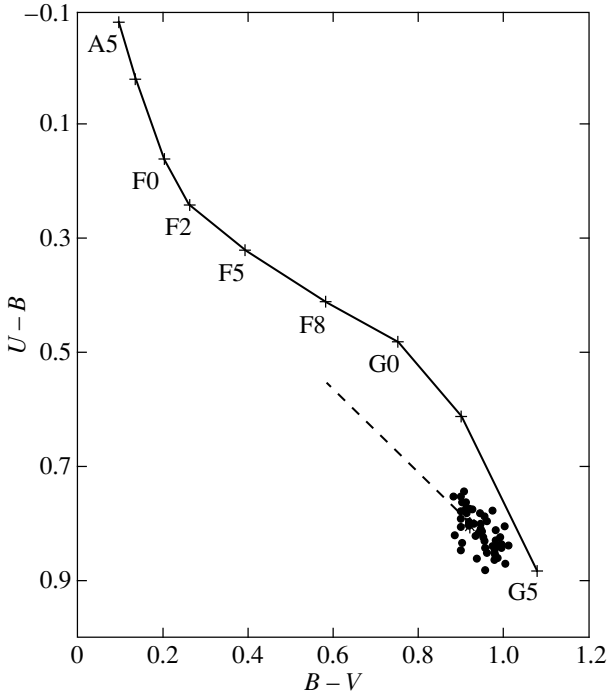

Fig. 4. IRAS 22223+4327 in the $U-B$, $B-V$ diagram. The solid line indicates the normal colors of supergiants, as prescribed by Straizys (1977); the dashed line represents the interstellar reddening line for the normal law; the dots represent our observations; and the asterisk represents the observations of Kwok *et al.* (1995).

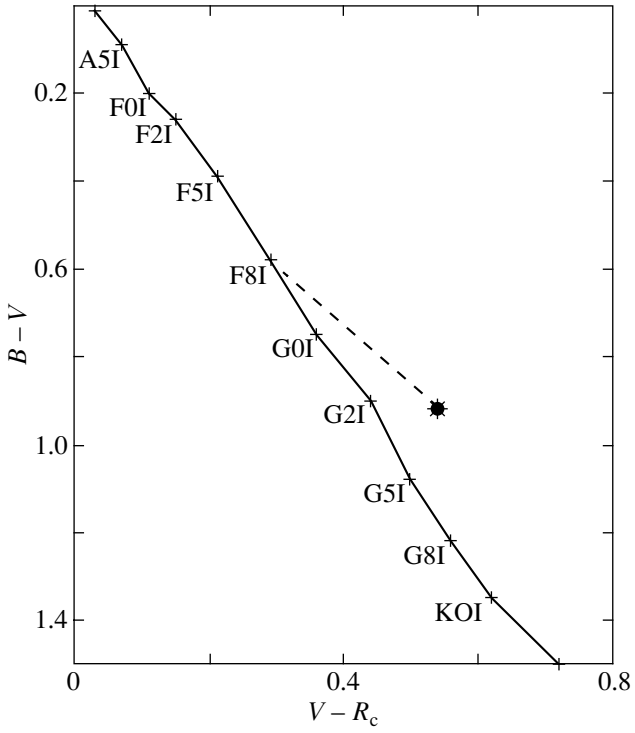

Fig. 5. IRAS 22223+4327 in the $B-V$, $V-R_c$ diagram. The solid line indicates the normal colors of supergiants; the dashed line represents the interstellar reddening line; and the asterisk represents the observations of Kwok *et al.* (1995).

especially since the current spectral classification of the star implies a much higher temperature than its historical spectral classification of the 1940s, K5 (Lee *et al.* 1947). If the time variation of the star's spectral type is real, then it must be reflected in its photometric behavior.

According to Flower (1996), the difference between the bolometric corrections for K5 I and F8 I is $-1.53-(-0.06)=-1.47$ and, in the case of temperature evolution at constant luminosity, the star should have brightened by more than a magnitude since the epoch of the Dearborn Observatory (DO) catalog. Its magnitude in the DO catalog derived from panchromatic plates is $9^m.8$. We compared the magnitudes from the DO catalog (Lee *et al.* 1947) with Johnson's V magnitudes taken from the Tycho catalog. We made a sample of 41 stars from the DO catalog with coordinates from $22^h17^m.9$ to $22^h22^m.6$ (1900) in right ascension and from $+40°$ to $+55°$ in declination and studied the correlation between their V_J magnitudes from the Tycho catalog and the m(DO) magnitudes (Fig. 6). The relation is linear, $V_J = 0.924m(\mathrm{DO}) + 0.728$; the deviations from this linear law for individual stars do not exceed $0^m.36$. Thus, the magnitudes from the DO catalog are close to the V_J magnitudes in the m(DO) range under consideration.

In August 1989, Kwok *et al.* (1995) obtained $V = 9^m.69$. In the Tycho catalog, IRAS 22223+4327 = Tycho 3212-676-1 has the mean magnitude $V_J = 9^m.78$, as inferred from the observations from December 24, 1989, through February 20, 1993. The mean magnitude in 1999–2002 was $\langle V\rangle = 9^m.70$. Thus, in more than 50 years, the star's mean brightness has not changed and the discrepancies in the spectral-type determinations can be explained, in part, by the use of different spectral classification criteria.

We compared the spectral classifications of stars in the DO catalog with the current determinations of the spectral types for stars in the same region of the sky that was used to study the photometric system of the DO catalog. Unfortunately, current spectral-type estimates are available only for 12 stars in this region. Our comparison shows that the spectral types of normal K–M stars in the DO catalog tend to be later than those given by other authors. Besides, it is improper to use the G band for the classification of carbon stars, to which IRAS 22223+4327 clearly belongs, and the intensity of this band may have been one of the classification criteria for stars in the

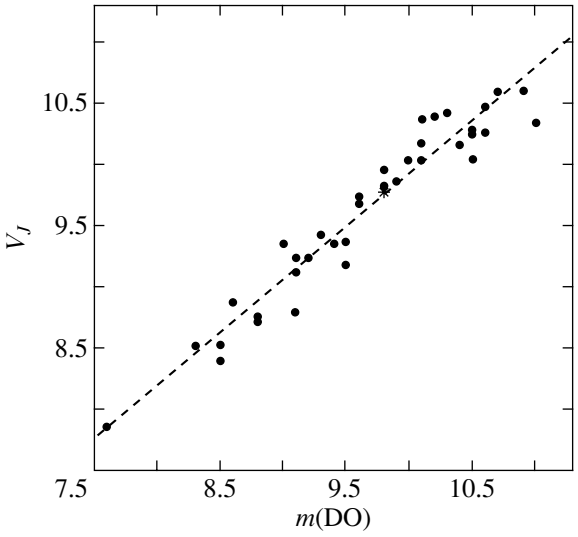

Fig. 6. The relation between the V_J magnitudes from the Tycho catalog and the magnitudes from the DO catalog for stars in the vicinity of IRAS 22223+4327 (dots). The asterisk refers to IRAS 22223+4327.

DO catalog. Therefore, it seems that one should not attach much weight to the star's classification as K5 in the 1940s.

CONCLUSIONS

Our program of searching for and studying variability in supergiant stars with IR excesses, which are candidate protoplanetary nebulae, has revealed the photometric variability of one more object, IRAS 22223+4327. This star was found to be a pulsating variable with a period of about 90 days. Previously, an 89-day period was derived by Hrivnak (1997) from the star's radial velocities. Our optical photometric data, except for the U band, agree with the F8 I spectral type estimate for the star. A deficit of light is observed in the U band; this deficit may stem from the fact that the star is a carbon representative of protoplanetary objects. Although there is evidence that the star can belong to the group of more massive post-AGB stars, we found no clear variations of its mean brightness and spectral type in the past half a century.

ACKNOWLEDGMENTS

We are grateful to the Russian Foundation for Basic Research for financial support, project no. 01-02-16530.

REFERENCES

1. V. P. Arkhipova, N. P. Ikonnikova, R. I. Noskova, *et al.*, Pis'ma Astron. Zh. **27**, 187 (2001) [Astron. Lett. **27**, 156 (2001)].
2. V. P. Arkhipova, N. P. Ikonnikova, R. I. Noskova, and G. V. Komissarova, Pis'ma Astron. Zh. **28**, 298 (2002) [Astron. Lett. **28**, 257 (2002)].
3. V. P. Arkhipova, N. P. Ikonnikova, R. I. Noskova, and G. V. Sokol, Pis'ma Astron. Zh. **26**, 705 (2000) [Astron. Lett. **26**, 609 (2000)].
4. L. Decin, H. Van Winckel, C. Waelkens, and E. Bakker, Astron. Astrophys. **332**, 928 (1998).
5. P. J. Flower, Astrophys. J. **469**, 355 (1996).
6. P. Garcia-Lario, A. Manchado, W. Pych, and S. R. Pottasch, Astron. Astrophys., Suppl. Ser. **126**, 479 (1997).
7. C. Heiles, Astrophys. J. **204**, 379 (1976).
8. W. A. Hiltner, Astrophys. J., Suppl. Ser. **2**, 389 (1956).
9. B. J. Hrivnak, Astrophys. J. **438**, 341 (1995).
10. B. J. Hrivnak, *IAU Symp. 180: Planetary Nebulae,* Ed. by B. J. Habing and H. J. G. L. M. Lamers (Kluwer Acad., Dordrecht, 1997), p. 303.
11. S. Kwok, B. J. Hrivnak, and T. R. Geballe, Astrophys. J. **454**, 394 (1995).
12. O. J. Lee, G. D. Gore, and T. J. Bartlett, Ann. Dearborn Observ. Vol. V, Part 1c (1947).
13. L. Likkel, Astrophys. J. **344**, 350 (1989).
14. C. Loup, T. Forveille, A. Omont, and J. F. Paul, Astron. Astrophys., Suppl. Ser. **99**, 291 (1993).
15. T. H. Neckel and G. Klare, Astron. Astrophys., Suppl. Ser. **42** , 251 (1980).
16. A. S. Sharov, Astron. Zh. **40**, 900 (1963) [Sov. Astron. Rep. **7**, 689 (1963)].
17. V. L. Straizys, *Multicolor Stellar Photometry* (Mokslas, Vilnius, 1977).

Translated by N. Samus'

Astronomy Letters, Vol. 29, No. 7, 2003, pp. 486–493. Translated from Pis'ma v Astronomicheskiĭ Zhurnal, Vol. 29, No. 7, 2003, pp. 552–559.

The Resonant Excitation of Transverse Oscillations in Coronal Loops

A. M. Uralov*

Institute for Solar-Terrestrial Physics, Siberian Branch, Russian Academy of Sciences, P.O. Box 4026, Irkutsk, 664033 Russia

Received October 29, 2002

Abstract—We suggest a way of self-consistently solving the problem of the excitation and rapid damping of coronal loop oscillations observed from the TRACE (Transition Region and Coronal Explorer) satellite. Oscillations are excited on the dispersion branch of fast magnetoacoustic waves, which propagate mainly across the magnetic field. The rapid damping of the observed oscillations is governed by the dispersion spreading of the pulse of these waves that was produced, for example, by a solar flare. The fundamental oscillation period is close to the period of the fundamental mode. Dissipative processes attributable to the nonideality of the plasma and the coronal-loop footpoints play no fundamental role. © *2003 MAIK "Nauka/Interperiodica".*

Key words: *Sun*.

INTRODUCTION

TRACE (Transition Region and Coronal Explorer) observations of transverse oscillations in coronal loops have prompted a number of questions to which there are no convincing answers as yet. Parameters of the observed oscillations, possible ways of explaining them, and the difficulties emerging in this case have recently been presented by Schrijver *et al.* (2002) and Aschwanden *et al.* (2002). Only the conclusion that the appearance of oscillations reflects the response of the magnetosphere of an active region to an internal or external magnetohydrodynamic (MHD) disturbance seems beyond question. The sources of such disturbances are solar flares or filament eruptions. The putative correspondence of the observed oscillations to the axisymmetric fundamental kink mode of a single coronal loop raises two questions at once: how to excite this mode and how to explain the rapid damping of the oscillation process. The third question as to why oscillations are observed only in a small group of ultraviolet loops also arises.

The question about the excitation of oscillations is considered only speculatively. It can simply be postulated that in an isolated, denser coronal loop, MHD oscillations, which are its eigenmodes, appear instantaneously. In this case, however, unrealistically large (eight or nine orders of magnitude higher than the classical values) values of the viscosity or resistivity of the coronal plasma (Nakariakov *et al.* 1999) are required to explain their rapid damping (the mean number of clearly observed oscillation periods is equal to four), even in terms of such an efficient mechanism as resonant absorption. At the same time, Solov'ev *et al.* (2002) believe that the kink oscillations of a single loop can also be rapidly damped in an ideal plasma due to its radiative losses through the emission of magnetoacoustic waves into the ambient space. The oscillation period and damping of an isolated magnetic field line can also be assumed to be entirely determined by the parameters of the oscillation process in the photospheric region from which this field line emerges (Schrijver and Brown 2000). These authors also show that the field lines that pass near the separatrix surfaces have the largest displacements during the motion of photospheric magnetic charges. In this case, the displacements of field lines on either side of this surface have opposite signs. These circumstances are invoked to account for the occasionally observed antiphase behavior of the oscillations of two closely spaced loops and should probably be taken into consideration in answering the third question in some cases. However, a different explanation is also possible.

Here, we use a plane homogeneous model magnetosphere of an active region as an example to show a way of self-consistently solving the first and second questions. The resonant excitation of oscillations and their rapid damping can be naturally explained by the appearance of a dispersion wake behind the moving MHD pulse. The wake shape depends on the sizes and geometry of the pulse source. This dependence creates an uncertainty in the problem being solved. The pulse source is assumed to be plane and extended. In the section entitled "The model and the

*E-mail: uralov@iszf.irk.ru

1063-7737/03/2907-0486$24.00

Assumptions," we discuss our assumptions and the equation that describes the response of the model magnetosphere to a disturbance moving across the magnetic field. In the section entitled "The Resonant Excitation of Oscillations," we present some of the solutions of this equation. The flare-induced disturbance is modeled by specifying a boundary regime. We estimate the effect of the presence of a rectangular inhomogeneity whose parameters are assumed to correspond to the parameters of the denser loops observed from TRACE in the ultraviolet. In conclusion, we discuss the advantages and disadvantages of the model.

THE MODEL AND THE ASSUMPTIONS

The basic equation for our analysis is the wave equation that follows from the linearized equations of ideal magnetohydrodynamics in the absence of gravity and under the additional condition $\gamma = \text{const}$, where γ is the adiabatic index:

$$\frac{\partial^2 \boldsymbol{\xi}}{\partial t^2} = C_\text{s}^2 \nabla(\nabla \cdot \boldsymbol{\xi}) + \frac{\mathbf{M}}{4\pi\rho_0}, \qquad (1)$$

$$\mathbf{M} = (\nabla \times \mathbf{B}_0) \times \mathbf{B}' + (\nabla \times \mathbf{B}') \times \mathbf{B}_0,$$
$$\mathbf{B}' = \nabla \times (\boldsymbol{\xi} \times \mathbf{B}_0).$$

Here, $C_\text{s}^2 = \gamma P_0/\rho_0$ is the square of the speed of sound; $\boldsymbol{\xi}$, ρ, and P are the displacement, density, and pressure of plasma, respectively; and $\mathbf{B}_0$ is the force-free magnetic field $(\nabla \times \mathbf{B}_0) \times \mathbf{B}_0 = 0$. The subscript "0" denotes the unperturbed quantities. There are no steady plasma flows. Disregarding the gravity is justifiable when the following inequality is satisfied: $T \ll T_\text{A} = 2\pi/\Omega_A$, where $\Omega_\text{A} = C_\text{s}/2H$, $H = C_\text{s}^2/\gamma g$, and g is the acceleration of gravity. The acoustic cutoff period T_A at a coronal temperature of 10^6 K and $\gamma = 5/3$ is $\sim$76 min. According to Schrijver *et al.* (2002) and Aschwanden *et al.* (2002), the observed coronal-loop oscillation periods T lie within the range 2–33 min, but values in the range 2–7 min dominate. Therefore, $T \ll T_\text{A}$ for most events.

A Uniform Magnetic Field

In real situations, the magnetic field lines of an active region have the shape of loops whose footpoints are fixed in the photosphere. With an eye to obtain analytic solutions, let us discuss a model in which the magnetic field is horizontal, $\mathbf{B}_0 = B_0\mathbf{e}_x$, and the ends of the field lines are rigidly fixed on the vertical $x = 0$ and $x = L$ planes. This geometry is used, for example, in analyzing the oscillations or stability of a single coronal loop. In contrast, we are interested in analyzing the oscillations of not a single loop but the entire ensemble of magnetic loops that constitute the magnetosphere of an active region. Therefore, in the homogeneous model discussed below, the magnetic loops, as such, are not yet isolated in any way.

Supplementing Eq. (1) with appropriate boundary and initial conditions, we can solve the problem either on the propagation of the boundary regime or on the decay of the initial disturbance. In the absence of rigid fixing and for $B_0 = \text{const}$, $C_\text{s} = \text{const}$, and $\rho_0 = \text{const}$, $\partial\boldsymbol{\xi}/\partial y = 0$, the elementary solution of Eq. (1) is a plane wave $\boldsymbol{\xi} \propto \exp(i\omega t - ik_z z - ik_x x)$. This wave satisfies the standard dispersion relation for fast (+) and slow (−) magnetoacoustic waves (Kulikovskii and Lyubimov 1962):

$$2\omega_{+,-}^2 = \left\{ \left(C_\text{s}^2 + V_\text{A}^2\right) k^2 \right. \qquad (2)$$
$$\left. \pm k^2 \sqrt{\left(C_\text{s}^2 + V_\text{A}^2\right)^2 - 4C_\text{s}^2 V_\text{A}^2 k_x^2/k^2} \right\},$$
$$k^2 = k_x^2 + k_z^2,$$

where $V_\text{A}^2 = B_0^2/4\pi\rho_0$ is the square of the Alfvén velocity. For plasma displacements across, ξ_z, and along, ξ_x, the equilibrium magnetic field, the following expression is valid:

$$\xi_x/\xi_z = k_x k_z C_\text{s}^2/(\omega^2 - k_x^2 C_\text{s}^2). \qquad (3)$$

The rigid fixing condition $\boldsymbol{\xi}(x = 0, L) = 0$ is satisfied in the standard way. For this purpose, the solution is sought in the form of a superposition of two plane oblique waves:

$$\boldsymbol{\xi} \propto (1/2)\left\{\exp(ik_x x + \phi) + \exp(-ik_x x - \phi)\right\}$$
$$\times \exp(i\omega t - ik_z z).$$

Hence, we obtain

$$\boldsymbol{\xi} \propto \sin(K_n x) \exp(i\omega t - ik_z z), \qquad (4)$$
$$K_n = \pi n/L, \quad n = 1, 2, 3, \ldots.$$

We are concerned with the transient wave process that accompanies the propagation of an arbitrary disturbance along the Z axis. The transient process arises from the group-velocity dispersion of the spectral components in the original signal. From (2) and (4), we obtain for the group-velocity component $V_{\text{g}z}$ across the magnetic field

$$V_{\text{g}z} = \frac{\partial\omega}{\partial k_z} = \frac{\omega k_z}{k^2} + \frac{C_\text{s}^2 V_\text{A}^2 k_x^2 k_z}{\omega\left\{2\omega^2 - k^2(C_\text{s}^2 + V_\text{A}^2)\right\}}; \qquad (5)$$
$$k_x = K_n, \quad \omega = \omega_{+,-}.$$

The value of $V_{\text{g}z}$ becomes zero at $k_z = 0$, which, according to (2), corresponds to the frequencies

$$\Omega_n^2 = K_n^2\left\{C_\text{s}^2 + V_\text{A}^2 \pm \left(C_\text{s}^2 - V_\text{A}^2\right)\right\}/2, \quad C_\text{s} > V_\text{A}, \qquad (6)$$

$$\Omega_n^2 = K_n^2 \left\{ C_\mathrm{s}^2 + V_\mathrm{A}^2 \pm \left(V_\mathrm{A}^2 - C_\mathrm{s}^2 \right) \right\} /2, \quad C_\mathrm{s} < V_\mathrm{A}.$$

The case $C_\mathrm{s} = V_\mathrm{A}$ constitutes an exception. Here, the wave energy is also transferred across the magnetic field at $k_z = 0$ (Sivukhin 1966).

The Approximation of a Strong Magnetic Field

In the approximation of a strong magnetic field, it is convenient to use the shortened dispersion relations that can be derived from (2) by discarding small terms of the order of $C_\mathrm{s}^2/V_\mathrm{A}^2$. The shortened dispersion relation for a fast magnetoacoustic wave is

$$\omega_+^2 \cong \left(C_\mathrm{s}^2 + V_\mathrm{A}^2 \right) k_z^2 + \Omega_n^2, \quad \Omega_n^2 = V_\mathrm{A}^2 K_n^2, \qquad (7)$$
$$K_n = \frac{\pi n}{L}.$$

This dispersion relation corresponds to the wave equation

$$\frac{\partial^2 \xi_z}{\partial t^2} = \left(C_\mathrm{s}^2 + V_\mathrm{A}^2 \right) \frac{\partial^2 \xi_z}{\partial z^2} + V_\mathrm{A}^2 \frac{\partial^2 \xi_z}{\partial x^2} \qquad (8)$$

with the boundary condition $\xi_z(t; x = 0, L; z) = 0$.

According to (3), at $C_\mathrm{s}^2 \ll V_\mathrm{A}^2$, motions across, $\xi_z \gg \xi_x$, and along, $\xi_x \gg \xi_z$, the magnetic field dominate in the fast and slow modes, respectively. Because of the condition $k_x = K_n$, a slow magnetoacoustic wave propagates across a strong magnetic field with a low group velocity $V_{\mathrm{g}z} \ll C_\mathrm{s}$ if $\omega > \Omega_n = K_n C_\mathrm{s}$ (6). As a result, a strong fast magnetoacoustic disturbance will reach a given magnetic flux tube first and a weak slow magnetoacoustic perturbation will reach this tube only after a long time. Below, we only discuss the fast mode.

THE RESONANT EXCITATION OF OSCILLATIONS

The appearance of resonance oscillations is attributable to a term in Eq. (8). The physical meaning of this term is easy to understand if we recall that the relation $\partial^2 \xi_z(t, x, z)/\partial x^2 \cong -1/R(t, x, z)$, where $R(t, x, z)$ is the local radius of curvature of the perturbed field line, is valid for small displacements $\xi_z \ll L/n$. Therefore, $V_\mathrm{A}^2 \partial^2 \xi_z/\partial x^2 = F_R/\rho_0$ is the acceleration due to the force $F_R \cong -B_0^2/4\pi R$, which prevents the bending of the initially straight field line. Equation (8) can be said to describe the behavior of an ensemble of stretched "magnetic strings" placed in an elastic liquid.

The Excitation of the Fundamental Mode. Basic Equations and Green's Function

We will discuss the excitation of resonance oscillations in terms of the boundary-value problem. A flare-induced or other disturbance is modeled by an impenetrable piston with a generally arbitrary shape. The motion of the piston is assumed to be known. Let us assume that its vertical velocity $U(t, x, z) \equiv U_z(t, x, z)$ is given, with $U(t; x = 0, L; z) = 0$. Differentiating Eq. (8) with respect to time and denoting the plasma velocity across the magnetic field by $u \equiv \partial \xi_z(t, x, z)/\partial t$, we have

$$\frac{\partial^2 u}{\partial t^2} = \left(C_\mathrm{s}^2 + V_\mathrm{A}^2 \right) \frac{\partial^2 u}{\partial z^2} + V_\mathrm{A}^2 \frac{\partial^2 u}{\partial x^2}, \qquad (9)$$
$$u(t; x = 0, L; z) = 0.$$

Under the assumption of small displacements, the piston is replaced with a velocity source $U(t, x)$ located at the bottom of the atmosphere $z = 0$:

$$u(t, x; z = 0) = U(t, x) = \sum_{n=1}^{\infty} U_n(t) \sin\left(K_n x\right). \qquad (10)$$

In expression (10), the boundary regime is expanded into a series with the condition $U(t; x = 0, L) = 0$. The expansion coefficients are the functions $U_n(t)$ that describe the time behavior of the fundamental ($n = 1$) and remaining ($n = 2, 3, 4, \ldots$) modes at $z = 0$. Supplementing Eqs. (9) and (10) with zero initial conditions, we can seek a solution of the problem on the propagation of the boundary regime in the form of a series of all modes.

We restrict our analysis to the fundamental mode $n = 1$. The lowest value of the frequency Ω_n, $\Omega_1 = K_1 V_\mathrm{A} = \pi V_\mathrm{A}/L$, and the broadest frequency spectrum of traveling ($\omega > \Omega_1$) waves correspond to this mode. Relations (9) then reduce to one equation,

$$\frac{\partial^2 u}{\partial t^2} = \left(C_\mathrm{s}^2 + V_\mathrm{A}^2 \right) \frac{\partial^2 u}{\partial z^2} - \Omega_1^2 u. \qquad (11)$$

Here, we took into account the fact that $\partial^2 u/\partial x^2 = -k_x^2 u = -K_1^2 u$ for the fundamental mode. The initial and boundary conditions for Eq. (11) are

$$u(t = 0; z) = (\partial u/\partial t)_{t=0} = 0, 0 < z < \infty, \qquad (12)$$

$$u(t; z = 0) = U_1(t), 0 < t < \infty.$$

The solution of problem (11), (12) is known (Budak *et al.* 1972) and can be written as

$$u(t', z) = U_1(t' - \tau') - \tau' \int_0^{t'-\tau'} U_1(\lambda) \frac{J_1(\eta)}{\eta} d\lambda, \qquad (13)$$

where $t' = t\Omega_1$, $\tau' = \tau\Omega_1$, $\tau = z/\sqrt{C_s^2 + V_A^2}$, $\eta = \sqrt{(t'-\lambda)^2 - \tau'^2}$, and J_1 is the Bessel function. Note that Eq. (11) is similar to the equation

$$\frac{\partial^2 \xi_z'}{\partial t^2} = C_s^2 \frac{\partial^2 \xi_z'}{\partial z^2} - \Omega_A^2 \xi_z', \qquad (14)$$

which describes the vertical acoustic motions in an atmosphere in a gravitational field. Here, $\xi_z' = \xi_z \exp(z/2H)$ and Ω_A is the aforementioned acoustic cutoff frequency. Despite the outward similarity, Eqs. (11) and (14) are different in origin. Equation (14) corresponds to the situation when (i) the gravity plays a fundamental role; and (ii) the plasma motions are longitudinal and exactly along the strong vertical magnetic field. Equation (11) was obtained under completely different conditions, when (i) the gravity plays no fundamental role and (ii) plasma motions across the strong magnetic field dominate.

In a stratified atmosphere, solution (13) describes the resonant excitation of oscillations whose frequency is close to the acoustic cutoff frequency. As a result, a wave wake appears behind the moving disturbance (Lamb 1932). This property of the solutions of Eq. (14) was used in solar physics in attempts to explain the 5-min oscillations (Schmidt and Zirker 1963; Stein and Schwartz 1972; Kneer and Nakagawa 1976) and longitudinal oscillations in thin magnetic-flux tubes (Rae and Roberts 1982). Zandanov and Uralov (1983a, 1983b, 1984) explained the origin of the 3-min oscillation trains observed in the microwave emission from sunspots by this effect. The 3-min oscillations were analyzed by Fleck and Schmitz (1991), Kalkofen *et al.* (1994), Schmitz and Fleck (1995), and Sutmann *et al.* (1998). The results of these authors left no shadow of doubt that the 3-min oscillations in the actual solar atmosphere owe their origin to the fundamental effect of the resonant excitation of oscillations with a frequency close to the acoustic-cutoff frequency.

The main feature of solution (13)—the appearance of a wave wake when an arbitrary velocity source switches on or off—clearly shows up in the simplest case of a pulse in the shape of the δ function:

$$U_1(t') = U_0 \delta(t'), \qquad (15)$$

where U_0 has the dimensions of velocity. Solution (13) is now Green's function of problem (11), (12). In ordinary variables, it is

$$u(t,z) = U_0 \delta(t-\tau) - (\tau U_0) \frac{J_1\left(\Omega_1 \sqrt{t^2-\tau^2}\right)}{\sqrt{t^2-\tau^2}}. \qquad (16)$$

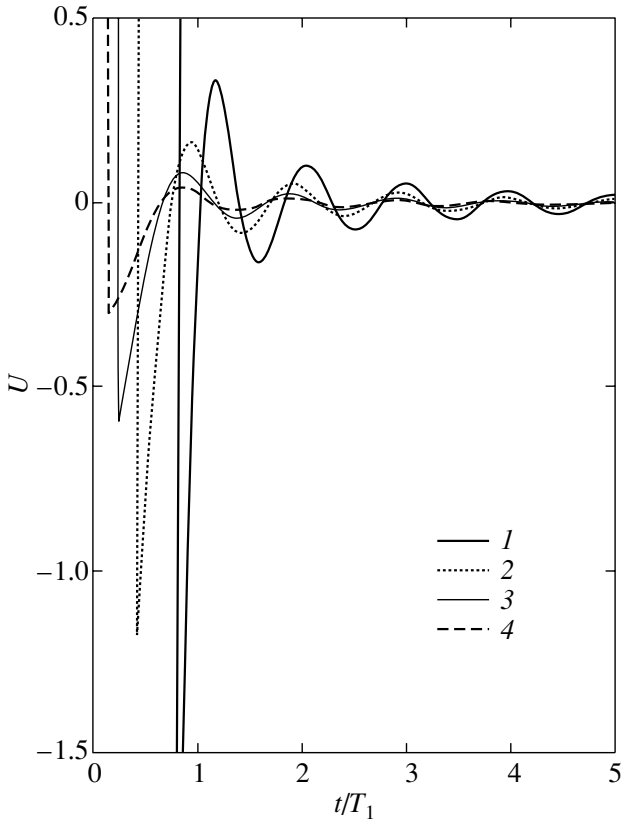

The form of solution (16) at various distances $z = \tau\sqrt{C_s^2 + V_A^2}$ from the piston, $U_0 = 1$. The plasma velocity is along the vertical axis. The dimensionless time t/T_1, where $T_1 = 2\pi/\Omega_1$, is along the horizontal axis. Each curve shows the behavior in time of the velocity of the plasma at a fixed point in space $z(\tau)$ after the δ-function pulse arrived at this point: $\tau =$ (1) $0.1T_1$, (2) $0.2T_1$, (3) $0.4T_1$, and (4) $0.8T_1$. After one or two rapidly damped oscillations, the periodicity of wave motions at a fixed point of space is virtually equal to T_1. The oscillation amplitude increases with distance from the piston.

Using the representation of the Bessel function for large arguments yields the behavior of solution (16) at $t^2 \gg \tau^2 + \Omega_1^{-2}$:

$$u(t,z) \cong -U_0 \frac{z}{\sqrt{C_s^2 + V_A^2}} \sqrt{\frac{2}{\pi\Omega_1}} \frac{1}{t^{3/2}} \times \cos\left(\Omega_1 t - \frac{3\pi}{4}\right). \qquad (17)$$

The curves in the figure show the time behavior of solution (16) at various distances from the piston (the place of impulsive energy release). As one recedes from the piston, the amplitude of the wave wake in solution (16) indefinitely increases proportionally to z. This circumstance is attributable to two factors. First, the wave energy contained in the δ-function pulse is

infinitely large. Second, there is persistent dispersion-induced outflow of this energy into the growing wave tail.

The Model of a Piston with a Finite Time of Action

Since in practice there are no phenomena described by the δ function, we replace it with a short, $\Delta t' = \Omega_1 \Delta t \ll 1$, rectangular velocity pulse:

$$U_1(t') = U_0 \psi(t'), \psi(t') \equiv H(t') - H(t' - \Delta t'), \quad (18)$$

where $H(t')$ is the Heaviside function. In contrast to the previous case where $\int U_0 \delta(t') dt' = U_0$, now $\int U_0 \psi(t') dt' = U_0 \Delta t'$. Therefore, for a very short pulse, $\Delta t' \ll 1$, the following analogue of expression (16) is an approximation to the exact solution:

$$u(t,z) \cong U_0 \psi(t-\tau) - \frac{z\Omega_1}{\sqrt{C_s^2 + V_A^2}}(U_0 \Delta t) \quad (19)$$
$$\times \frac{J_1\left(\Omega_1 \sqrt{t^2 - \tau^2}\right)}{\sqrt{t^2 - \tau^2}}.$$

Expression (19) describes the amplitude and shape of the entire wake behind the short pulse. Comparison of the exact (13) and approximate solutions for $t \to \tau$ gives a constraint on the validity of expression (19): $\tau = z/\sqrt{C_s^2 + V_A^2} \ll 2/\left(\Omega_1^2 \Delta t\right)$. The small decrease in the amplitude of the leading edge (discontinuity) of the pulse may be ignored within this distance range. In the exact solution, the amplitude of the leading discontinuity remains constant. Note that, for a smoothly inhomogeneous medium, the discontinuity amplitude varies according to the laws of linear acoustics as long as the nonlinearity may be disregarded. In an asymptotic representation, $t^2 \gg \tau^2 + \Omega_1^{-2}$, the inaccuracy of expression (19) lies in the absence of an additional phase shift of the order of $\Omega_1 \Delta t \ll 1$, which is unimportant.

The first term on the right-hand side of (19) describes the propagation of the pulse at velocity $\sqrt{C_s^2 + V_A^2}$ without any distortion of its shape. The second term describes the excitation of oscillations at an arbitrary point z after the passage of the leading edge of the initial disturbance through this point. If the velocity pulse is positive, $U_0 > 0$, then the strongest first oscillation that follows it corresponds to the rarefaction phase. For the amplitude u_{max} of this oscillation, we can easily find from (19) for $t \to \tau$ that $u_{max} \approx U_0 \tau \left(\Omega_1^2 \Delta t\right)/2$. The asymptotic solution is reached quickly, after two or three oscillations. The characteristic oscillation frequency approaches the resonance frequency Ω_1 and the oscillation amplitude begins to smoothly decrease as $1/t^{3/2}$. An important circumstance follows from (19): in the case of an impulsive disturbance, the intensity of the wave wake is determined by the parameter $U_0 \Delta t$. This parameter is equal to the area of the initial velocity pulse in variables (u, t) and is nothing but the maximum displacement of the piston located at the bottom of the atmosphere.

Let us estimate the ratio of the energy E of the wave wake to the (kinetic plus magnetic) energy, $E_0 \approx \rho U_0^2 \Delta t \sqrt{C_s^2 + V_A^2}$, of the initial wave disturbance generated by the piston. Taking $T_1 \sqrt{C_s^2 + V_A^2} \approx 2L$, where $T_1 = 2\pi/\Omega_1$, as the characteristic scale length, we have $E \approx 2L\left(\overline{\rho u^2}\right) \approx L\rho u_{max}^2$. Therefore, $E/E_0 \approx \pi^4 z^2 (V_A \Delta t)/(4L^3)$. The energy of the wave wake rapidly increases with distance. This is true as long as $E < E_0$ (and $u < u_{max}$), which is equivalent to the validity condition for solution (19). Formally, assuming that $z = L/\pi$, which is equal to the radius of a semicircular loop, we derive the order-of-magnitude relation

$$(E/E_0)_{z=L/\pi} \sim \pi^2 (V_A \Delta t)/(4L) = \pi^2 \Delta t/(2T_1),$$
$$\Delta t/T_1 \ll 1.$$

For a pulse duration $\Delta t \approx 0.2 T_1$, the energy of the wave wake is of the order of the energy of the flare-induced disturbance.

The switching of a periodic velocity source, $U_1(t) = U_0 H(t) \cos \omega t$, is also accompanied by a transient process whose characteristic period corresponds to the frequency Ω_1. The transient process is indistinct at $\omega \gg \Omega_1$ and clearly shows up at $\omega \ll \Omega_1$. The transition of the entire atmosphere from rest to motion with a piston velocity U_0 corresponds to the case $\omega = 0$. This transition is also accompanied by the excitation of oscillations with a period $\cong T_1 = 2L/V_A$, which are damped roughly as $1/t^{3/2}$.

The Effect of a "Heavy" Layer on the Transient Process

The plasma of coronal loops seen in ultraviolet iron lines is cooler and, apparently, denser than the ambient plasma (Aschwanden *et al.* 2002). These conditions are likely to be satisfied only for loops adjacent to the separatrix surfaces of the coronal magnetic field. Therefore, the bulk of the magnetic flux involved in the oscillatory motion of all or part of the magnetosphere of an active region described above is simply unseen. The energy of this motion can be high, because, as we

saw above, the energy of the wave wake sufficiently far from the flare location is comparable to the energy of the initial disturbance. At the same time, it seems clear that, if the gas mass in a coronal loop is too large, then, because of the large inertia, this loop will inhibit general oscillatory motion. The inverse effect of a group of such loops located, for example, along a separatrix surface on the transient process described above can be stronger. Let us attempt to establish a criterion whose satisfaction will allow the effect of "heavy" coronal loops on the parameters of the transient process to be disregarded. For this purpose, we postulate the presence of a homogeneous plasma layer inside of which the coefficients of Eq. (11) differ from those outside. An exact solution of the boundary-value problem described in the preceding section similar to expression (13) is now difficult to obtain. Therefore, we restrict our analysis to estimating the effect of such a layer on the spectral composition of the transient process.

We use the results of the solution of the standard problem on the transmission of a monochromatic wave, $\xi \propto \exp(-i\omega t)$, through a layer $0 \le z \le d$. Inside of the layer, the speed of sound and the Alfvén velocity are C_2 and V_2, respectively. Outside of the layer, in the half-spaces $z < 0$ and $z > d$ (media 1 and 3), the plasma parameters are identical and the speed of sound and the Alfvén velocity are denoted by C_s and V_A, respectively, as previously. There are incident and reflected waves in the half-space $z < 0$, $\xi_1 \propto A_1 \exp(ikz) + B_1 \exp(-ikz)$, and only a transmitted wave in the half-space $z > d$, $\xi_3 \propto A_3 \exp(ik(z-d))$.

The continuity of ξ and $d\xi/dz$ at $z = 0$ and $z = d$ gives a familiar (see, e.g., Grechko *et al.* 1972) expression for the transmission coefficient, $W = |A_3/A_1|^2$, of a particle through a potential barrier or above a potential well. At $\omega \ge \Omega_1$, when $k = \sqrt{(\omega^2 - \Omega_1^2)/(C_s^2 + V_A^2)}$ and $k_2 = \sqrt{(\omega^2 - (\Omega_1^*)^2)/(C_2^2 + V_2^2)}$ are valid, the following expression holds:

$$W = \left[1 + \frac{(k^2 - k_2^2)^2}{4k^2k_2^2}\sin^2 k_2 d\right]^{-1} = (1+\alpha)^{-1}. \quad (20)$$

The potential well corresponds to the"heavy" layer: $\Omega_1^* < \Omega_1$, where $\Omega_1^* = V_2K_1 = \pi V_2/L$. The dispersion of traveling waves $\omega \ge \Omega_1$ at low frequencies is responsible for the appearance of the wave wake described in the preceding section. The distortion of the wake is attributable to the reflection of the spectral components $\omega \to \Omega_1$, when $k \to 0$, from the layer. At $k = 0$, the reflection is total, $W = 0$. The reflection is significant, $W(\omega) > 0.5$, at frequencies in the range from Ω_1 to some frequency determined from the condition $\alpha(\omega) \approx 1$. Let us estimate the relative width, of this range, $\Delta\omega/\Omega_1 = (\omega - \Omega_1)/\Omega_1$. We use the fact that the observed oscillation periods and the corresponding wavelengths are so large and the loop diameters so small that $k_2 d \ll 1$. To estimate k_2, it will suffice to use the condition $k = 0$. Disregarding the speed of sound, we then derive an equality equivalent to the condition $\alpha \approx 1$:

$$\left(\frac{\omega^2}{\Omega_1^2} - 1\right) \approx \frac{1}{4}\left(\frac{\pi d}{L}\right)^2\left(\frac{\rho_2}{\rho} - 1\right)^2,$$

where ρ_2 and ρ are the plasma densities inside and outside of the layer, respectively. The following inequality corresponds to the smallness condition $\Delta\omega/\Omega_1 \ll 1$ for the spectral range of the waves reflected from the layer:

$$\frac{\Delta\omega}{\Omega_1} \approx \frac{1}{8}\left(\frac{\pi d}{L}\right)^2\left(\frac{\rho_2}{\rho} - 1\right)^2 \ll 1. \quad (21)$$

If inequality (21) is satisfied with a margin, then the presence of a "heavy" layer will scarcely affect the parameters of the transient process. Let us estimate $\Delta\omega/\Omega_1$ in order of magnitude. According to the measurements presented in Aschwanden *et al.* (2002), the lengths of oscillating loops lie within the range 74 000–582 000 km, with a mean value being $L \approx 220\,000$ km. The loop diameters lie within the range 5500–16 800 km, with a mean value of $d \approx 8700$ km. The plasma density inside and outside of the loops is highly uncertain. Its mean value inside of the loops was estimated by the above authors to be 6×10^8 cm^{-3}. If we take a typical value of 10^8 cm^{-3} for the ambient plasma density, then $\rho_2/\rho \approx 6$. We then obtain from (21): $\Delta\omega/\Omega_1 \approx 0.037$. It should be noted that the actual value of d in expression (21) can be even smaller than 8700 km if the observed loops are assumed to consist of a web of thinner structures. Their presence is clearly felt when examining the images. At the same time, we cannot rule out the possibility that, actually, $\rho_2/\rho < 6$.

CONCLUSIONS

The homogeneous model magnetosphere of an active region only shows the main physical effect—the resonant excitation of a rapidly damped wake behind the MHD disturbance that propagates across the magnetic field. Oscillations are excited on the dispersion branch of fast magnetoacoustic waves. The rapid damping of the observed oscillations is governed by the dispersion spreading of the pulse of these waves produced by a solar flare or a filament eruption. The oscillations of the magnetic field lines are also transverse and their fundamental period is

close to the period of the fundamental mode. The phenomenon is completely described in terms of ideal magnetohydrodynamics. It is important to note that we discussed the transient wave process for the plane case and only for the fundamental mode, $n = 1$, of the expansion of the boundary regime (10). Thus, the size (along the X axis) of the piston that models the impulsive disturbance is equal to the length of the oscillating field lines. If the piston size is small, then the subsequent modes, $n > 1$, should be taken into account. The latter will lead to a more complex structure of the "transient" solution.

The approximation of a strong magnetic field implies a negligible role of the gas pressure and, accordingly, the dissipative factors that change its value. Such insignificant factors include heat conduction and coronal-plasma losses through intrinsic radiation, however large they are. There is also no need to invoke any reasoning about the waveguide properties of isolated, denser magnetic loops and the resonant absorption (viscosity and electrical conductivity) of the natural oscillations excited in them. The presence of such loops undoubtedly modifies the solution but does not change its global character. The small width (21) of the spectral range of the waves reflected from a "heavy" layer provides evidence for the following conclusion. "Heavy" coronal loops must be forcedly displaced in time by the motions described by expression (13). Thus, the oscillations observed from *TRACE* are, to a greater extent, determined not by the intrinsic parameters (magnetic field, enhanced density, length) of the oscillating loop itself but by the parameters of the transient wave process in the surrounding magnetospheric area of an active region. We cannot but take into account this circumstance when developing the technique for determining the coronal magnetic field strengths from the parameters of the coronal loop oscillations observed from *TRACE*.

The occasionally observed puzzling antiphase behavior (Schrijver *et al.* 2002) of the oscillations of two closely spaced loops can also be naturally explained in terms of our model. In particular, if the two loops are the structural elements of a bipolar magnetic field, then the in-phase behavior of their oscillations in the radial (relative to the bipolar field center) direction automatically implies a periodic convergence and divergence of the oscillating loops. If the line of sight lies in the middle plane that spatially separates the two loops, then the loop displacements transverse to the line of sight will be perceived as occurring in antiphase.

The characteristics of the transient process described above are the result of the solution of the plane problem. In particular, this implies that the source of the impulsive disturbance (piston) must be extended enough in all directions for the use of the one-dimensional Green's function (16) to be justified. In real situations, the piston may prove to be compact. The curvature of the equilibrium magnetic field and, possibly, the regular inhomogeneity of the coronal plasma itself should also be taken into account. These factors can modify the amplitude and shape of the response of the magnetosphere of an active region to the impulsive disturbance generated, for example, at its bottom. The same factors imply the necessity of an allowance for the linear interaction between various types of MHD waves in the wavelength range concerned and, in particular, the possible resonant transformation of a fraction of the energy of a fast magnetoacoustic wave into Alfvén energy (like the field-line resonance in the Earth's magnetosphere). At the same time, it is not quite clear what distribution of the magnetic field and the coronal-plasma parameters should be used in this case. The set of oscillating magnetic domains that constitute the magnetosphere of an actual active region is also a complex resonant system. Another crucially important fact is also the tangible anisotropy in the propagation of almost any impulsive disturbance generated inside or outside an active region.

ACKNOWLEDGMENTS

I am grateful to the referees for the remarks. This study was supported by the Federal Program "Astronomy," The Ministry of Science and Technology (no. 0-27), and the Russian Foundation for Basic Research (project nos. 01-02-16290, and 00-02-16456, 00-15-96710).

REFERENCES

1. M. J. Aschwanden, B. De Pontieu, C. J. Schrijver, and A. M. Title, Solar Phys. **206**, 99 (2002).
2. B. M. Budak, A. A. Samarskii, and A. N. Tikhonov, *Collected Problems on Mathematical Physics* (Nauka, Moscow, 1972).
3. B. Fleck and F. Schmitz, Astron. Astrophys. **250**, 235 (1991).
4. L. G. Grechko, V. I. Sugakov, O. F. Tomasevich, and A. M. Fedorchenko, *Collected Problems on Theoretical Physics* (Vysshaya Shkola, Moscow, 1972).
5. W. Kalkofen, P. Rossi, G. Bodo, and S. Massaglia, Astron. Astrophys. **284**, 976 (1994).
6. F. Kneer and Y. Nakagawa, Astron. Astrophys. **47**, 65 (1976).
7. A. G. Kulikovskii and G. A. Lyubimov, *Magnetohydrodynamics* (Fizmatgiz, Moscow, 1962).
8. H. Lamb, *Hydrodynamics* (Cambridge University Press, Cambridge, 1932).
9. V. M. Nakariakov, L. Ofman, E. DeLuca, B. Roberts, and J. M. Davila, Science **285**, 862 (1999).

10. I. C. Rae and B. Roberts, Astrophys. J. **256**, 761 (1982).
11. H. Schmidt and J. B. Zirker, Astrophys. J. **138**, 1310 (1963).
12. F. Schmitz and B. Fleck, Astron. Astrophys. **301**, 483 (1995).
13. C. J. Schrijver, M. J. Aschwanden, and A. M. Title, Solar Phys. **206**, 69 (2002).
14. C. J. Schrijver and D. S. Brown, Astrophys. J. **537**, L69 (2000).
15. D. V. Sivukhin, Magn. Gidrodin. **1**, 35 (1966).
16. A. A. Solov'ev, B. B. Mikhalyaev, and E. A. Kirichek, Fiz. Plazmy **28**, 758 (2002).
17. R. E. Stein and R. A. Schwartz, Astrophys. J. **177**, 807 (1972).
18. G. Sutmann, Z. E. Musielak, and P. Ulmschneider, Astron. Astrophys. **340**, 556 (1998).
19. V. G. Zandanov and A. M. Uralov, Issled. Geomagn. Aeronom. Fiz. Solntsa **65**, 97 (1983a).
20. V. G. Zandanov and A. M. Uralov, Issled. Geomagn. Aeronom. Fiz. Solntsa **65**, 107 (1983b).
21. V. G. Zandanov and A. M. Uralov, Solar Phys. **93**, 301 (1984).

Translated by V. Astakhov

Astronomy Letters, Vol. 29, No. 7, 2003, p. 494. Translated from Pis'ma v Astronomicheskiĭ Zhurnal, Vol. 29, No. 7, 2003, p. 560.

The Contour of an Orbit and a Stable Periodic Orbit

N. Yu. Kretser* **and T. A. Agekyan**

Astronomical Institute, St. Petersburg State University, Universitetskii pr. 28, Petrodvorets, 198504 Russia

Received September 23, 2002

Abstract—We derive an equation that relates the contour of an orbit and a stable periodic orbit.

Key words: *periodic orbits, stability.*

A periodic orbit can result either from the merging of two sides of a box-shaped orbit or from the merging of two shells of a shell-like orbit. The result depends on the form of the potential $U(r,z)$ and on the specified energy integral I.

Let the contour of an orbit in the meridional plane of a rotationally symmetric potential $U(r,z)$ be given by the equality

$$F(r,z)=0. \tag{1}$$

The curvature of this contour is defined by the expression

$$k=\begin{vmatrix} F''_{rr} & F''_{rz} & F'_r \\ F''_{zr} & F''_{zz} & F'_z \\ F'_r & F'_z & 0 \end{vmatrix} : (F'^2_r+F'^2_z)^{\frac{3}{2}}. \tag{2}$$

For the contour of the orbit to coincide with a stable periodic orbit, it is necessary and sufficient that the curvature of the contour of the orbit be equal to the curvature of a trajectory in the field of the potential $U(r,z)$.

The equation of a trajectory was derived by Agekyan (1972):

$$\frac{\partial f}{\partial l}=\frac{\partial f}{\partial r}\cos f+\frac{\partial f}{\partial z}\sin f \tag{3}$$

$$=\frac{1}{2(U(r,z)+I)}\left(-\frac{\partial U}{\partial r}\sin f+\frac{\partial U}{\partial z}\cos f\right),$$

where $\dfrac{\partial f}{\partial l}$ is the curvature of the trajectory, f is the angle between the tangent to the trajectory in the meridional plane and the abscissa R, l is the direction along the tangent to the trajectory, and I is the energy integral.

Consequently, the equation

$$\begin{vmatrix} F''_{rr} & F''_{rz} & F'_r \\ F''_{zr} & F''_{zz} & F'_z \\ F'_r & F'_z & 0 \end{vmatrix} - (F'^2_r+F'^2_z)^{\frac{3}{2}}\frac{1}{2(U+I)} \tag{4}$$
$$\times\left(-\frac{\partial U}{\partial r}\sin f+\frac{\partial U}{\partial z}\cos f\right)=0$$

determines the position of a stable periodic orbit.

REFERENCES

1. T. A. Agekyan, Astron. Zh. **49**, 371 (1972) [Sov. Astron. **16**, 303 (1972)].

Translated by A. Dambis

*E-mail: nata@NK1327.spb.edu

1063-7737/03/2907-0494$24.00